

Fig. 6 Uniform and adaptive meshes with their temperature solution contours for a plate subjected to a highly localized surface heating

$$+ \sum_{n=1,3}^{\infty} \frac{1}{\lambda_n \left(H^2 + \frac{n^2 \pi^2}{4L^2}\right)} \times \left[H(2\cos(\alpha)\sinh(HW)) + \frac{n\pi}{2L}(2\sin(\alpha)\cosh(HW))\right] \times \left[\cos\left(\frac{n\pi\xi}{2L}\right)\frac{\sinh(\lambda_n y)}{\cosh(\lambda_n h)}\right]. \tag{27}$$

where the origin and the directions of the ξ -y coordinate system are shown in Fig. 8, q is the moving heat source, h is the plate width, $H = \rho cv/2k$, ρ is the plate density, c is the

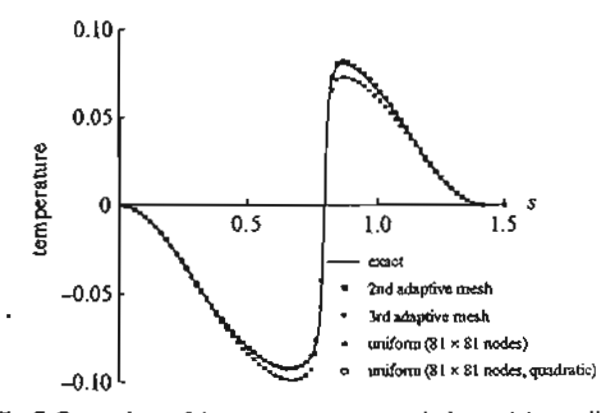


Fig. 7 Comparison of the exact temperature solution and the predicted temperatures from the uniform and adaptive meshes

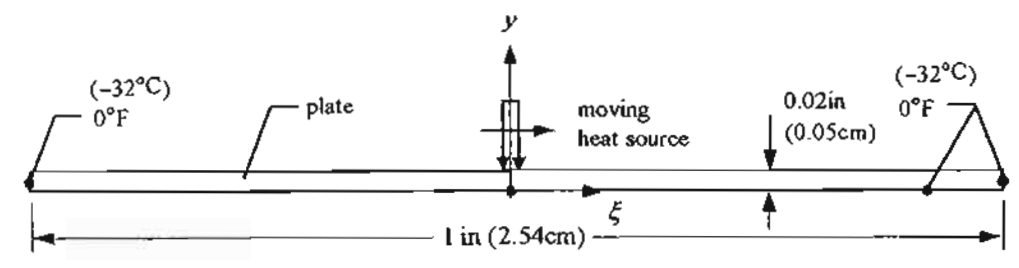


Fig. 8 Problem statement for transient thermal analysis of a plate subjected to a moving heat source

specific heat, v is the velocity of the moving heat source, and k is the plate thermal conductivity. The parameter α and λ_n in Eq. (27) are defined by

$$\alpha = \frac{n\pi w}{2L},$$

$$\lambda_n = \sqrt{\frac{n^2 \pi^2}{4L^2} + H^2},$$
(28)

where L is the plate length, and w is the width of the moving heat source simulated by a square pulse.

To clearly evaluate the performance and compare the solution accuracy obtained from the conventional and the nodeless variable flux-based finite element methods, the steady-state heat transfer case of the problem is first used. For the steady-state condition when the heat pulse is at the center of the plate, the transient temperature solution as shown in Eq. (27) is reduced to,

$$T_{\text{steady}} = \frac{8Lq}{\pi^2 k} \sum_{n=1,3}^{\infty} \frac{\sin(\alpha) \tanh\left(\frac{n\pi h}{2L}\right)}{n^2}.$$
 (29)

Such steady-state solution behavior represents a very high temperature with the magnitude of 581.82°F (291.23°C) on the edge at the heat pulse impingement location. The high temperature is localized with very steep distribution in an approximate narrow band of 0.01 in (0.025 cm).

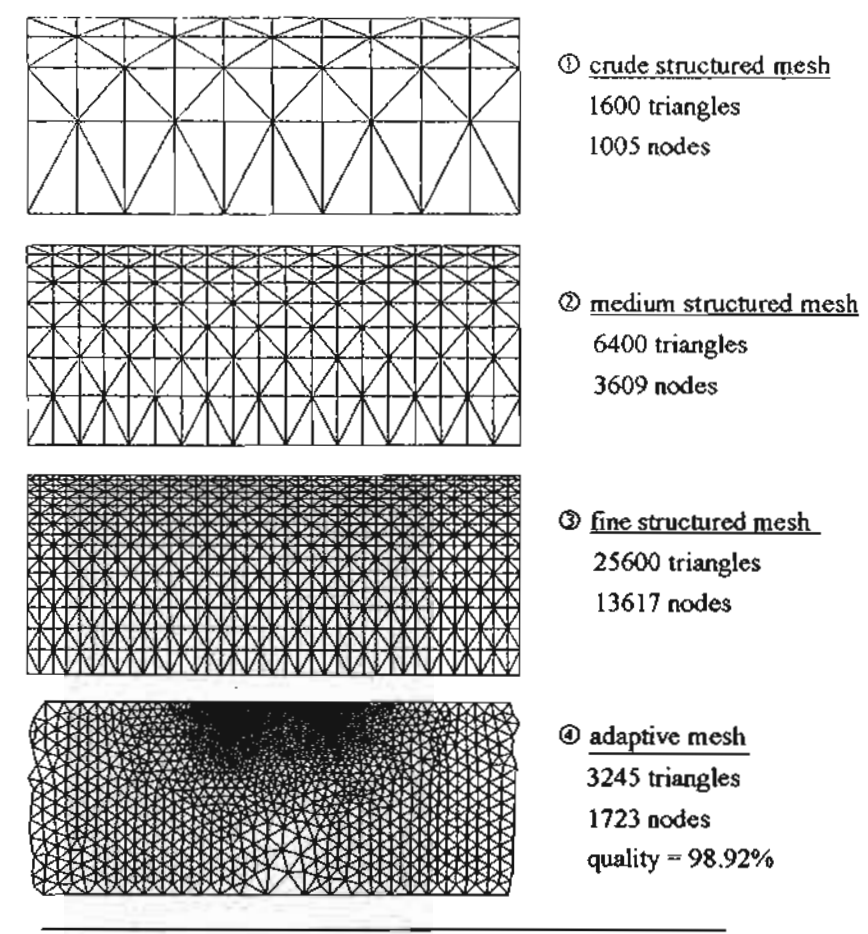
Figure 9 shows sections of the four finite element models used for predicting the plate temperature response. The first three models are the structured mesh models with graded elements near the top edge. These three models are crude, medium, and fine finite element models with 1600, 6400, and 25600 standard triangular elements, respectively. The fourth model is an adaptive mesh model with 3245 nodeless variable finite elements. The table in Fig. 9 compares the predicted peak temperature response at the heat pulse impingement location obtained from the different finite element mesh models using the conventional and the flux-based finite element methods. The values in the brackets denote the percentage error of the predicted peak temperature as compared to the exact solution. The table shows that the adaptive mesh uses fewer elements than the fine structured mesh but can achieve higher solution accuracy. The table also indicates that the nodeless variable flux-based finite element method attains higher solution accuracy than all the three

conventional finite element mesh models. Figure 10 shows the convergence rates obtained from the conventional and the nodeless variable finite element methods on both the graded and regular uniform structured meshes. In this figure, NE denotes the number of elements. Figure 11 shows the predicted temperature contours on the entire plate obtained from the nodeless variable finite element method.

For the case of transient heat transfer analysis, the adaptive meshing technique combined with the nodeless variable flux-based finite element method is used to predict the temperature response. The adaptive meshing technique is incorporated into the finite element method to adapt the mesh to the transient solution behavior. Figure 12 shows the adaptive meshes and their temperature solution contours at three typical times. Detail of the adaptive mesh near the heat pulse impingement location and the temperature contours are shown in the lower figures. These figures show that small clustered elements are generated in the region of steep temperature gradients to capture the predicted peak temperature and the localized temperature distribution. At the same time, larger elements are generated in the other regions to reduce the computational time and the computer memory. Such a typical transient adaptive mesh consists of approximately 2000 triangles. At the heat pulse impingement location, the predicted peak temperature is 572.62°F (286.12°C) as compared to 573.07°F (286.37°C) of the exact solution given by Eq. (27) with a relative difference less than 0.1%. The comparison of the exact and the predicted temperature distributions along the top edge is shown in Fig. 13. The figure shows that the temperature distribution obtained from the adaptive meshing technique combined with the nodeless variable flux-based finite element method is in very good agreement with the exact solution.

5 Conclusions

The nodeless variable flux-based finite element method was developed to analyze two-dimensional steady-state and transient heat transfer problems. The nodeless variable finite element was described and their finite element equations were derived. The flux-based formulation was applied to reduce the computational complexity as compared to the conventional finite element method. The solution accuracy was further improved by implementing an adaptive meshing



Mesh	Temperature (%Error)	
	Conventional FE	Nodeless FE
0	558.40 (4.26)	583.23 (0.26)
②	575.83 (1.09)	581.86 (0.0073)
3	580.32 (0.27)	581.83 (0.0018)
④	581.36 (0.09)	581.82 (0.0000)

Fig. 9 Comparison of the predicted peak temperatures obtained from the conventional and the nodeless variable finite element methods on both the graded structured and unstructured meshes

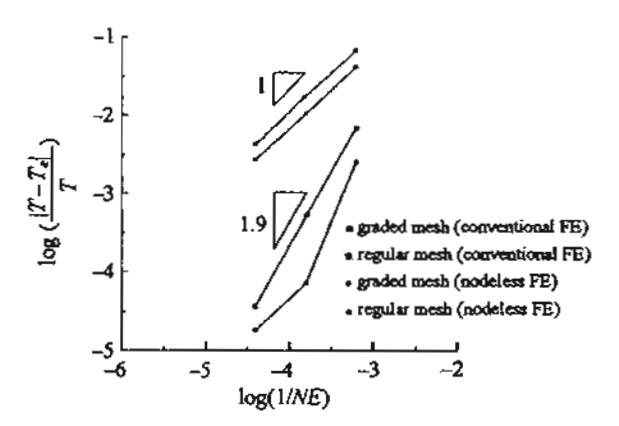


Fig. 10 Comparison of the orders for convergence rates at x = 0.0 and y = 0.02 on the structured meshes

technique. The technique places small elements in the regions with drastic changes of temperature gradients. At the same time, larger elements are generated in other regions to reduce the total number of unknowns and the computational time. The combined procedure was evaluated by two heat transfer problems that have exact solutions. The problems are the steady-state heat conduction analysis of a plate subjected to a highly localized surface heating, and the transient thermal analysis of a plate subjected to a moving heat source. These problems show that the nodeless variable flux-based finite element method incorporated with the adaptive meshing technique can increase the analysis solution accuracy, and meanwhile it significantly reduce the total number of unknowns as compared to the standard nonadaptive mesh.



Fig. 11 Adaptive mesh and temperature distribution contours

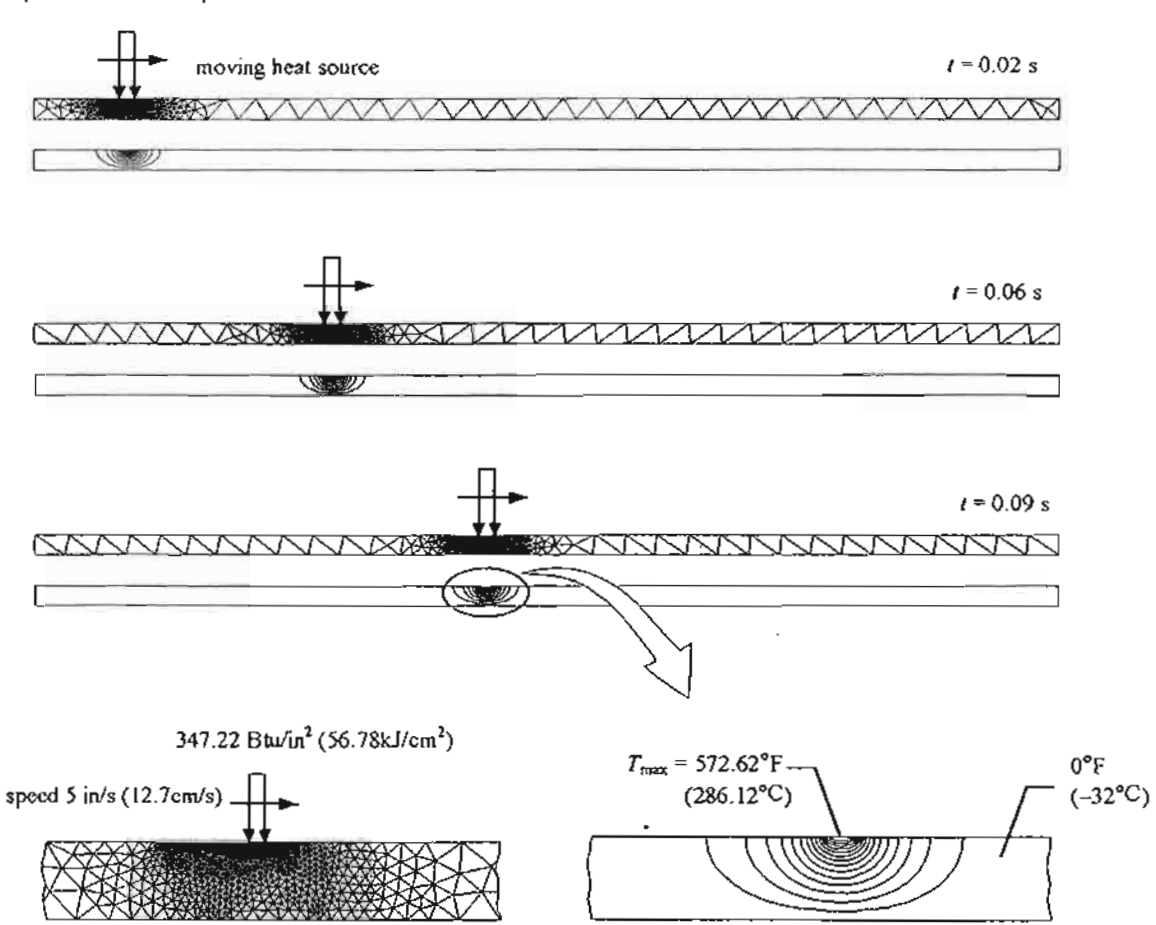


Fig. 12 Adaptive mesh movement and the transient temperature response as the heat source moves across the plate

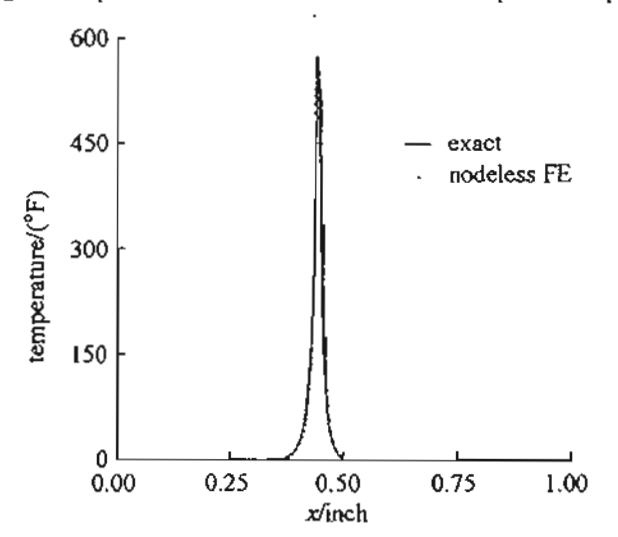


Fig. 13 Comparison of the exact temperature solution and the predicted temperature distribution obtained from the combined adaptive meshing technique and the nodeless finite element method

Acknowledgements The authors are pleased to acknowledge the Thailand Research Fund (TRF) for supporting this research work.

References

- Eckert, E.R.C., Goldstein, R.J., Ibele, W.E., Patankar, S.V.: Heat transfer—a review of 1989 literature. Int J Heat Mass Transfer 33(11), 2349-2437 (1990)
- Noor, A.K.: Computational structures technology: leap frogging into the twenty-first century. Computers & Structures 73(1-5), 1-31 (1999)
- Dechaumphai, P., Morgan, K.: Transient thermal-structural analysis using adaptive unstructured remeshing and mesh movement. Thermal Structures and Materials for High-Speed Flight, AIAA, Washington, D. C., 205-228, 1992
- Polesky, S.P., Dechaumphai, P., Glass, C.E., Pandey, A.K.: Threedimensional thermal-structural analysis of a swept cowl leading edge subjected to skewed shock-shock interference heating. J Thermophysics 6(1), 48-54 (1992)

- Limtrakarn, W., Dechaumphai, P.: Adaptive finite element method for high-speed fluid-structure interaction. Acta Mechanica Sinica 20(6), 597-606 (2004)
- Dechaumphai, P., Phongthanapanich, S., Sricharoenchai, T.: Combined Delaunay triangulation and adaptive finite element method for crack growth analysis. Acta Mechanica Sinica 19(2), 162–171 (2003)
- Phongthanapanich, S., Dechaumphai, P.: Mixed entropy fix method for Roe's flux-difference splitting scheme with automatic mesh generation. Trans of CSME 28(3-4), 531-550 (2004)
- Žienkiewicz, O.C., Taylor, R.L.: Finite element method, volume 1: The basis, Fifth Edition. Woburn, Butterworth-Heinemann, 2000
- Beckett, G., Mackenzie, J.A., Robertson, M.L.: A moving mesh finite element method for the solution of two-dimensional Stefan problems. J Comput Phys 168(2), 500-518 (2001)
- Huang, W.: Practical aspects of formulation and solution of moving mesh partial differential equations. J Comput Phys 171(2), 753– 775 (2001)

- Tang, H.Z., Tang, T.: Adaptive mesh methods for one- and twodimensional hyperbolic conservation laws. SIAM J Numer Anal 41(2), 487-515 (2003)
- Shewchuck, J.R.: An introduction to the conjugate gradient method without the agonizing pain. Pittsburgh, PA 15213, Carnegic Mellon University, 1994
- Hughes, T.J.R., Levit, I., Winget, J.: An element-by-element solution algorithm for problems of structural and solid mechanics. Comput Methods Appl Mech Engrg 36(2), 241-254 (1983)
- Babuska, I., Aziz, A.K.: On the angle condition in the finite element method. SIAM J Numer Anal 13(2), 214–226 (1976)
- Ruppert, J.: A delaunay refinement algorithm for quality 2-dimensional mesh generation. J Algorithm 18(3), 548-585 (1995)
- McGowan, D.M., Camarda, C.J., Scotti, S.J.: A simplified method of thermal analysis of a cowl leading edge subjected to intense localized heating. NASA TP-16505, 1990

บทความทางวิชาการ เรื่อง

Combined Characteristic-Based Split

Algorithm and Mesh Adaptation Technique
for High-Speed Compressible Flow Analysis

Published in the

Key Engineering Materials

Vol. 12, pp. 376-388

2005

Combined characteristic-based split algorithm and mesh adaptation technique for high-speed compressible flow analysis

Parinya Boonmarlert, Sutthisak Phongthanapanich & Pramote Dechaumphai* Mechanical Engineering Department, Chulalongkorn University, Bangkok 10330, Thailand

Received 1 November 2004; accepted 26 July 2005

The characteristic-based split algorithm is combined with a mesh adaptation technique to analyze high-speed inviscid compressible flow problems. The solution accuracy is improved by coupling an error estimation procedure to an adaptive remeshing technique that generates small elements in regions with large change in solution gradients, and at the same time, larger elements in the other regions. The efficiency of the combined procedure is evaluated by solving several problems for both transient and steady-state flow behaviours.

IPC Code: F15B

High-speed compressible flows normally include complex flow phenomena, such as shock waves, flow expansions, and shock-shock interactions¹. Effects of these phenomena are critical in the design of high-speed vehicle structures. These flows are characterized by steep gradients that need robust analyses and computational techniques as well as dense meshes to obtain good resolution of flow behaviours. During the past decades, several computational techniques were developed to alleviate the computational effort in order to capture complex flow fileds. These algorithms include the Taylor-Galerkin algorithm², the Petrov-Galerkin algorithm³, the least-squares algorithm⁴, the cell-centered upwinding algorithm⁵, and the characteristic-based split algorithm⁶.

In this paper, the characteristic-based split algorithm is combined with the adaptive Delaunay triangulation algorithm⁷⁻⁹ to improve the accuracy of the predicted flow solutions. The characteristic-based split algorithm is selected for the flow analysis because of its capability to provide solution accuracy for most of the fluid dynamics problems. The Delaunay triangulation is used in the construction of triangular meshes for arbitrary two-dimensional geometry. An adaptive remeshing technique is also included in order to generate small elements in the region of large change in solution gradients to increase solution accuracy. At the same time, larger elements are generated in the other regions to reduce the computational time.

The paper starts by explaining the theoretical formulation for inviscid compressible flow analysis and the characteristic-based split algorithm. The basic concept of Delaunay triangulation and the adaptive remeshing technique are then described. Finally, the efficiency of the combined procedure is evaluated by analyzing four examples of high-speed inviscid compressible flows; a Sod shock tube, an oblique shock reflection at a wall, a Mach 2.0 flow in a channel with compression and expansion ramps, and a shock-shock interaction on a cylinder. The paper concentrates on the demonstration of the solution accuracy improvement and the computational efficiency by using the proposed procedure.

Theoretical Formulation and Solution Procedure

Governing differential equations

The Euler equations for two-dimensional inviscid compressible flow are written in the conservation form as,

$$\frac{\partial}{\partial t} \{U\} + \frac{\partial}{\partial x} \{E\} + \frac{\partial}{\partial y} \{F\} = 0 \qquad \dots (1)$$

The vector $\{U\}$ contains the conservation variables defined by,

$$\{U\} = \begin{bmatrix} \rho & \rho u & \rho v & \rho \varepsilon \end{bmatrix}^T \qquad \dots (2)$$

where ρ is the fluid density, u and v are the velocity components in the x and y directions, respectively, and ε is the total energy of the fluid. The vectors $\{E\}$

^{*}For correspondence (E-mail: fmepdc@eng.chula.ac.th)

and $\{F\}$ consist of inviscid fluxes in the x and y directions, respectively. These inviscid flux vectors are given by,

$$\{E\} = \begin{bmatrix} \rho u & \rho u^2 + p & \rho uv & \rho u\varepsilon + \rho u \end{bmatrix}^T \dots (3)$$

and

$${F}^{r} = \left[\rho v \quad \rho u v \quad \rho v^{2} + p \quad \rho v \varepsilon + p v \right]^{r} \quad \dots \quad (4)$$

where p is the pressure. The total energy consists of the internal energy and the kinetic energy defined by,

$$\varepsilon = e + \frac{1}{2} \left(\mu^2 + \nu^2 \right) \tag{5}$$

The internal energy is assumed to satisfy the equation of state that can be written in the form,

$$e = \frac{p}{\rho(\gamma - 1)} \qquad \dots \tag{6}$$

where γ is a specific heat ratio.

Characteristic-based split algorithm

The characteristic-based split algorithm was first introduced by Zienkiewicz and Codina⁶ to solve different categories of fluid dynamics problems. The basic concept of the characteristic-based split algorithm is to use the characteristic-Galerkin method and the operator-splitting procedure to establish recurrence relations for temporal discretization, while the method of weighted residuals with Galerkin's criteria is used for spatial discretization for deriving the finite element equations.

Temporal discretization

The characteristic-based split algorithm for the high-speed inviscid compressible flow analysis 10 consists of four steps. In the first step, the intermediate values of conservative variables of the momentum equations are calculated by omitting the pressure gradient terms. In the second step, the continuity equation is solved to determine the density changes in the fluid. Then, the conservative variables of the momentum equations are updated in the third step. Finally, the energy equation is solved for the total energy in the last step, and the pressure is calculated using the equation of state. These four steps can be written in the fully explicit form as follows,

Step 1: The intermediate momentum equations,

$$\Delta U_{i}^{*} \simeq \Delta t \left[-\frac{\partial \left(u_{j} U_{i} \right)}{\partial x_{j}} + \frac{\Delta t}{2} u_{k} \left(\frac{\partial^{2} \left(u_{i} U_{j} \right)}{\partial x_{k} \partial x_{j}} + \frac{\partial^{2} p}{\partial x_{k} \partial x_{i}} \right) \right]^{u} \dots (7)$$

where U_i are the mass fluxes and Δt is the time step.

Step 2: The continuity equation,

$$\Delta \rho = \Delta t \left[-\frac{\partial U_i}{\partial x_i} - \frac{1}{2} \frac{\partial \Delta U_i^*}{\partial x_i} + \frac{\Delta t}{2} \frac{\partial^2 p}{\partial x_i \partial x_i} \right]^a \qquad \dots (8)$$

Step 3: The momentum correction equations,

$$\Delta U_i = \Delta U_i^* - \Delta t \left[\frac{\partial p_i}{\partial x_i} \right]^n \qquad \dots (9)$$

Step 4: The energy equation,

$$\Delta \rho \varepsilon = \Delta t \left[-\frac{\partial \left(u_{j} \left(\rho \varepsilon + p \right) \right)}{\partial x_{j}} \right]$$

$$+\frac{\Delta t}{2}u_k\frac{\partial}{\partial x_k}\left[\frac{\partial \left(u_j(\rho\varepsilon+p)\right)}{\partial x_j}\right]^n \qquad \dots (10)$$

Spatial discretization

The triangular element assumes linear interpolation for the variables U, E, F, ρ and p as,

$$U = N_{\alpha}(x, y) U_{\alpha} \qquad \dots (11a)$$

$$E = N_{\alpha}(x, y) E_{\alpha} \qquad \dots (11b)$$

$$F = N_{\alpha}(x, y) F_{\alpha} \qquad \dots (11c)$$

$$\rho = N_{\alpha}(x, y) \rho_{\alpha} \qquad \dots (11d)$$

$$p = N_{\alpha}(x, y) p_{\alpha} \qquad \dots (11e)$$

where $\alpha=1, 2, 3$ and N_{α} are the element interpolation functions.

The method of weighted residuals with Galerkin's criteria is employed to discretize the finite element equations by multiplying Eqs (7)-(10) with the weighting functions, N_{α} , and performing integration by parts using the Gauss theorem¹¹ to yield the element equations shown in the steps below,

Step 1: The intermediate momentum equations,

$$\int_{\Omega} N_{\alpha} \Delta U_{i}^{*} d\Omega =$$

$$\Delta t \left[\int_{\Omega} \frac{\partial N_{\alpha}}{\partial x} \left(u_{j} U_{i} \right) d\Omega - \int_{\Gamma} N_{\alpha} \left(u_{j} U_{i} \right) n_{j} d\Gamma \right]^{n}$$

$$- \frac{\Delta t^{2}}{2} u_{k} \left[\int_{\Omega} \frac{\partial N_{\alpha}}{\partial x_{k}} \left[\frac{\partial \left(u_{j} U_{i} \right)}{\partial x_{j}} + \frac{\partial p}{\partial x_{i}} \right] d\Omega$$

$$+ \int_{\Gamma} N_{\alpha} \left[\frac{\partial \left(u_{j} U_{i} \right)}{\partial x_{j}} + \frac{\partial p}{\partial x_{i}} \right] n_{k} d\Gamma \right]^{n} \qquad \dots (12)$$

Step 2: The continuity equation,

$$\int_{\Omega} N_{\alpha} \Delta \rho \, d\Omega = \Delta I \left[\int_{\Omega} \frac{\partial N_{\alpha}}{\partial x_{i}} \left(U_{i} + \frac{1}{2} \Delta U_{i}^{*} \right) U_{i} \, d\Omega \right]$$

$$- \int_{\Gamma} N_{\alpha} \left(U_{i} + \frac{1}{2} \Delta U_{i}^{*} \right) n_{i} \, d\Gamma \right]^{n}$$

$$- \frac{\Delta I^{2}}{2} \left[\int_{\Omega} \frac{\partial N_{\alpha}}{\partial x_{i}} \frac{\partial \rho}{\partial x_{i}} \, d\Omega - \int_{\Gamma} N_{\alpha} \frac{\partial \rho}{\partial x_{i}} n_{i} \, d\Gamma \right]^{n} \dots (13)$$

Step 3: The momentum correction equations,

$$\int_{\Omega} N_{\alpha} \Delta U_{i} d\Omega =$$

$$\int_{\Omega} N_{\alpha} \Delta U_{i}^{*} d\Omega + \Delta t \left[\int_{\Omega} \frac{\partial N_{\alpha}}{\partial x_{i}} p d\Omega - \int_{\Gamma} N_{\alpha} p n_{i} d\Gamma \right]^{n} \dots (14)$$

Step 4: The energy equation,

$$\int_{\Omega} N_{\alpha} \Delta \rho \varepsilon d\Omega = \frac{1}{\Delta t} \int_{\Omega} \frac{\partial N_{\alpha}}{\partial x_{j}} \left(u_{j} (\rho \varepsilon + p) \right) d\Omega - \int_{\Gamma} N_{\alpha} \left(u_{j} (\rho \varepsilon + p) \right) n_{i} d\Gamma \right]^{n} - \frac{\Delta t^{2}}{2} u_{k} \left[\int_{\Omega} \frac{\partial N_{\alpha}}{\partial x_{k}} \frac{\partial \left(u_{j} (\rho \varepsilon + p) \right)}{\partial x_{j}} d\Omega \right]^{n} + \int_{\Gamma} N_{\alpha} \frac{\partial \left(u_{j} (\rho \varepsilon + p) \right)}{\partial x_{j}} n_{k} d\Gamma \right]^{n} \qquad \therefore (15)$$

The finite element equations in matrix form can then be derived by substituting Eq. (11) into Eqs (12)-(15) to give,

Step 1: The intermediate momentum equations,

$$[M] \{ \Delta U_i^* \} = \Delta t ([C] \{ u_j U_i \} - \{ R_u \})^n$$

$$- \frac{\Delta t^2}{2} u_k ([K_u] \{ u_j U_i \} + [K_p] \{ p \} - \{ R_{\mu i} \} - \{ R_{\rho i} \})^n$$
... (16)

Step 2: The continuity equation,

$$[M]\{\Delta\rho\} = \Delta t \left[[D] \left\{ U_i + \frac{1}{2} \Delta U_i^* \right\} - \left\{ S_u \right\} \right]^n$$

$$-\frac{\Delta t^2}{2} \left([K] \left\{ p \right\} - \left\{ S_p \right\} \right)^n \qquad \dots (17)$$

Step 3: The momentum correction equations,

$$[M]\{\Delta U_i\} = [M]\{\Delta U_i^*\} + \Delta t ([D]\{p\} - \{T_p\})^n \dots (18)$$

Step 4: The energy equation,

$$[M] \{ \Delta \rho \varepsilon \} = \Delta t ([C] \{ u_j (\rho \varepsilon + p) \} - \{ R_{\varepsilon} \})^n$$

$$- \frac{\Delta t}{2} u_k ([K_u] \{ u_j (\rho \varepsilon + p) \} + \{ R_{\varepsilon s} \})^n \qquad \dots (19)$$

In the above equations, the element matrices written in the integral form are,

$$[M] = \int_{\Omega} \{N\} \lfloor N \rfloor d\Omega \qquad \dots (20a)$$

$$[C] = \int_{\Omega} \left\{ \frac{\partial N}{\partial x_{j}} \right\} [N] d\Omega \qquad \dots (20b)$$

$$[D] = \int_{\Omega} \left\{ \frac{\partial N}{\partial x_i} \right\} [N] d\Omega \qquad ... (20c)$$

$$[K_{\mu}] = \int_{\Omega} \left\{ \frac{\partial N}{\partial x_{k}} \right\} \left| \frac{\partial N}{\partial x_{j}} \right| d\Omega \qquad \dots (20d)$$

$$\left[K_{p}\right] = \int_{\Omega} \left\{\frac{\partial N}{\partial x_{k}}\right\} \left[\frac{\partial N}{\partial x_{i}}\right] d\Omega \qquad \dots (20e)$$

$$[K] = \int_{\Omega} \left\{ \frac{\partial N}{\partial x_i} \right\} \left[\frac{\partial N}{\partial x_i} \right] d\Omega \qquad \dots (20f)$$

$$\{R_{u}\} \simeq \int_{\Gamma} \{N\} (u_{j}U_{i}) n_{j} d\Gamma \qquad \dots (20g)$$

$$\{R_{us}\} = \int_{\Gamma} \{N\} \frac{\partial (u_j U_i)}{\partial x_j} n_k d\Gamma \qquad ... (20h)$$

$$\left\{ R_{\rho x} \right\} = \int_{\Gamma} \left\{ N \right\} \frac{\partial p}{\partial x_i} n_k \, d\Gamma \qquad \qquad \dots (20i)$$

$$\{S_{\nu}\} = \int_{\Gamma} \{N\} \left(U_{i} + \frac{1}{2}\Delta U_{i}^{*}\right) n_{i} d\Gamma \qquad \dots (20j)$$

$$\left\{S_{\rho}\right\} = \int_{\Gamma} \left\{N\right\} \frac{\partial p}{\partial x_{i}} n_{i} d\Gamma \qquad \dots (20k)$$

$$\left\{T_{\rho}\right\} = \int_{\Gamma} \left\{N\right\} p \, n_i \, d\Gamma \qquad \qquad \dots \tag{201}$$

$$\{R_{\varepsilon}\} = \int_{\varepsilon} \{N\} (u_{j}(\rho \varepsilon + p)) n_{j} d\Gamma \qquad \dots (20m)$$

$${R_{ss}} = \int_{\Gamma} {N} \frac{\partial (u_{j}(\rho \varepsilon + p))}{\partial x_{j}} n_{k} d\Gamma$$
 ... (20n)

An artificial diffusion is also needed to reduce the oscillation in the vicinity of sharp gradients of the solutions. The second derivative of pressure¹² is selected to contribute the artificial diffusion into nodal quantities. These nodal artificial diffusions are determined from.

$$\left[M\right]\left\{\frac{U_{s}^{n+1}-U^{n+1}}{\Delta t}\right\}=C_{\epsilon}h^{3}\frac{\left|V\right|+c}{\overline{p}}\left|\nabla^{2}p\right|_{\epsilon}\left[K\right]\left\{U\right\}^{n}...(21)$$

where U_s^{n+1} is the modified solution at time step n+1 after adding artificial diffusion, U_s^{n+1} is the solution at time step n+1, C_e is the user-specified coefficient which varies between 0 and 2, h is the element size, |V| is the absolute velocity, c is the speed of sound, \bar{p} is the average pressure, and $|\nabla^2 p|_e$ is the second derivative of pressure over the element. The fully explicit form of the characteristic-based split algorithm is conditionally stable. The permissible time step is given by,

$$\Delta t = \sigma \frac{h}{|V| + c} \qquad \dots \tag{22}$$

where σ is the Courant number $(0 < \sigma \le 1)$.

Adaptive Mesh Regeneration

Mesh adaptation procedure

In high-speed compressible flows, the flow properties, such as the density and pressure, change abruptly across the shock waves. Small elements are thus needed along the shock waves to provide good flow resolution. The second derivatives of any key variable ϕ , such as density is used to determine the proper element sizes¹ that is, small elements are placed in the region where changes in the variable gradients are large. Elements which will be either refined or coarsened by Adaptive Remeshing algorithm, are identified by a dimensionless error indicator using the pressure-switch coefficient¹³. The indicator at node I is given by,

$$E_{I} = \frac{\sum_{\alpha \in I} |2\phi_{I} - \phi_{J} - \phi_{K}|}{\sum_{\alpha \in I} (A^{*} + B^{*})} \dots (23)$$

where J and K are the other two nodes of the triangle, $A^* = \max(|\phi_I - \phi_J|, \alpha(\phi_I + \phi_J))$ and $B^* = \max(|\phi_I - \phi_K|, \alpha(\phi_I + \phi_K))$. The value of α is prescribed as .005 in this paper, which means $A^* = .005(\phi_I + \phi_J)$ and $B^* = .005(\phi_I + \phi_K)$ if ϕ_J and ϕ_K are oscillated within 1% of ϕ_J , respectively.

Practical experience found that this type of error indicator for complex high-speed compressible flow problems, where regions such as shock or discontinuity have different strength, may cause inaccurate solution from inadequate refinement because the point spacing is scaled according to the maximum value of the second derivatives. To overcome this problem, an element size scaling function, which scales the point spacing of point p_i between minimum and maximum element sizes, h_{min} and h_{max} , within the range of χ_{min} and χ_{max} , has been used,

$$\chi_{i} = \text{ScaleRange}\left(\frac{h_{\text{max}} - dp_{i}}{h_{\text{max}} - h_{\text{min}}}, 0, 1, \chi_{\text{min}}, \chi_{\text{max}}\right)$$
... (24)

where dp_i is nodal distribution value of node i.

The coefficient χ_i controls the point insertion in the regions of high solution gradient and eliminates undue distortion of the triangle regularity. The value of χ_{\min} limits number of points insertion in high gradient region such as shock, while the value of upper limit χ_{\max} allows more points to be inserted into the lower solution gradient region. As shapes of adapted elements generated by this function may be distorted, the Alpha

End:

and Beta coefficients⁷ are incorporated as coefficients of such function to control point density and the regularity of triangulation.

The proposed adaptive mesh regeneration is based on the concepts of the Delaunay triangulation and the mesh refinement as described by Algorithm I and II⁷. The new mesh is constructed using the information from the previous or background mesh, such that it is composed of small elements in the regions with large changes of solution gradients, and large elements in the other regions where the changes of solution gradients are small. The proposed algorithm is terminated when number of inserted points in each iteration is less than some threshold values, between 2 to 5 points. Detailed process of adaptive remeshing technique is shown and described in the algorithm as follows.

Algorithm III; Adaptive Remeshing (P, T, P0, alpha beta, _ Hmin, Hmax, Xi_min, _ Xi_max, threshold)

Do f

```
Do p \leftarrow P0.NextInteriorNode {
             If (p.hi \leq Hmax) {
               t \leftarrow T.FindTriangleContainNode(p);
               pq \leftarrow t.ComputeTriangleCentroid();
               pq.dp \leftarrow t.ComputePointDistribution
               Function(); pq.dm(1:3) \leftarrow t.Distance
               CentroidToVertices(); sclcoef = Scale
               Range((Hmax - pq.dp) / \_
               (Hmax - Hmin), 0, 1, Xi_min,
               Xi_max);
               If ((sclcoef * lalpha * pq.dp) <
               pq.dm.Average) {
               var = sclcoef * Hmin / beta;
               If Not(((pq.dm(1) < var))
               And (pq.dm(2) < var)) Or _
               ((pq.dm(2) < var) And (pq.dm(3))
               < var)) Or _
               ((pq.dm(3) < var) And (pq.dm(1)
               < var)))
               P.AddNodeAsInsertedNode(pq);
                };
             };
          };
          Do p \leftarrow P.NextInsertedNode {
          Call DelaunayTriangulation(P, T, p);
           1;
} Loop Until (P.InsertedNodes <= threshold);</pre>
```

The above algorithm III can be described in order as follows;

Algorithm III; AdaptiveRemeshing

- 1 Let user-specified threshold be the minimum number of points required in each point iteration loop to continue this algorithm.
- Let P0, k = 1, ..., n be the set of points of the background mesh.
- 3 Let P be the set of points and T be the set of triangles.
- 4 Read next interior point p_i of the background mesh from P0.
- 5 If $h_i > h_{max}$ then go to step 4.
- Search triangle t_i in T which contains the point p_i . Then calculate the centroid of the triangle t_i and define it as point p_q , and compute the point distribution function of point p_q .
- 7 Compute the distance d_m , m = 1, 2, 3 from point p_q to each of the three vertices of the triangle t_l .
- 8 Compute the Xi coefficient, χ_p for point p_i by using Eq. (24), and the average distance, $s_i = (d_1 + d_2 + d_3) / 3$.
- Perform the Xi-Alpha test for point p_q . If $(\chi_i * alpha * h_i) \ge s_i$, then reject the point p_q and return to step 4.
- 10 Perform the Xi-Beta test for point p_q . If two out of three of $d_m < (\chi_i * h_{min} / beta)$ for any m = 1, 2, 3, then reject the point p_q and return to step 4.
- 11 Accept the point p_q for insertion by the Delaunay triangulation algorithm and add point p_q into p
- 12 Repeat steps 4 to 11 until all points in P are considered.
- 13 Perform the Delaunay triangulation of the inserted points in P.
- 14 If number of inserted points is greater than *threshold*, then go to step 3; otherwise stop the algorithm.

The proposed algorithm above does not guarantee the good mesh topology. The mesh relaxation ¹⁴ based on an edge-swapping technique is highly recommended for well-shaped mesh improvement. The objective of this method is to make the topology of elements closer to equilateral triangles by swapping edges to equalize the vertex degrees (number of edges linked to each point) toward the value of six. Finally, the Laplacian smoothing is applied to smooth the mesh.

Algorithm evaluation

To evaluate the performance of the adaptive remeshing technique with the Delaunay triangulation algorithm, the specification of element size, h_0 is given as an analytical function for two-dimensional domain. The adaptive mesh generation process first generates an initial mesh from the domain, then the values of the element sizes at all points are computed by the given function. The mesh generation coupled with the adaptive remeshing procedure is repeated until the resulting mesh is globally stable. The three examples of adaptive mesh generation with the analytical element size-specification function presented herein are: (i) adaptive meshes along centerline of a rectangular domain, (ii) adaptive meshes along a diagonal of a square domain, and (iii) alpha-shape adaptive meshes in a square domain.

Adaptive Meshes along Centerline of a Rectangular Domain: The first example presents an adaptive mesh generation in a 3×5 rectangular domain. The element sizes at positions in the domain are given by the distribution function,

$$h(y) = 0.42 - \frac{1}{\sqrt{2\pi}\sigma} e^{-\left[\frac{y-\mu}{2\sigma}\right]^2}$$
 ... (25)

where y is the variable and the values of μ and σ are constants equal to zero and one, respectively. Fig. 1 shows a series of the meshes generated by three successive adaptation from the coarse initial mesh. The value of mesh generation coefficients, α , β , χ_{min} , χ_{max} are 0.5, 0.6, 0.75, and 1.10, respectively. Due to the prescribed distribution function, Eq. (25), small element sizes are specified around the centerline of the domain. The figures show the pattern of graded elements along narrow band around the centerline of the domain. The value of χ_{min} limits number of points insertion along centerline of the domain, while the value

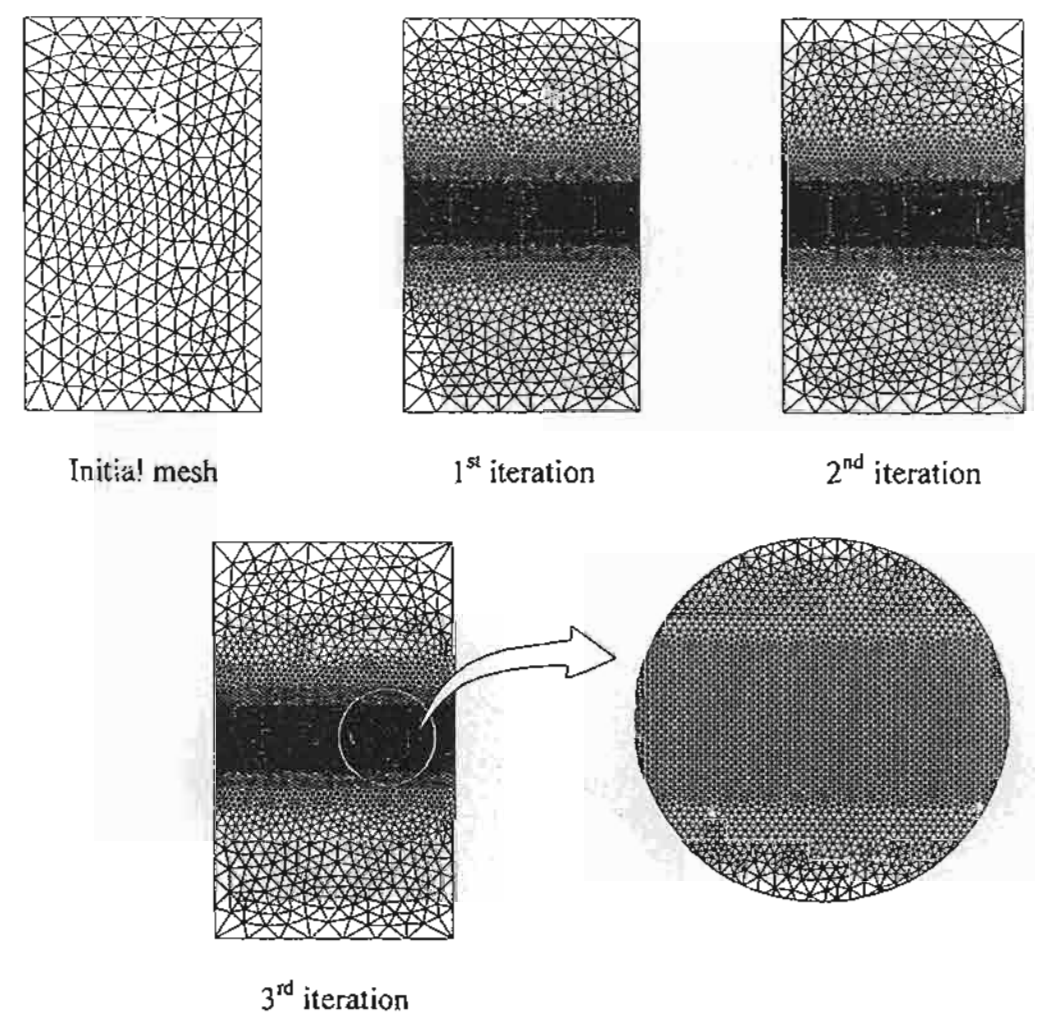


Fig. 1—Adaptive meshes along centerline of a rectangular domain.

of χ_{max} allows more nodes to be inserted into the other regions.

The specification of scale range and limiting χ , χ_{min} and χ_{max} , have strong effects on the resulting meshes as shown in Fig. 2. Without the scale range, the mesh is composed of small elements concentrated around line a (see Fig. 2) with progressively larger elements outwards as $h_a < h_b$, h_c . The scale range function sorts the nodal spacing values into prescribed intervals according to χ_{min} and χ_{max} . In each interval, the generated element sizes are relatively uniform. With them,

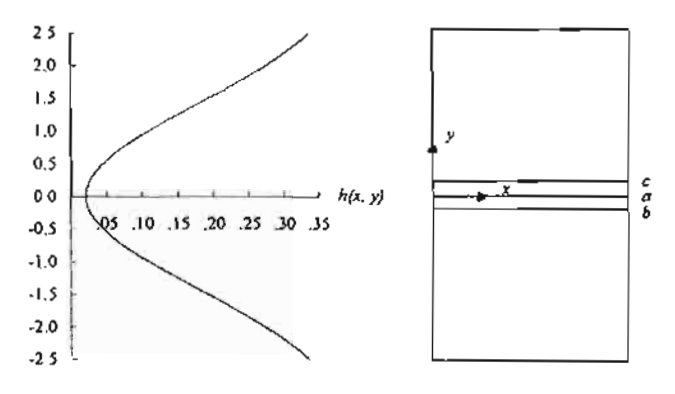


Fig. 2-Distribution of element sizes along the y direction.

a mesh consisting of relatively uniform elements in a wider centerline band of the domain is generated. This mesh has better physical correlation with the behaviours of shocks.

Adaptive Meshes along a Diagonal of a Square Domain: The second example concerns with an adaptive mesh generation in a unit square domain. The element sizes are calculated by the function in Eq. (26) where the constant α is equal to 0.5 for this test case⁷.

$$h(x,y) = 2y(1-y) \left[\tan^{-1} \beta - \frac{\alpha(1-2x)}{\sqrt{2}(1+\beta^2)} + \frac{\alpha^2 \beta x(1-x)}{2(1+\beta^2)^2} \right] + 2x(1-x) \left[\tan^{-1} \beta - \frac{\alpha(1-2y)}{\sqrt{2}(1+\beta^2)} + \frac{\alpha^2 \beta y(1-y)}{2(1+\beta^2)^2} \right] \dots (26)$$

where $\beta = \alpha[(x+y)/\sqrt{2} - 0.8]$.

Because this function generates both negative and positive values, the only positive values of this function are used to determine the element size by scaling into the new range of 0.001 and 0.2. Fig. 3 shows the sequence of adaptive meshes generated by five itera-

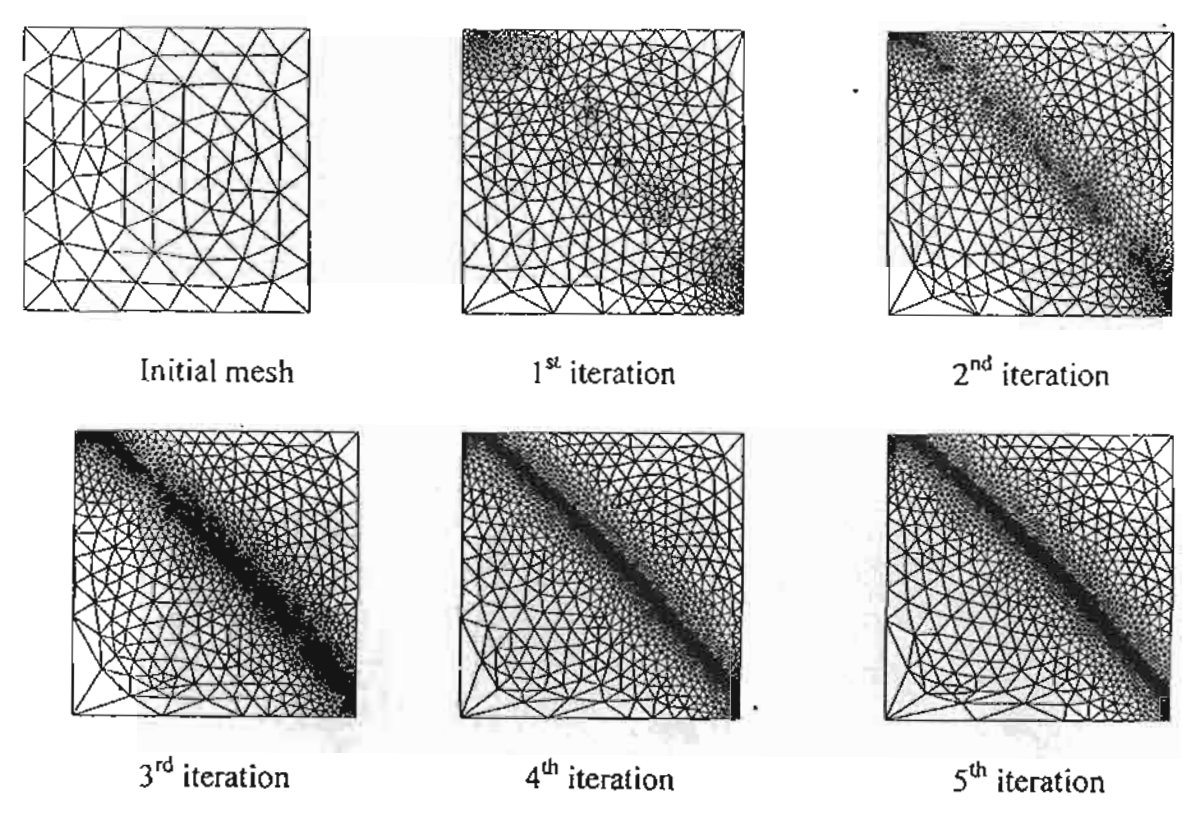


Fig. 3-Adaptive meshes along a diagonal of a square domain.

tions based on a coarse initial mesh. The value of mesh generation coefficients, α , β , χ_{min} , χ_{max} are 0.5, 0.6, 0.4, and 0.75, respectively. The combination of the values of χ_{min} and χ_{max} , narrows the band along the diagonal line with small elements.

Alpha-Shape Adaptive Meshes in a Square Domain: The third example generates an alpha-shape adaptive mesh in a square domain as shown in Fig. 4. The alpha shape function 15 is used to calculate element sizes in an 8 × 8 square domain,

$$h(x,y) = \begin{cases} \min(0.2(\lambda - 1)^3 + 0.005, 1.0) & \text{if } \lambda \ge 1\\ \min(0.2(\lambda - 1)^2 + 0.01, 1.0) & \text{if } \lambda < 1\\ & \dots (27) \end{cases}$$

where the value of parameter λ is determined from $x^3 - y^2 + 2 - 3\lambda x = 0$. The value of mesh generation coefficients, α , β , χ_{min} , χ_{max} are 0.5, 0.6, 0.5, and 0.85, respectively.

Results and Discussion

To demonstrate the capability of the combined characteristic-based split algorithm and the adaptive remeshing technique for increasing the flow solution accuracy, four simulations of the high-speed inviscid compressible flows are used: (i) Sod shock tube, (ii) an oblique shock reflection at a wall, (iii) a Mach 2

flow in a channel with compression and expansion ramps, and (iv) a shock-shock interaction on a cylinder.

Sod shock tube

The first example, used for evaluating the combined characteristic-based split algorithm and adaptive remeshing technique, is the Sod shock tube 16. This example was selected because it has exact solutions for comparison. The problem statement is described by Fig. 5, the initial conditions of the fluids on the left and right regions are given by $(\rho, \mu, p)_L = (1.0, \mu, p)_L = (1.0,$ 0.0, 1.0) and $(\rho, u, p)_R = (0.125, 0.0, 0.1)$. Figs 6 (a-c) show a transient adaptive mesh which consists of 32,091 nodes and its corresponding computed density and pressure contours. Figs 7(a-c) compare the computed density, pressure and u-velocity along the tube length with the exact solutions at time t = 0.1. The figures show the combined procedure can capture abrupt changes of the solutions across the shocks wave very well.

An oblique shock reflection at a wall

The problem statement of a steady-state oblique shock reflection at a wall is described in Fig. 8. The Mach 2.9 and 2.378 flows enter through the left and the top boundaries of the computational domain resulting in an oblique shock from the top-left corner. This shock incidents and reflects at a wall as high

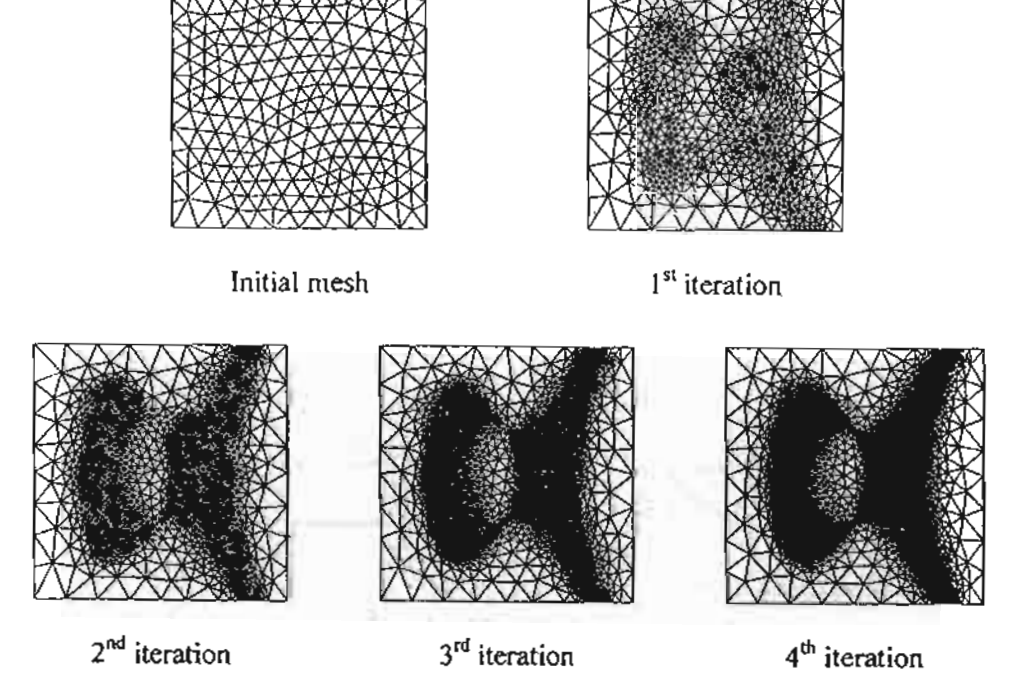


Fig. 4-An alpha-shape adaptive meshes in a square domain.

lighted in the figure. The boundary conditions along the left side of the computational domain are given by $\rho = 1.0$, u = 2.9, v = 0, $\varepsilon = 5.990714$; and the upper side are given by $\rho = 1.7$, u = 2.619334. v = -0.506320, $\varepsilon = 5.805957$. The slip condition is imposed on the lower side and none of flow variables is specified on the right side. The combined procedure starts by creating a relatively smooth initial meshes as shown in Fig. 9a that consists of 2,561 nodes. The fluid analysis is then performed to generate the corresponding solution such as the density contours as shown in Figs 9(b-c). The figure shows the computed shock is not sharp because the elements along the shock lines are not small enough. This flow solution is then used to generate an adaptive mesh to cluster small elements in the regions of sharp changes of the density gradients, and at the same time, to use larger elements on the other regions. The fluid analysis is then performed again to yield a more accurate solution. The entire process is repeated to generate the third adaptive mesh consisting of 9,989 nodes and the

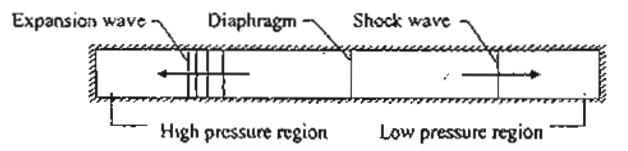


Fig. 5-Problem statement of a shock wave propagation in a tube

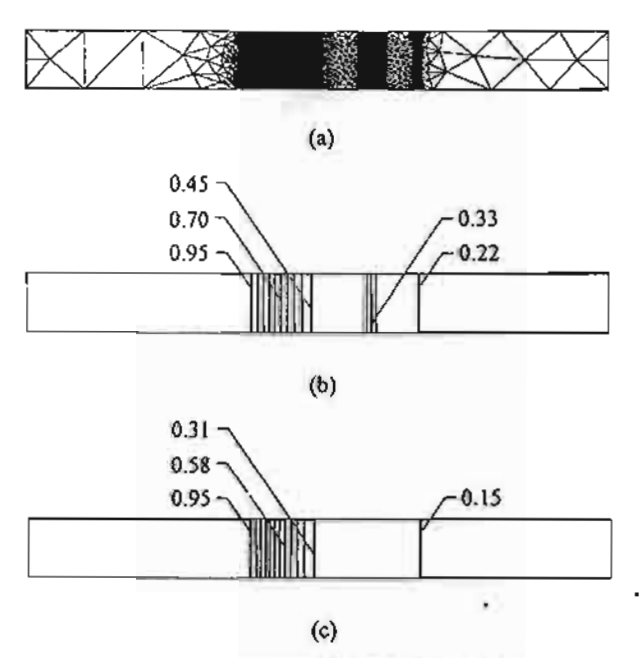


Fig. 6—A shock wave propagation in a tube: (a) adaptive mesh; (b)-(c) corresponding density and pressure contours at time t = 0.1.

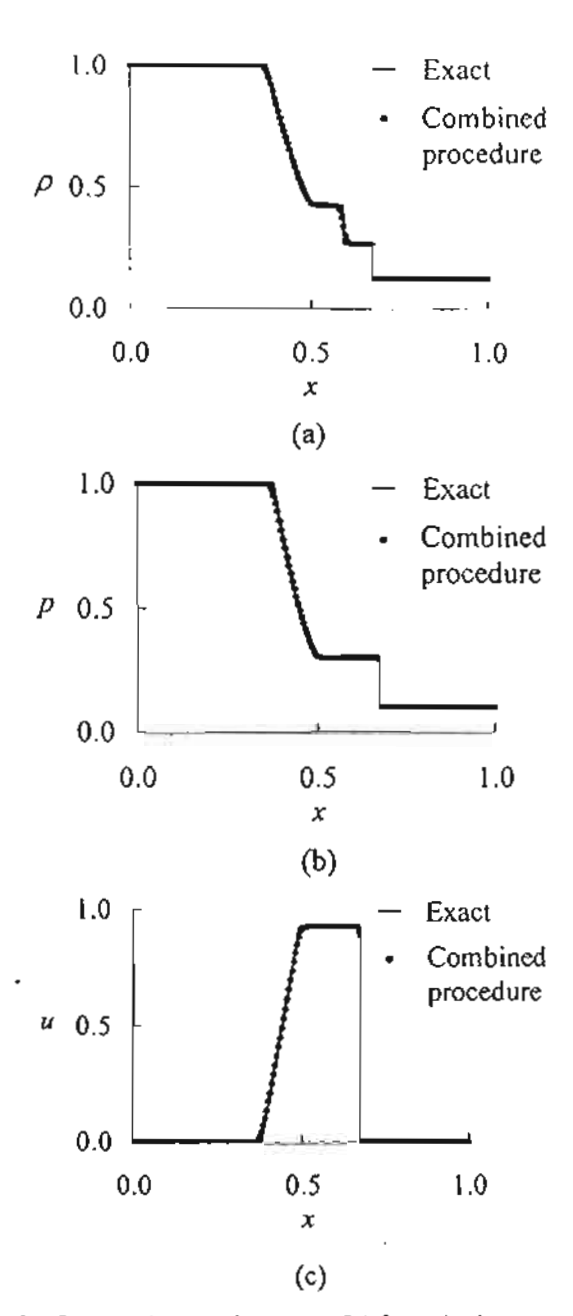


Fig. 7—Comparative solutions at t = 0.1 for a shock wave propagation in a tube: (a) density distribution; (b) pressure distribution; (c) u-velocity distribution.

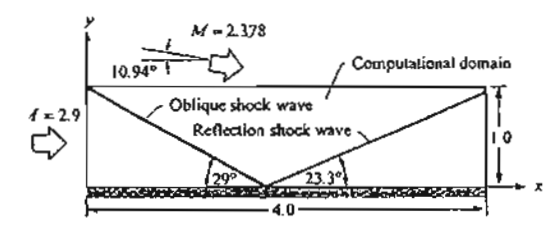


Fig. 8—Problem statement of an oblique shock reflection at a wall.

corresponding density contours as shown in Figs 9(d-e), respectively. Figs 10(a-b) illustrate the effect of C_c on the predicted density and pressure as compared to the exact solutions. Figs 11(a-(b)) show the improvement of the shock resolution from the third adaptive mesh by comparing with the exact solution and the initial mesh solution at y = 0.25.

Mach 2 flow in a channel with compression and expansion ramps

The problem statement of a Mach 2.0 in a channel with compression and expansion ramps and the sketch

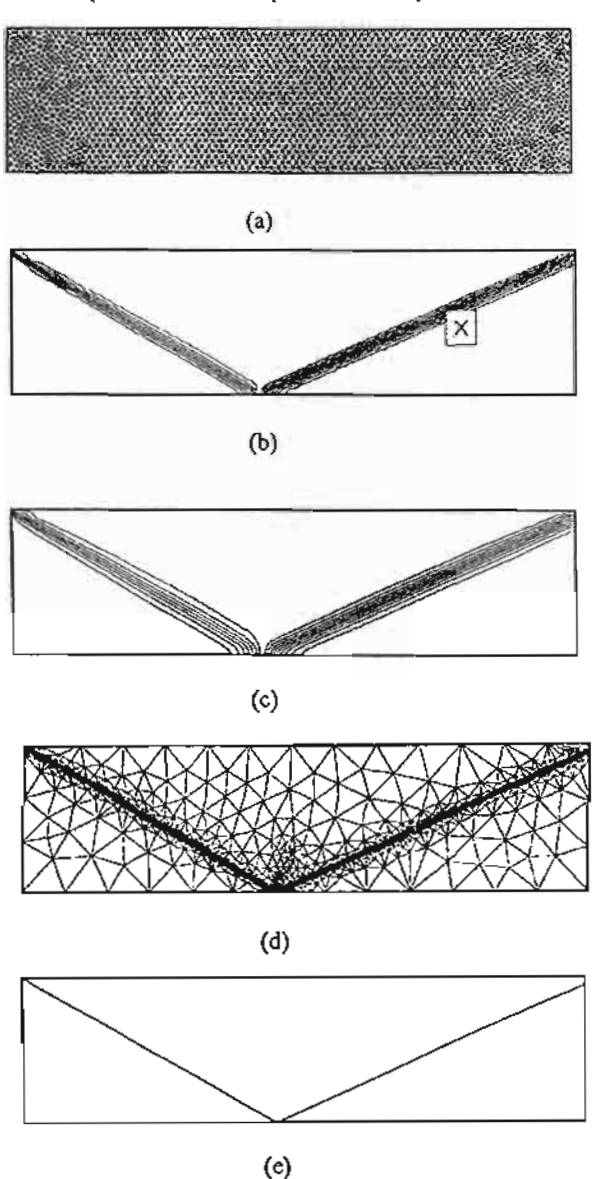


Fig. 9—An oblique shock reflection at a wall: (a) initial mesh; (b)-(c) the corresponding density contours with $C_e = 0.5$, 2.0; and (d)-(c) third adaptive mesh and the corresponding density contours.

of the flow behaviour are described in Fig. 12. The flow creates an oblique shock from the compression ramp that impinges on the upper wall resulting in a reflecting shock. The reflecting shock also intersects with the Mach waves generated from the expansion corner. The boundary conditions along the left side of computational domain are given by $\rho = 1.0$, u = 1.0, v = 0, $\varepsilon = 0.946429$. The upper and lower sides of the domain are specified by the slip condition while none of the variables is specified on the right side. The final adaptive mesh consisting of 13,387 nodes is shown in Fig. 13a. The corresponding density, pressure and Mach number contours are shown in Figs 13(b-d), respectively. The figures highlight good quality of the predicted solutions with sharp shock lines and clear Mach wave. The comparisons of the

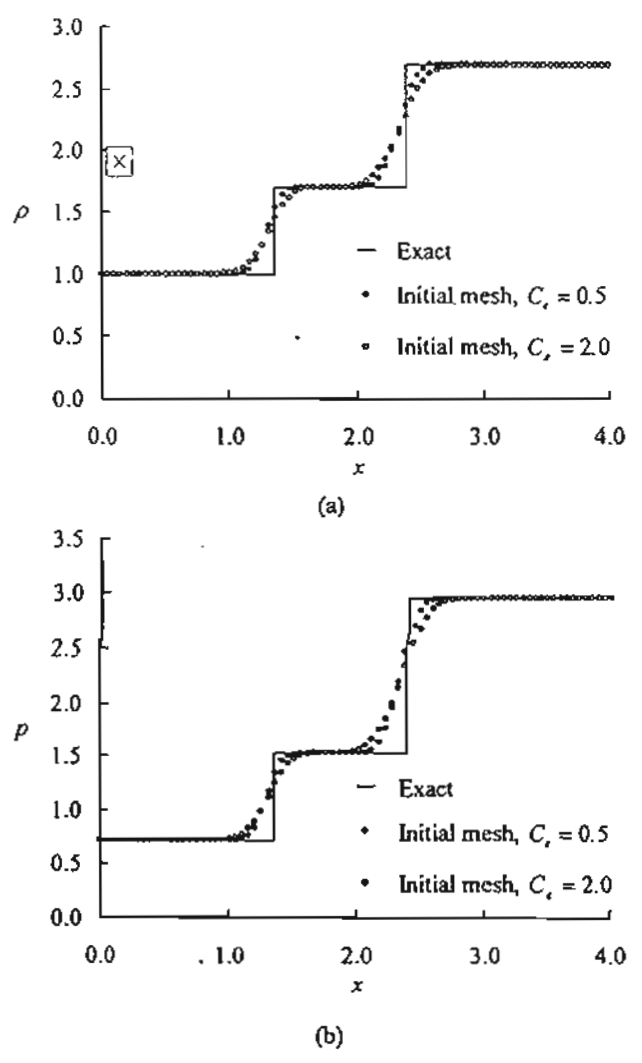


Fig. 10—Effect of C_r on the solutions at y = 0.25 for an oblique shock reflection at a wall: (a) density distribution; and (b) pressure distribution.

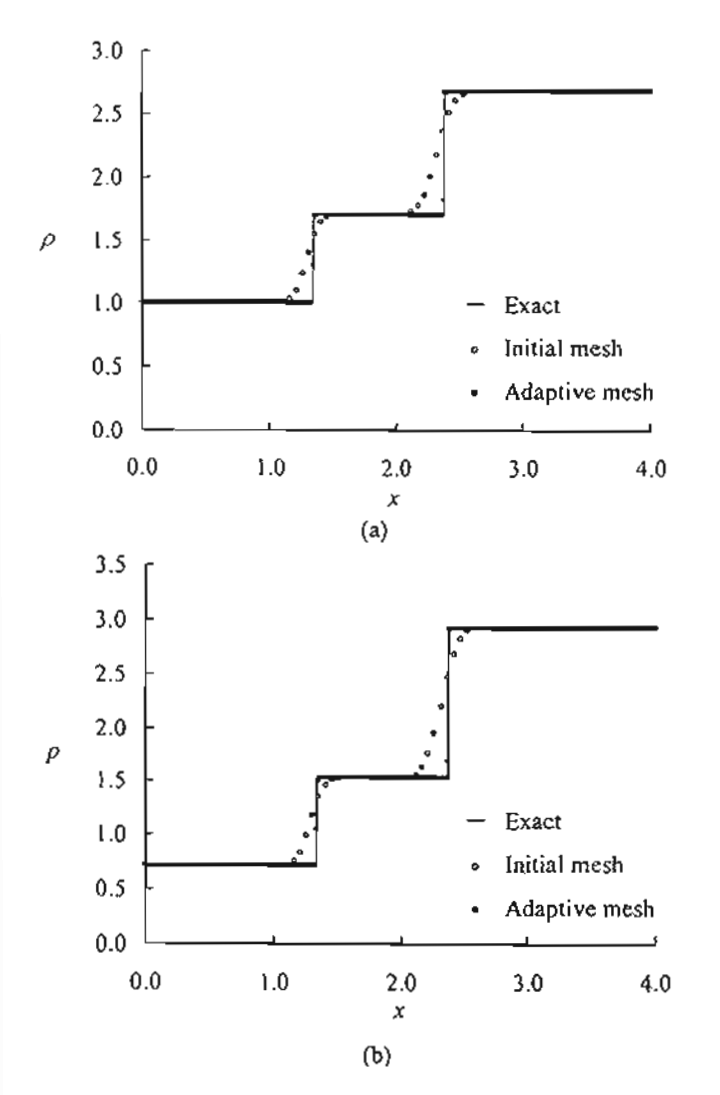


Fig. 11—Comparative solutions at y = 0.25 for an oblique shock reflection at a wall: (a) density distribution; and (b) pressure distribution.

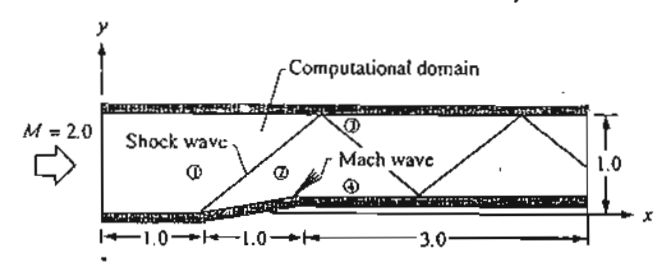


Fig. 12—Problem statement of a Mach 2.0 in a channel with compression and expansion ramps.

analytical solutions, the numerical solutions¹⁷ and the present numerical results are given in Table I. The table shows the Mach number at the four state locations are in excellent agreement with the analytical solutions. This example demonstrates the capability of

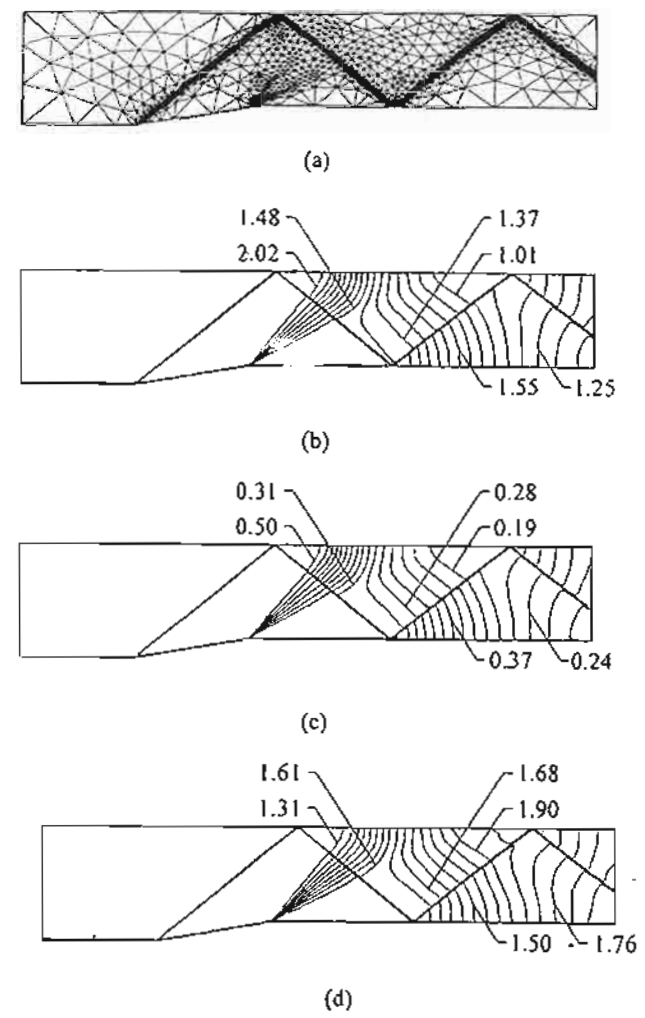


Fig. 13—Mach 2.0 in a channel with compression and expansion ramps: (a) final adaptive mesh; (b) corresponding density contours; (c) pressure contours; (d) Mach number contours.

Table 1— Comparison of analytical and numerical solutions at the four state locations (Fig. 12) of the flow in a channel with compression and expansion ramps

State location	Analytical Mach number	Present (% difference)	Ref . (17) (% difference)
i	2.00	2.000 (0.0)	2.000 (0.0)
2	1.65	1.640 (0.6)	1.639 (0.7)
3	1.30	1.290 (0.8)	1.287 (1.0)
4	2.00	1.982 (0.9)	1.985 (0.8)

the combined characteristic-based split algorithm and the adaptive remeshing technique to provide flow solution for general flow behaviour that is not known a priori.

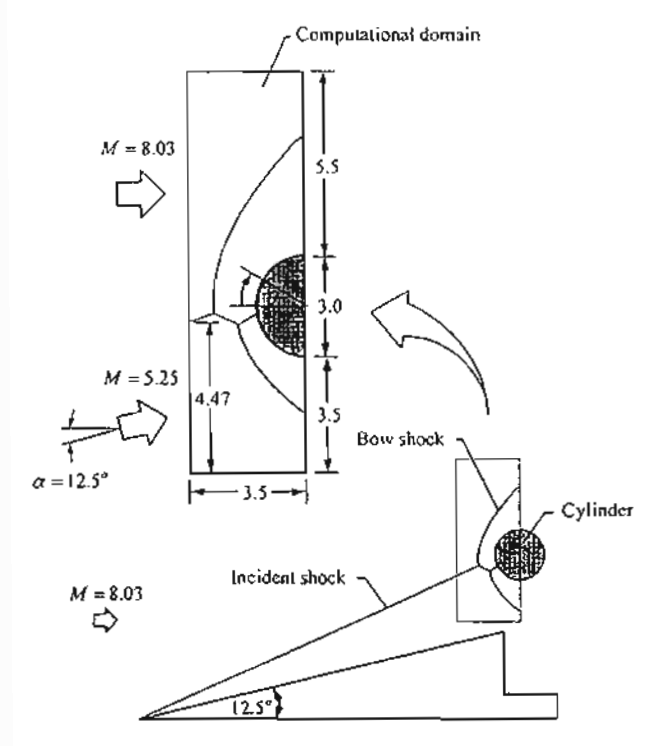


Fig. 14—Problem statement of a shock-shock interaction on a cylinder.

Shock-shock interaction on a cylinder

The problem statement of a shock-shock interaction behaviour in front of a cylinder is shown in Fig. 14. An incident shock generated from a Mach 8.03 flow over a wedge interacts with the bow shock of the cylinder resulting in a shock-shock interaction phenomenon. Such phenomenon is quite complex for which the interaction pattern is not known a priori. The inlet flow conditions of upper left side of the domain consist of specifying $\rho = 2.879051E-9$ lbf s^2/in^4 , u = 6.693240E+4 in/s, v = 0 in/s, and $\varepsilon =$ 2.364019E+9 in²/s²; the lower left side of domain are given by $\rho = 9.596836E-9 \text{ lbf-s}^2/\text{in}^4$, u =6.240757E+4 in/s, $\nu = 1.383542E+4$ in/s, and $\varepsilon =$ 2.307711E+9 in²/s². The slip condition is imposed on the surface of the cylinder while none of the flow variables is specified on the other sides. The combined procedure with the adaptive meshing technique was applied to solve for such flow solution. The final adaptive mesh consisting of 20,332 nodes and 40,359 elements is shown in Fig. 15a. The corresponding computed pressure and Mach number contours are presented in Figs 15(b-c), respectively. Fig. 16 shows the computed pressure distribution on the surface of the cylinder as compared to the experimental data18. The predicted and experimental pressure distributions

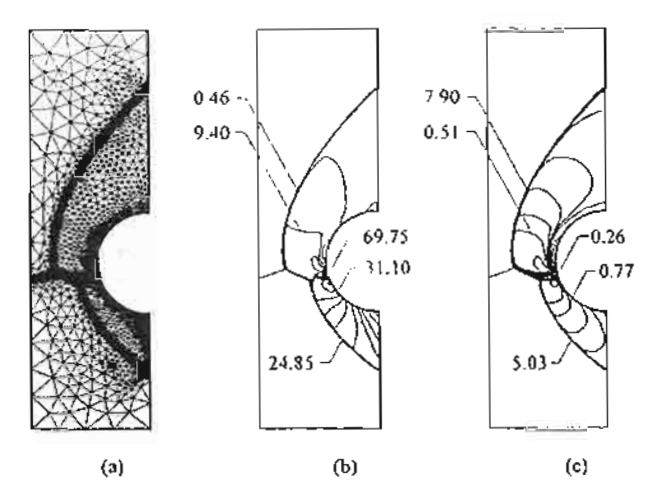


Fig. 15—Shock-shock interaction on a cylinder: (a) adaptive mesh; (b)-(c) corresponding pressure and Mach number contours.

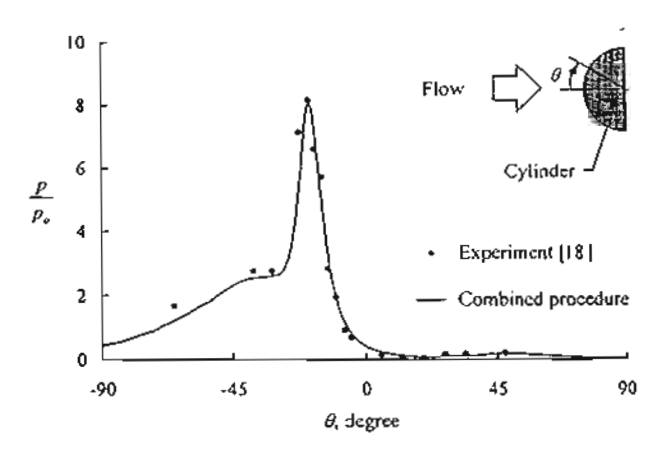


Fig. 16— Comparative pressure distributions along cylinder sur-

are normalized by the undisturbed flow (no shock interaction) stagnation pressure. The figure shows good agreement of the pressure distributions and excellent agreement of the peak pressure location.

Conclusions

The combined procedure of the finite element method based on the characteristic-based split algorithm and the adaptive Delaunay triangulation algorithm for the analysis of high-speed inviscid compressible flow was presented. The characteristic-based split algorithm for solving the Euler equations was described first. The concept of the Delaunay triangulation for two-dimensional mesh construction was then explained. The mesh generation procedure with automatic point creation and mesh smoothing were developed and described. The solution accuracy was improved by incorporating an adaptive remeshing

technique to the Delaunay triangulation algorithm. The adaptive remeshing technique places small elements in the regions with large changes of flow solution gradients, and at the same time, larger elements are generated in the other regions. Four examples of high-speed inviscid compressible flows were presented to assess the effectiveness of the combined procedure. These examples are a shock wave propagation in tube, an oblique shock reflection at a wall, a Mach 2.0 flow in a channel with compression and expansion ramps, and a shock-shock interaction on a cylinder. The results demonstrate that the combined procedure can provide high solution accuracy with reduced computational time and memory for analysis of high-speed compressible flow problems.

Acknowledgements

The authors acknowledge the Thailand Research Fund (TRF) for supporting this research work.

References

- Anderson J D, Modern compressible flow with historical prospective, 2nd Ed (McGraw-Hill, New York), 1990.
- Donea J, Int J Numer Methods Eng, 20 (1984) 101-119.

- Huges T J R. Int J Numer Methods Fluids, 7 (1987) 1261-1275.
- 4 Jiang B N & Carey G F, Int J Numer Methods Fluids, 8 (1988) 933-942.
- 5 Gnoffo P A, AIAA Paper 86-0565, 1986.
- 6 Zienkiewicz O C & Codina R, Int J Numer Methods Fluids, 20 (1995) 869-885.
- Phongthanapanich S & Dechaumphai P, Indian J Eng Mater Sci. 10 (2003) 245-260.
- 8 Bowyer A, Comput J, 8 (1981) 162-166.
- 9 Watson D F, Comput J, 24 (1981) 167-172.
- 10 Satya Sai B V K, Zienkiewicz O C, Manzari M T, Lyra P R M & Morgan K, Int J Numer Methods Fluids, 27 (1998) 57-80.
- 11 Zienkiewicz O C & Taylor R L, The Finite Element Method, 5th Ed (Butterworth-Heinemann), 2000.
- 12 Nithiarasu P, Zienkiewicz O C, Satya Sai B V K, Morgan K, Codina R & Vazquez M, Int J Numer Methods Fluids. 28 (1998) 1325-1353.
- 13 Probert J, Hassan O, Peraire J & Morgan K, Int J Numer Methods Eng., 32 (1991) 1145-1159.
- 14 Frey W H, Int J Numer Methods Eng, 31 (1991) 1121-1133.
- 15 Borouchaki H, George P L & Mohammadi B, Finite Elem Anal Des, 25 (1997) 85-109.
- 16 Sod G A, J Comput Phys, 57 (1978) 1-31.
- 17 Ripley R C, Lien F S & Yovanovich M M, Int J Comput Fluid Dyn, 18 (2004) 189-198.
- 18 Dechaumphai P, Thornton E A & Wieting A R, J Spacecraft Rockets, 26 (1989) 201-209.

บทความทางวิชาการ เรื่อง

Nodeless Variable Finite Element Method and Adaptive Meshing Technique for Viscous Flow Analysis

Published in the

Journal of Mechanical Science and Technology

Vol. 20, No. 10, pp. 1730-1740 2005

Nodeless Variables Finite Element Method and Adaptive Meshing Teghnique for Viscous Flow Analysis

Archawa Paweenawat, Pramote Dechaumphai*

Mechanical Engineering Department, Chulalongkorn University,

Bangkok 10330, Thailand

The Separate Volume of Journal of Mechanical Science and Technology

Nodeless Variables Finite Element Method and Adaptive Meshing Teghnique for Viscous Flow Analysis

Archawa Paweenawat, Pramote Dechaumphai*

Mechanical Engineering Department, Chulalongkorn University, Bangkok 10330, Thailand

A nodeless variables finite element method for analysis of two-dimensional, steady-state viscous incompressible flow is presented. The finite element equations are derived from the governing Navier-Stokes differential equations and a corresponding computer program is developed. The proposed method is evaluated by solving the examples of the lubricant flow in journal hearing and the flow in the lid-driven cavity. An adaptive meshing technique is incorporated to improve the solution accuracy and, at the same time, to reduce the analysis computational time. The efficiency of the combined adaptive meshing technique and the nodeless variables finite element method is illustrated by using the example of the flow past two fences in a channel.

Key Words: Finite Element Method, Incompressible Flow, Nodeless Variables, Adaptive Meshing Technique

1. Introduction

The finite element method has been widely and successfully used as a tool for analyzing both the solid mechanics and heat transfer problems. However, its application in the field of fluid dynamics is still under development and is limited, because the method has encountered some difficulties arisen from the nature of the governing Navier-Stokes differential equations (Zienkiewicz and Taylor, 2000). This is mainly due to the fact that the derivative terms of the velocity components in the momentum equations are one order higher than those of the pressure. The order of the finite element interpolation functions for the velocity components is thus required to be one order higher than that of the pressure to assure the solution's stability (Patankar, 1980; Chen

and Han, 2000; Schafer and Teschauer, 2001). In addition, the non-linearity nature of the Navier-Stokes equations also poses difficulty in the analysis. An iterative computational procedure is needed to obtain the flow solution. Solving such the fluid problems thus normally requires larger computer memory and computational time as compared to those for the solid mechanics and heat transfer problems.

In the past, the six-node triangular elements were generally employed for the low- speed viscous flow analysis in arbitrary two-dimensional geometry. The mixed element interpolation functions were selected such that the interpolation functions for the velocity components are one order higher than those for the pressure (Yamada et al., 1975; Kawahara et al., 1976). The use of the sixnode elements requires extra effort for generating the finite element meshes and their related element data as compared to the regular three-node elements (Dechaumphai and Sikkhabandit, 2000). Furthermore, additional difficulty arises if both the fluid and the solid regions are to be solved together simultaneously as in the interdisciplinary problem (Wansophark et al., 2005). The finite

^{*} Corresponding Author, E-mail: fmepdc@eng.chula.ac.th TEL: +66-2-218-6621; FAX: +66-2-218-6621 Mechanical Engineering Department, Chulalongkorn University, Bangkok 10330, Thailand. (Manuscript Received May 12, 2005; Revised July 2, 2006)

Fig. 1 Modeling incompatibility from using the six-node triangular elements in the fluid region for interdisciplinary fluid/solid problem

element modeling incompatibility occurs because the three-node triangular elements are normally used in the solid region, while the six-node elements are required in the fluid region for the fluid analysis as highlighted in Fig. 1(a). Development of an alternative finite element method for the flow analysis using the three-node triangular elements, as shown in Fig. 1(b) for fluid/ solid modeling compatibility, is thus needed. Therefore, in this paper, the finite element method for the analysis of viscous incompressible flow using the regular three-node elements with nodeless variables is developed. The performance of the new finite element and the proposed method is evaluated by the analyzing several the viscous incompressible flow problems.

In addition, an adaptive meshing technique (Limtrakarn and Dechaumphai, 2004) is also implemented. The technique generates small clustered elements in the regions of high changes in solution gradients to improve solution accuracy. Larger elements are generated in the other regions where the solutions are fairly uniform to reduce the number of unknowns and thus the analysis computational time. The efficiency of the combined adaptive meshing technique and the nodeless variables finite element method is demonstrated by the problem of the flow past two fences in a channel.

2. Governing Equations

The governing differential equations for the viscous incompressible flow problems consist of the Navier-Stokes equations and the continuity equation. The two-dimensional steady-state NavierStokes equations, which represent the conservation of momentums in the x and y-directions, can be written as,

$$\rho \left(u \left(\frac{\partial u}{\partial x} + v \frac{\partial u}{\partial y} \right) - \frac{\partial \sigma_x}{\partial x} - \frac{\partial \tau_{yx}}{\partial y} = 0 \right)$$
 (1a)

$$\rho \left(u \left(\frac{\partial v}{\partial x} + v \frac{\partial v}{\partial y} \right) - \frac{\partial \tau_{xy}}{\partial x} - \frac{\partial \sigma_y}{\partial y} = 0 \right)$$
 (1b)

where ρ is the density: u and v are velocity components in the x and y-directions, respectively. For the Newtonian fluid, the normal and tangential stress components in Eqs. (1a) and (1b) above are written in terms of the pressure, ρ , and the velocity gradients as,

$$\sigma_x = -p + 2\mu \frac{\partial u}{\partial x} \tag{2a}$$

$$\sigma_y = -p + 2\mu \frac{\partial v}{\partial y} \tag{2b}$$

$$\tau_{xx} = \tau_{yx} = u \left(\frac{\partial u}{\partial y} + \frac{\partial v}{\partial x} \right) \tag{20}$$

where μ is the viscosity. The Navier-Stokes equations can then be rewritten in the form of non-linear partial differential equations of second order as,

$$\rho\left(u\frac{\partial u}{\partial x} + v\frac{\partial u}{\partial y}\right) - \mu\left(\frac{\partial^2 u}{\partial x^2} + \frac{\partial^2 u}{\partial y^2}\right) + \frac{\partial \rho}{\partial x} = 0$$
(3a)

$$\rho\left(u\frac{\partial v}{\partial x} + v\frac{\partial v}{\partial y}\right) - \mu\left(\frac{\partial^2 v}{\partial x^2} + \frac{\partial^2 v}{\partial y^2}\right) + \frac{\partial p}{\partial y} = 0 \quad (3b)$$

The above two equations, together with the continuity equation representing the conservation of mass.

$$\frac{\partial u}{\partial x} + \frac{\partial v}{\partial y} = 0 \tag{3c}$$

are to be solved for the unknowns of the velocity components and the pressure.

These differential equations, Eqs. (3a) \sim (3c), are to be solved with appropriate boundary conditions which are either specifying velocity components along edge S_3 ,

$$u(x,y) = u_1(x,y) \tag{4a}$$

$$v(x, y) = v_1(x, y)$$
 (4b)

or surface tractions along edge S2,

$$T_x = \sigma_x l + \tau_{xy} m \tag{5a}$$

$$T_{v} = \tau_{xy}l + \sigma_{y}m \tag{5b}$$

where l and m are the direction cosines of the unit vector normal to the boundary edge.

3. Finite Element Formulations

The Galerkin finite element method is applied for deriving the finite element equations from the governing differential equations, Eqs. (3a) ~ (3c). The computational domain is discretized using the regular three-node finite elements. These three-node finite element velocity component and the pressure distributions in the form,

$$p(x, y) = H_i(x, y) p_i \tag{6a}$$

$$u(x, y) = H_i(x, y) u'_i + G_i(x, y) u''_i$$
 (6b)

$$v(x, y) = H_t(x, y) v'_i + G_t(x, y) v''_i$$
 (6c)

where u_i' and v_i' , i=1,2,3, are the velocity components at the three nodes, and p_i is the nodal pressure. The u_i'' and v_i'' , j=1,2,3, are nodeless variables related to velocity components that do not need their locations as required by the actual nodes. The element interpolation functions, H_i , are linear in the form,

$$H_1 = L_1 \tag{7a}$$

$$H_2 = I_{-2} \tag{7b}$$

$$H_3 = L_3 \tag{7c}$$

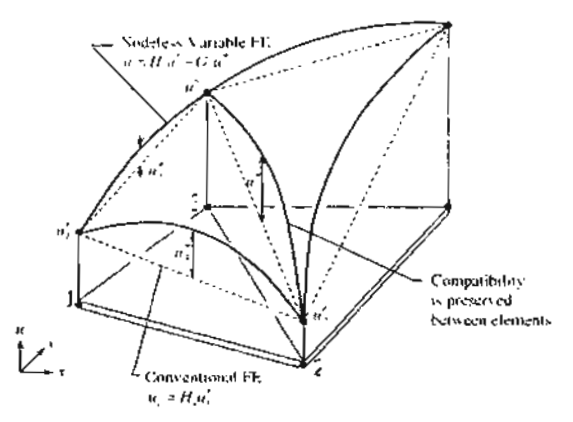


Fig. 2 Meaning and distribution of the nodeless variable finite elements with the preserved compatibility condition along element inter-

and the nodeless variable interpolation functions, G_i , are quadratic in the form,

$$G_1 = 4L_2L_3 \tag{8a}$$

$$G_2 = 4L_1L_3$$
 (8b)

$$G_3 = 4L_1L_2 \tag{8c}$$

where L_i are the area coordinates (Zienkiewicz and Taylor, 2000). Distributions of these functions together with the nodeless variables as compared to those for the conventional 3-node element are shown in Fig. 2. The figure also shows that the compatibility condition is always preserved along the element interfaces to ensure the solution convergence. For simplicity in the derivation of the finite element equations presented later, the element velocity component distributions in Eqs. (6b) and (6c) are first written in the form,

$$u(x,y) = N_i(x,y) u_i \tag{9a}$$

$$v(x,y) = N_i(x,y) v_i \tag{9b}$$

where i=1 to 6. The Bubnov-Galerkin finite element method is applied to the differential Eqs. $(3a) \sim (3c)$ for deriving the finite element equations by using the element interpolation functions above. The finite element equations in form of integrals over the element domain A and the

element edge S2 are.

$$\int_{A} N_{i}u u_{x}dA + \int_{A} N_{i}v u_{x}dA - \frac{1}{\rho} \int_{A} N_{i,x}\rho dA$$

$$+ \frac{2\mu}{\rho} \int_{A} N_{i,x}u_{,x}dA + \frac{\mu}{\rho} \int_{A} N_{i,y}u_{,y}dA \qquad (10a)$$

$$+ \frac{\mu}{\rho} \int_{A} N_{i,y}v_{,x}dA = \int_{S_{t}} N_{i}T_{x}dS$$

$$\int_{A} N_{i}u \, v_{,x} dA + \int_{A} N_{i}v \, v_{,y} dA - \frac{1}{\rho} \int_{A} N_{i,y} \rho dA$$

$$+ \frac{\mu}{\rho} \int_{A} N_{i,x} u_{,y} dA + \frac{\mu}{\rho} \int_{A} N_{i,x} v_{,x} dA \qquad (10b)$$

$$+ \frac{2}{\rho} \int_{A} N_{i,y} v_{,y} dA = \int_{S_{2}} N_{i} T_{x} dS$$

$$\int_{A} H_{i}(u_{,x}+v_{,y}) dA = 0 \qquad (10c)$$

Then, by the substitution of Eqs. (9a) and (9b) into equations (10a) and (10b), the finite element equations can be written in form of the tensor notations as,

$$K_{\alpha\beta\gamma} \times u_{\beta} u_{\gamma} + K_{\alpha\beta\gamma} \times v_{\beta} u_{\gamma} - H_{\alpha\mu} \times p_{\mu} + S_{\alpha\beta} \times \times u_{\beta} + S_{\alpha\beta} \times \times v_{\beta} = Q_{\alpha} \times$$
(11a)

$$K_{\alpha\beta\gamma} \times u_{\beta}u_{\gamma} + K_{\alpha\beta\gamma} v_{\beta}v_{\gamma} - H_{\alpha\mu}v_{\beta\mu} + S_{\alpha\beta} \times u_{\beta} + S_{\alpha\beta} v_{\gamma}v_{\beta} = Q_{\alpha}v$$
(11b)

$$H_{s\mu\nu}u_s + H_{s\mu\nu}v_s = 0 \tag{11c}$$

where the coefficients in these equations are defined by,

$$K_{\alpha\beta\gamma^{x}} = \int_{A} N_{\alpha} N_{\beta} N_{\gamma,x} dA \qquad (12a)$$

$$K_{\alpha\beta\gamma\gamma} = \int_{a} N_{\alpha} N_{\beta} N_{\gamma,\gamma} dA$$
 (12b)

$$H_{\alpha\lambda^x} = \frac{1}{\rho} \int_A N_{\alpha,x} H_{\lambda} dA \qquad (12c)$$

$$H_{\alpha\lambda} = \frac{1}{\rho} \int_{A} N_{\alpha,y} H_{\lambda} dA \qquad (12d)$$

$$S_{\alpha\beta xx} = \frac{2\mu}{\rho} \int_{A} N_{\alpha,x} N_{\beta,x} dA + \frac{\mu}{\rho} \int_{A} N_{\alpha,y} N_{\beta,y} dA \quad (12e)$$

$$S_{\alpha\beta^{xy}} = \frac{\mu}{\rho} \int_{A} N_{\alpha,y} N_{\beta,x} dA \qquad (12f)$$

$$S_{\alpha,j,rs} = \frac{\mu}{\rho} \int_{A} N_{\sigma,x} N_{\beta,y} dA \qquad (12g)$$

$$S_{\alpha\beta\gamma\gamma} = \frac{\mu}{\rho} \int_{4} N_{\alpha,x} N_{\beta,x} dA + \frac{2\mu}{\rho} \int_{A} N_{\alpha,y} N_{\lambda,y} dA \quad (12h)$$

$$Q_{\alpha x} = \int_{S^2} N_i T_x dS \qquad (12i)$$

$$Q_{ay} = \int_{S^2} N_i T_y dS \tag{12j}$$

4. Computational Procedure

The finite element equations, as shown in Eqs. (11a) ~ (11c) are non-linear to be solved by an iterative method. The Newton-Raphson iterative method is selected in this study. The method requires writing the unbalance values in the form,

$$F_{\alpha x} = K_{\alpha \beta \gamma} \times u_{\beta} u_{\gamma} + K_{\alpha \beta \gamma} \times u_{\beta} u_{\gamma}$$

$$-\frac{1}{\rho} H_{\alpha \lambda} \times p_{\lambda} + S_{\alpha \beta} \times u_{\beta} + S_{\alpha \beta} \times v_{\beta} - Q_{\alpha x}$$
(13a)

$$F_{\alpha \nu} = K_{\alpha \beta \gamma \nu} u_{\beta} v_{\gamma} + K_{\alpha \beta \gamma \nu} v_{\beta} v_{\gamma}$$

$$- \frac{1}{\rho} H_{\alpha \lambda \nu} p_{\lambda} + S_{\alpha \beta \nu \nu} u_{\beta} + S_{\alpha \beta \nu \nu} v_{\beta} - Q_{\alpha \nu}^{(136)}$$

$$F_{\mu} = H_{\theta\mu} \times u_{\theta} + H_{\theta\mu} \times v_{\theta} \tag{13c}$$

Then application of the method leads to a set of algebraic equations with incremental unknowns in the form,

$$\begin{bmatrix} G_{\alpha\beta^{\chi}} & L_{\alpha\beta^{\chi}} & -H_{\alpha\lambda^{\chi}} \\ L_{\alpha\beta^{\chi}} & G_{\alpha\beta^{\chi}} & -H_{\alpha\lambda^{\chi}} \\ H_{\beta\mu^{\chi}} & H_{\beta\mu^{\chi}} & 0 \end{bmatrix} \begin{pmatrix} \Delta u_{\beta} \\ \Delta v_{\beta} \\ \Delta p_{\beta} \end{pmatrix} = \begin{pmatrix} F_{\alpha^{\chi}} \\ F_{\alpha^{\chi}} \\ F_{\mu} \end{pmatrix}$$
(14)

where the coefficients in the above equations, are,

$$G_{\alpha\beta x} = K_{\alpha\beta\gamma x} u_{\gamma} + K_{\alpha\gamma\beta x} u_{\gamma} + K_{\alpha\gamma\beta x} v_{\gamma} + S_{\alpha\beta xx}$$
(152)

$$G_{\alpha\beta\gamma} = K_{\alpha\beta\gamma\gamma}v_{\gamma} + K_{\alpha\gamma\beta\gamma}v_{\gamma} + K_{\alpha\gamma\beta\gamma}u_{\gamma} + S_{\alpha\beta\gamma\gamma}$$
(156)

$$L_{\alpha\beta^{\chi}} = K_{\alpha\beta\gamma^{\chi}} v_{\gamma} + S_{\alpha\beta^{\gamma\chi}} \tag{15c}$$

$$L_{\alpha\beta\gamma} = K_{\alpha\beta\gamma\gamma} u_{\tau} + S_{\alpha\beta\gamma\gamma} \tag{15d}$$

These coefficients which are in form of element matrices can be evaluated in closed-form ready for computer programming. Details of the derivation for these element matrices are omitted herein for brevity. In these Eqs. $(15a) \sim (15d)$, u_7 and v_7

are the values of the velocity components for both the actual nodes and the nodeless variables at the $i^{\rm th}$ iteration. The iteration process is terminated if the change in percentage of the overall errors of the nodal unknowns from the previous iteration is less than the specified value.

5. Adaptive Meshing Technique

The idea behind the adaptive meshing technique (Limtrakarn and Dechaumphai, 2004) presented herein is to construct a new mesh based on the solution obtained from the previous mesh. The new mesh will consist of small elements in the regions with large change in solution gradients and large elements in the other regions where the change in solution gradients is small. To determine proper element sizes at different locations in the flow field, the solid-mechanics concept for determining the principal stresses from a given state of stresses at a point is employed. Since small elements are needed in the regions of complex flow behavior, thus the velocity distribution can be used as an indicator in the determination of proper element sizes.

To determine proper element sizes, the second derivatives of the flow velocity with respect to the global coordinates x and y are first computed,

$$\begin{bmatrix}
\frac{\partial^2 V}{\partial x^2} & \frac{\partial^2 V}{\partial x \partial y} \\
\frac{\partial^2 V}{\partial x \partial y} & \frac{\partial^2 V}{\partial y^2}
\end{bmatrix}$$
(16)

where V is the magnitude of the two velocity components u and v,

$$V = \sqrt{u^2 + v^2} \tag{17}$$

The principal quantities in the principal directions X and Y where the cross derivatives vanish, are then determined,

$$\begin{bmatrix} \frac{\partial^2 V}{\partial X^2} & 0\\ 0 & \frac{\partial^2 V}{\partial Y^2} \end{bmatrix}$$
 (18)

The magnitude of the larger principal quantity is

then selected,

$$\lambda = \max\left(\left|\frac{\partial^2 V}{\partial X^2}\right|, \left|\frac{\partial^2 V}{\partial Y^2}\right|\right) \tag{19}$$

This value is used to compute proper element size h at that location from the conditions.

$$h^2 \lambda = \text{constant} = h_{\text{min}}^2 \lambda_{\text{max}}$$
 (20)

where h_{\min} is the specified minimum element size, and λ_{\max} is the maximum principal quantity for the entire model.

6. Examples

In this section, three examples are presented. The first two examples are used to verify and evaluate the nodeless variables finite element method with exact solution and solution from other numerical method. The third example is used to demonstrate the capability of the combined nodeless variable finite element method and the adaptive meshing technique to improve the analysis solution accuracy.

6.1 Lubricant flow in journal bearing

The problem statement of the lubricant flow in journal bearing is shown in Fig. 3. The problem can be simplified as illustrated in the Fig. 4 if the length L is much larger than the gap h. The figure shows the lower sliding pad moving at a velocity U relative to the stationary pad inclined

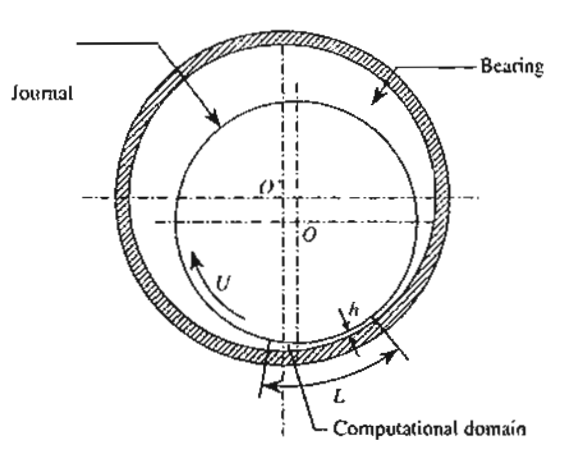


Fig. 3 Problem statement of lubricant flow in journal bearing

at a small angle with respect to the sliding pad. The small gap between the two pads is filled with a lubricant. The exact solution of the velocity is (Reddy and Gartling, 1994),

$$u = \frac{1}{2\mu} \frac{\partial h}{\partial x} y(y - h) + U\left(1 - \frac{y}{h}\right)$$
 (21)

where

$$h = h_0 + (h_L - h_0) \frac{x}{I}$$
 (22)

and the exact solution for the pressure distribution is.

$$\frac{P}{\mu U L/h_0^2} = \frac{6(x/L) \left(1 - x/L\right) \left(1 - h_L/h_0\right)}{\left(1 + h_L/h_0\right) \left[1 - \left(1 - h_L/h_0\right) x/L\right]^2}$$
(23)

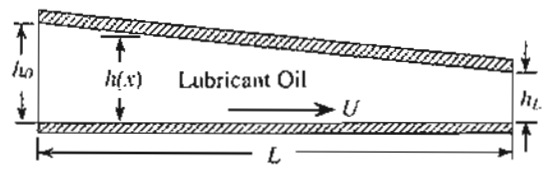


Fig. 4 Computational domain for lubricant flow in journal bearing

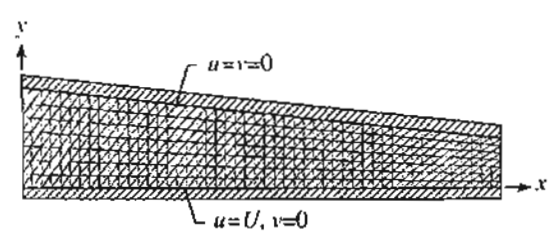


Fig. 5 Finite element model and boundary conditions of lubricant flow in journal bearing

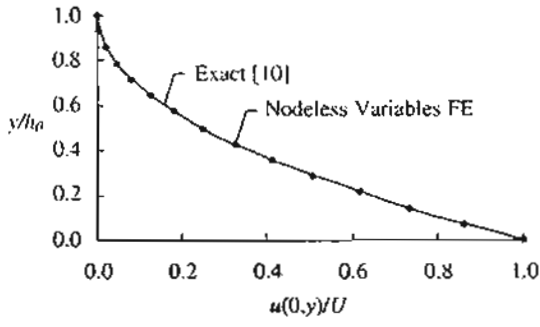


Fig. 6 Comparison of velocity profiles along the left boundary

In the computation, the values of $h_L=2$, $h_0=1$, L=20, U=5, and $\mu=10$ are selected. The finite element model as shown in Fig. 5 consists of 686 nodeless variables finite elements. Figures 6 and 7 show good agreement between the predicted and the exact solutions for the velocity profiles at the entrance and the exit of the computational domain. Figure 8 also shows good comparison of the predicted and the exact pressure distributions along the lower boundary of the computational model.

6.2 Lid-driven cavity flow

The problem of the flow circulation in a closed cavity driven by a moving lid has been widely used to validate new fluid computational methods. The problem statement is illustrated in Fig. 9. The flow circulation in a unit square cavity is induced by a moving lid at the velocity of U=1 to the right. A finite element model, with a 50×50 mesh discretization along the x and y directions, consisting of all the nodeless variable finite

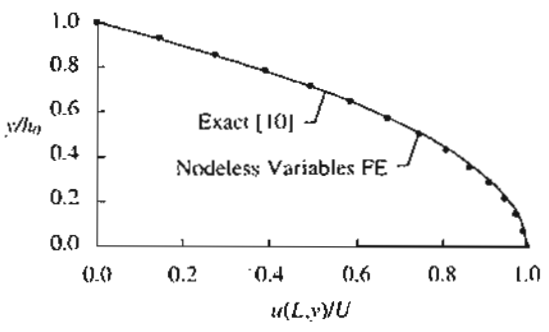


Fig. 7 Comparison of velocity profiles along the right boundary

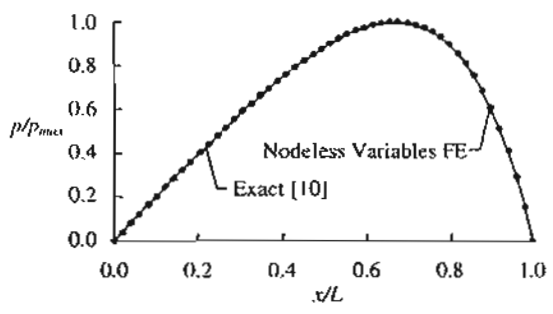


Fig. 8 Comparison of pressure distributions along the bottom boundary

elements is shown in Fig. 10. The predicted velocity vectors of the flow circulation behavior at

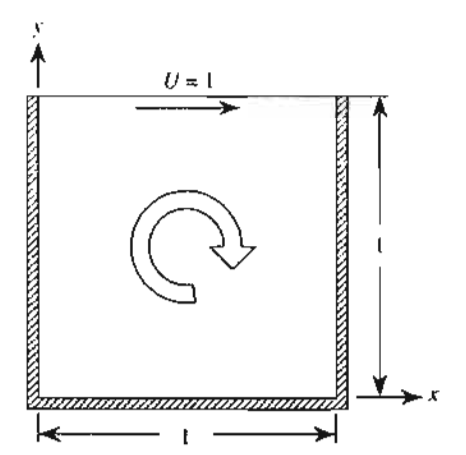


Fig. 9 Problem statement of lid-driven cavity flow

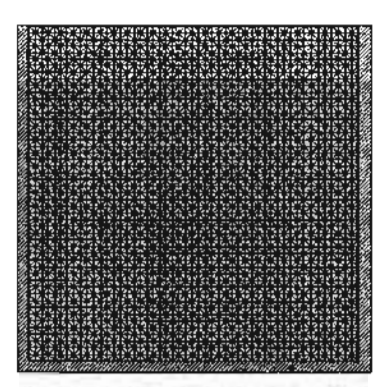


Fig. 10 Finite element model of lid-driven cavity flow problem

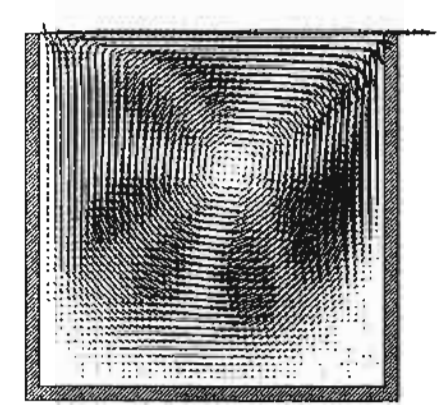


Fig. 11 Predicted velocity vectors of lid-driven cavity flow problem

the Reynolds number of 400 are plotted in Fig. 11. Figure 12 shows good agreement of the velocity profiles along the cavity centered lines obtained from the nodeless variables finite element method and those presented Ref. (Ramaswamy and Juc. 1991).

6.3 Flow past two fences in channel

The problem of a flow past two fences in a channel is used to evaluate the performance of the combined nodeless variables finite element method and the adaptive meshing technique. The problem statement of the flow past the two fences in the channel with its geometry are shown in Fig. 13. Results of the flow behavior for this problem, including the separations behind the obstacles, were obtained by experiment and presented in Ref. (Durst et al., 1988).

The procedure of the combined nodeless variables finite element method and the adaptive meshing technique starts from generating a crude uniform mesh throughout the model as shown in Figs. $(4(a) \sim (c))$. The nodeless variables finite element method is then employed to predict the flow solution according to this first uniform mesh. The flow solution shown in Figs. $14(d) \sim (f)$ is then used, based on the adaptive meshing technique described in Section 5, to construct a new mesh. This second mesh as shown in Figs. 15(a) ~ (c) consists of clustered small elements in the regions of high changes in the solution gradients. Larger elements are, at the same time, generated in the other regions where the flow solution is fairly uniform. The nodeless variables finite ele-

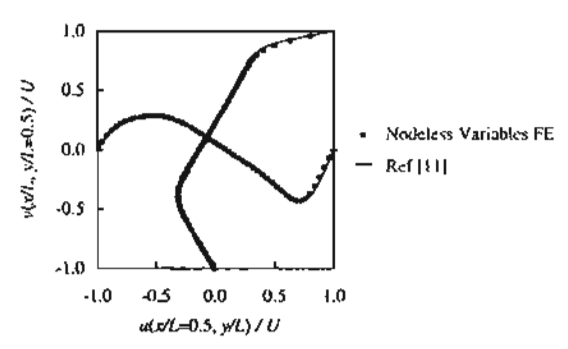


Fig. 12 Comparison of velocities of lid-driven cavity flow problem

ment method is then performed using this second mesh to produce a new flow solution as shown in Figs. $15(d) \sim (f)$. This procedure of generating new mesh and performing finite element computation is repeated. Figure 16(a) shows the third adaptive mesh. Small elements are clustered in the upper left corner of both the left and the right

fences, as shown in Figs. 16(b) (c), where the fluid pressures change abruptly. The figure also shows that larger elements are generated in the other regions to reduce the computational time and the computer memory requirement.

Small elements generated at the upper left corners of both the fences provide high solution ac-

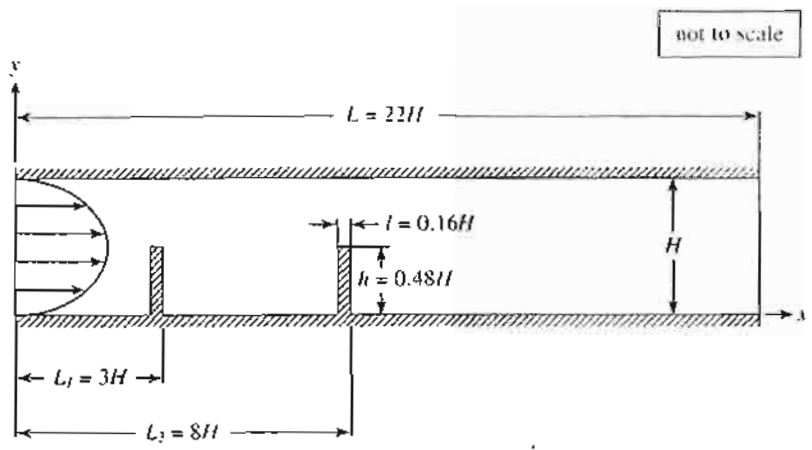


Fig. 13 Problem statement for flow past two fences in channel

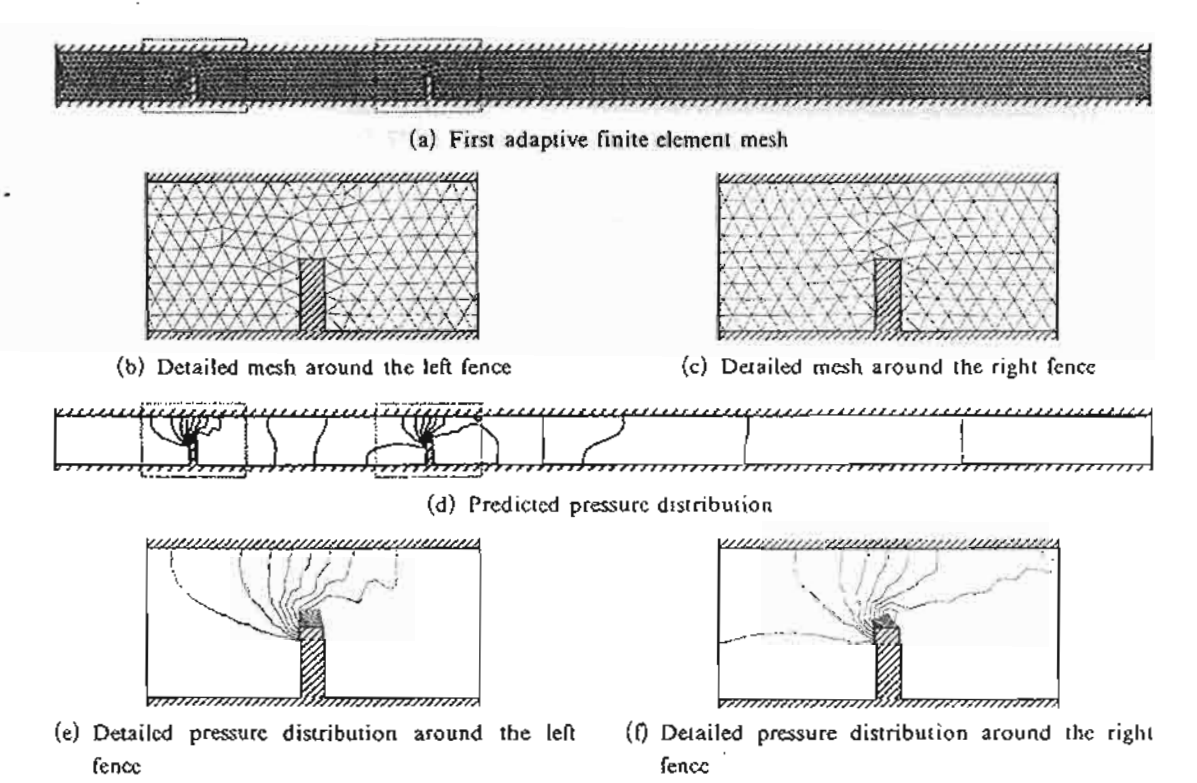


Fig. 14 First adaptive mesh and its solution for flow past two fences in channel problem

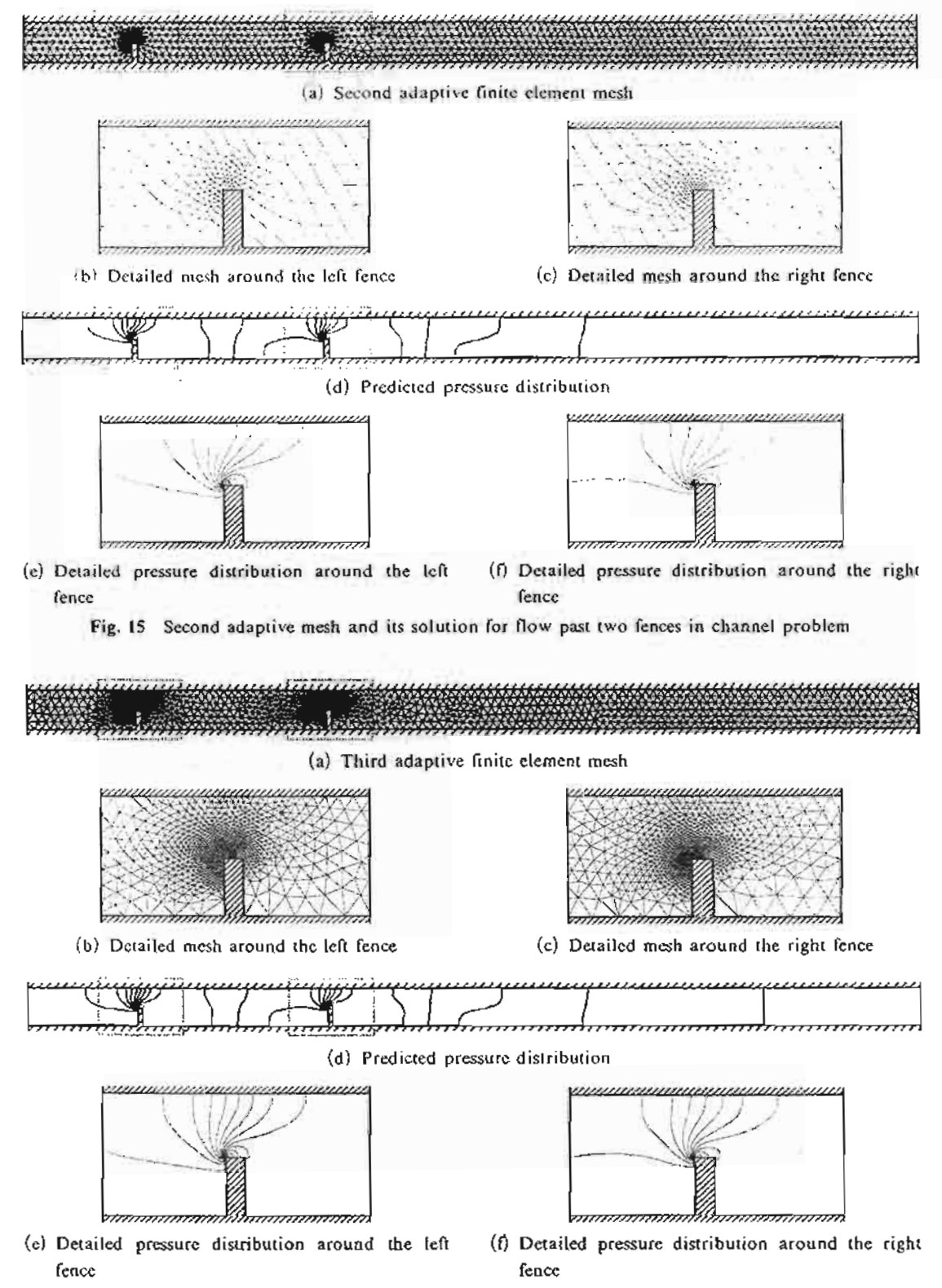


Fig. 16 Third adaptive mesh and its solution for flow past two fences in channel problem

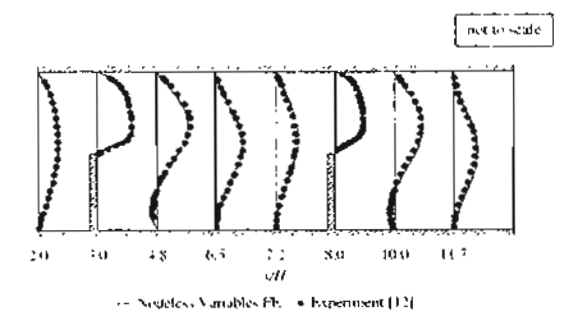


Fig. 17 Comparative velocity profiles for flow past

curacy as can be observed by the smooth pressure contours in Figs. $16(d) \sim (f)$. The predicted velocity profiles are compared with the experimental data (Durst et al., 1988) in Fig. 17. The figure shows good comparisons at different channel locations, with flow separations captured near the lower surface at x/H equals to 4.8 and 10.

7. Conclusions

The nodeless variables finite element method for viscous incompressible flow analysis was presented. The nodeless variables were incorporated into the standard three-node triangular elements to increase the order of the velocity interpolation functions. The nodeless variables finite elements avoid the need for using the six-node triangular elements normally employed to provide the analysis solution stability. The use of the nodeless variables finite elements reduces the difficulty for generating the meshes and provides modeling compatibility for the interdisciplinary analysis of coupled fluid/solid problems.

The nodeless variables finite element equations were derived from the governing Navier-Stokes differential equations. All finite element matrices were derived in closed-form and a corresponding computer program was developed. Two examples with exact and numerical solutions were used to validate the performance of the nodeless variables finite element method. The method was also combined with an adaptive meshing technique to further increase the overall analysis performance. The adaptive meshing technique generates small clustered elements in the regions of high solu-

tion gradients to increase the solution accuracy. Larger elements are generated in the other regions to reduce the computational time as well as the computer memory. The efficiency of the combined adaptive meshing technique and the nodeless variables finite element method was demonstrated by using the example of a flow past two fences in a channel

Acknowledgements

The authors are pleased to acknowledge the Thailand Research Fund (TRF) for supporting this research work.

References

Chen, X. and Han, P., 2000, "A Note on the Solution of Conjugate Heat Transfer Problems Using SIMPLE-Like Algorithm," *International Journal of Heat and Fluid Flow*, Vol. 21, pp. 463~467.

Dechaumphai, P. and Sikkhabandit, S., 2000, "Adaptive Finite Element Technique for Viscous Flow Analysis," ASEAN Journal on Science and Technology for Development, Vol. 17, No. 1, pp. 41~58.

Durst, F., Founti, M. and Obi, S., 1988, "Experimental and Computational Investigation of the Two-Dimensional Channel Flow over Two Fences in Tandem," *Trans. ASME, Journal of Fluids Engineering*, Vol. 110, pp. 48~54.

Kawahara, M., Yoshimura, N., Nakagawa, K. and Ohsaka, H., 1976, "Steady and Unsteady Finite Element Analysis of Incompressible Viscous Fluid," *International Journal of Numerical Methods in Engineering*, Vol. 10, pp. 437—456.

Limtrakarn, W. and Dechaumphai, P., 2004, "Interaction of High-Speed Compressible Viscous Flow and Structure by Adaptive Finite Element Method," KSME International Journal, Vol. 18, No. 10, pp. 1837—1848.

Patankar, S. V., 1980, Numerical Heat Transfer and Fluid Flow, McGraw-Hill, New York.

Ramaswamy, B. and Jue, T. C., 1991, "A Segregated Finite Element Formulation of Navier-Stokes Equations Under Laminar Conditions,"

Finite Element in Analysis and Design, Vol. 9, pp. 257 - 270.

Reddy, J. N. and Gartling, D. K., 1994. The Finite Element Method in Heat Transfer and Fluid Dynamics, CRC Press, Florida.

Schafer, M. and Teschauer, I., 2001, "Numerical Simulation of Coupled Fluid-Solid Problems," Computer Methods in Applied Mechanics and Engineering, Vol. 190, pp. 3645~3667.

Wansophark, N., Malatip, A. and Dechaumphai, P., 2005, "Streamline Upwind Finite Element Method for Conjugate Heat Transfer Problems,"

To be Published in the Journal of Acta Mechanica Sinica

Yamada, Y., Ito, K., Yokouchi, Y., Tamano, T. and Ohtsubo, T., 1975, "Finite Element Analysis of Steady Fluid and Metal Flow," Finite Element Methods in Fluids, Edited by Gallagher, R. H., Zienkiewicz, O. C., Oden, J. T. and Taylor, C., Wiley, New York.

Zienkiewicz, O. C. and Taylor, R. L., 2000, The Finite Element Method, 5th Ed., Vol. 3, Fluid Dynamics, Butterworth-Heinemann, Oxford.

บทความทางวิชาการ เรื่อง

Two-Dimensional Adaptive Mesh

Generation Algorithm and Its Application
with Higher-Order Compressible

Flow Solver

Published in the

Journal of Mechanical Science and Technology

Vol. 18, No. 12, pp. 2190-2203 2004

Two-Dimensional Adaptive Mesh Generation Algorithm and its Application with Higher-Order Compressible Flow Solver

Sutthisak Phongthanapanich, Pramote Dechaumphai*

Mechanical Engineering Department, Chulalongkorn University,

Bangkok 10330, Thailand

The Separate Volume of KSME International Journal

Two-Dimensional Adaptive Mesh Generation Algorithm and its Application with Higher-Order Compressible Flow Solver

Sutthisak Phongthanapanich, Pramote Dechaumphai'

Mechanical Engineering Department, Chulalongkorn University, Bangkok 10330, Thailand

A combined procedure for two-dimensional Delaunay mesh generation algorithm and an adaptive remeshing technique with higher-order compressible flow solver is presented. A pseudo-code procedure is described for the adaptive remeshing technique. The flux-difference splitting scheme with a modified multidimensional dissipation for high-speed compressible flow analysis on unstructured meshes is proposed. The scheme eliminates nonphysical flow solutions such as the spurious bump of the carbuncle phenomenon observed from the bow shock of the flow over a blunt body and the oscillation in the odd-even grid perturbation in a straight duct for the Quirk's odd-even decoupling test. The proposed scheme is further extended to achieve higher-order spatial and temporal solution accuracy. The performance of the combined procedure is evaluated on unstructured triangular meshes by solving several steady-state and transient high-speed compressible flow problems.

Key Words: Adaptive Mesh. Delaunay Triangulation, Carbuncle Phenomenon, H-correction Entropy Fix

1. Introduction

Spatial discretization of a given domain is a prerequisite for solutions with finite-element or finite-volume method of a partial differential equations system that represents the physical model of the problem. Generally, triangulation process starts from the generation of the point list; the points are subsequently connected into triangular elements. The points connection step is often performed by constructing the Delaunay triangulation (Bowyer, 1981; Watson, 1981) of the point set to guarantee triangles which are as well-shaped as possible for the given points. Since the Delaunay triangulation in itself does not include procedures for creating points in-

To enhance the solution accuracy of the numerical analysis and to improve the computed solution, mesh adaptation is needed. An adaptive remeshing technique is incorporated with an appropriated error indicator to dictate a close correlation between the size of elements and the behavior of the corresponding computed solution. The technique is implemented to capture the fast variation of the solution with a reasonable number of elements. The process of the adaptive meshing is to first generate an initial mesh for the domain. The mesh is used to compute the corresponding solution by the finiteelement or finite-volume method. Then the regions where adaptation is vital are determined by an error indicator, and new adapted mesh for the solution is entirely generated. The same process is repeated until the specified convergence criterion is met. The efficiency of the overall

side the domain, points are generated independently by an automatic point creation algorithm (Marchant and Weatherill, 1993; Karamete et al., 1997)

^{*} Corresponding Author, E-mail: fmepdc@eng.chula.ac.th Mechanical Engineering Department, Chulalongkorn University, Bangkok 10330, Thailand. (Manuscript Received May 25, 2004; Revised September 23, 2004)

procedure is evaluated by calculating flows that include the supersonic shock waves and shock propagation behaviors.

High-speed compressible flows normally involve complex flow phenomena, such as strong shock waves and shock-shock interactions. Various numerical inviscid flux formulations have been proposed to solve an approximate Riemann problem (Roe, 1981; Steger and Warming, 1981; Liou et al., 1993; Toro et al., 1994; Kang et al., 2002; Kang et al., 2003). Among these formulations, the flux-difference splitting scheme by Roe (1981) is widely used due to its accuracy, quality and mathematical clarity. However, the scheme may sometimes lead to nonphysical flow solutions in certain problems, such as the carbuncle phenomenon (Perry and Imlay, 1988) with a spurious bump in the bow shock for flow over a blunt body. In the odd-even decoupling problem (Quirk, 1994), an unrealistic perturbation may grow with the planar shock as it moves along the duct. To improve the solution accuracy of these problems. Quirk pointed out that the original Roe's scheme should be modified or replaced by other schemes in the vicinity of strong shock. It has been known that the original Roe's scheme does not satisfy the entropy condition and may allow unrealistic expansion shock. Harten (1983) proposed an entropy fix formulation to replace the near zero small eigenvalues by some tolerances. The mathematical background of the Harten's entropy fix with the suggested tolerance values is given by Van Leer et al. (1989).

This paper proposed a mixed entropy fix method for the Roe's scheme on adaptive unstructured meshes for two-dimensional high-speed compressible flow analysis. The entropy fix method by Van Leer et al. and the multidimensional dissipation technique of Pandolfi and D'Ambrosio (2001) are modified for unstructured triangular meshes and implemented into the original Roe's scheme. The presented scheme is further extended to higher-order solution accuracy and then evaluated by several benchmark test cases.

The presentation in this paper starts at Section 2 describing an adaptive remeshing technique

with the implementation procedure in an objected-oriented programming concept. Section 3 describes the Roe's flux-difference splitting scheme with some well-known problems that exhibit numerical shock instability. A Roe's scheme with a mixed entropy fix method is then proposed and examined for their capabilities. The presented scheme is further extended to higher-order solution accuracy and then evaluated by several benchmark test cases in Section 4. Finally, the performance of the scheme is evaluated on adaptive unstructured meshes for solving both the steady-state and transient high-speed compressible flow problems.

2. Delaunay Triangulation and Adaptation Technique

2.1 Mesh generation and adaptation

The mesh generation implemented in this paper follows the Delaunay triangulation (Bowyer, 1981; Watson, 1981). The algorithm itself does not provide the procedure for creating new points inside the domain. The automatic point creation procedure presented in this paper are derived from the algorithm suggested by Marchant and Weatherill (1993). The shape and size of elements or density of points inside the domain are controlled by two coefficients, the Alpha and the Beta coefficients. The main idea of the automatic point creation procedure is to search for the element that conforms to both the Alpha and Beta testing criteria and a new point placement at the centroid of that element. New elements can then be created by the Delaunay triangulation algorithm. The step-by-step explanation of these algorithms was presented in detail in Ref. (Phongthanapanich and Dechaumphai, 2004).

To capture fast variations of the solution, small elements are needed along that region in the domain. The proper element size h_i is computed by requiring that the error should be uniform for all elements (Dechaumphai and Morgan, 1992):

$$h_i^2 \lambda_i = h_{\min}^2 \lambda_{\max} = \text{constant}$$
 (1)

where λi is the higher principal quantity of the element considered,

$$\lambda_i = \max\left(\left|\frac{\partial^2 \phi}{\partial X^2}\right|, \left|\frac{\partial^2 \phi}{\partial Y^2}\right|\right) \tag{2}$$

and ϕ is the selected solution indicator. In the above Eq. (1), λ_{\max} is the maximum principal quantity for all elements and h_{\min} is the minimum element size specified by users. The regions, which will be refined or coarsened by Adaptive-Remeshing algorithm below, are identified by a dimensionless error indicator using the pressure-switch coefficient (Probert et al., 1991). The indicator at node I is given by,

$$E_{I} = \frac{\sum_{e \in I} |2\phi_{I} - \phi_{J} - \phi_{K}|}{\sum_{e \in I} (A^{*} + B^{*})}$$
(3)

where f and K are the other two nodes of the triangle, e, $A^* = \max(|\phi_I - \phi_J|, \alpha(\phi_I + \phi_I))$ and $B^* = \max(|\phi_I - \phi_K|, \alpha(\phi_I + \phi_K))$. The value of α is used to identify the solution discontinuity or numerical oscillation. According to numerical experiment especially for the proposed scheme that will be explained later, the value of α is prescribed as 0.005 in this paper. This means $A^* = 0.005(\phi_I + \phi_I)$ and $B^* = 0.005(\phi_I + \phi_K)$ if ϕ_I and ϕ_K are oscillated within 1% of ϕ_I , respectively.

Practical experience found that this type of error indicator for the transient high-speed compressible flow problems, where regions such as shock or discontinuity have different strength, may cause inaccurate solution due to the inadequate refinement because the point spacing is scaled according to the maximum value of the second derivatives. In order to overcome this problem, an element size scaling function, which scales the point spacing of point p_i within the range of χ_{man} and χ_{max} , has been used:

$$\chi_i = \text{scaleRange}\left(\frac{h_{\text{max}} - dp_i}{h_{\text{max}} - h_{\text{min}}}, 0, 1, \chi_{\text{min}}, \chi_{\text{max}}\right)$$
 (4)

The coefficient χ_i controls the point insertion in the regions of high solution gradient and eliminates excessive distortion of the regularity of the triangulation. The value of χ_{min} limits the number of points insertion in the high gradient region such as shock, while the value of upper limit χ_{max} allows to insert more points into the

region with smaller solution gradient such as the tail of the expansion fan. When the adapted elements generated by this function are distorted in shape, the Alpha and Beta coefficients are incorporated to control the point density and the regularity of triangulation.

The proposed adaptive mesh regeneration is based on the concepts of the Delaunay triangulation and the mesh refinement. The new mesh is constructed using the information from the previous or background mesh, and it is composed of small elements in the regions with large changes of the solution gradients, and large elements in the remaining regions where the changes of the solution gradients are small. Detailed process of adaptive remeshing technique is described as follows.

Algorithm AdaptiveRemeshing (P. T. P0, alpha, beta, houn, hour, Xionn, Xionn, threshold)

- 1. Let P0, $k=1, \dots, n$ be the set of points of the background mesh.
- 2. Let P be the set of points and T be the set of triangles.
- 3. Read next interior point p_i of the background mesh from P0.
 - 4. If $h_i > h_{\text{max}}$ then go to step 3.
- 5. Search triangle t_i in T which contains the point p_i . Then calculate the centroid of the triangle t_i and define it as point p_q , and compute the point distribution function of point p_q by Eq. (5).

$$dp_{q} = \frac{1}{M} \sum_{i=1}^{M} |p_{i} - p_{q}|$$
 (5)

where M is number of surrounding nodes to node q.

- 6. Compute the distance d_m , m=1, 2, 3 from point pq to each of the three vertices of the triangle t_i .
- 7. Compute the Xi coefficient, χ_i , for point p_i by using Eq. (4), and the average distance, $s_i = (d_1 + d_2 + d_3)/3$.
- 8. Perform the Xi-Alpha test for point p_q . If $(\chi_i \cdot alpha \cdot h_i) >= s_i$, then reject the point p_q and return to step 3.
- 9. Perform the Xi-Beta test for point p_q . If two out of three of $d_m < (\chi_i \cdot h_{min}/beta)$ for any

- m=1, 2, 3, then reject the point p_q and return to step 3.
- 10. Accept the point pq for insertion by the Delaunay triangulation algorithm and add point p_q into P.
- 11. Repeat steps 3 to 10 until all points in P are considered.
- 12. Perform the Delaunay triangulation of the inserted points in P.
- 13. If number of accepted points greater than threshold, then go to step 3; otherwise stop the algorithm.

Since the proposed algorithm above does not guarantee the good mesh topology, the mesh relaxation (Frey, 1991) based on an edge-swapping technique is highly recommended for wellshaped mesh improvement. The objective of this method is to make the topology of elements closer to equilateral triangles by swapping edges to equalize the vertex degrees (number of edges linked to each point) toward the value of six. Finally, the Laplacian smoothing is applied to smooth the meshes.

2.2 Mesh generation implementation and algorithm evaluation

This section presents the main algorithm for combining together the mesh generation from the Delaunay triangulation, the mesh refinement procedure, and the adaptive remeshing technique. This main algorithm is demonstrated using the object-oriented programming concept that takes into account the advantages of the code encapsulation, inheritance, and polymorphism capabilities. The implementation of the main algorithm is summarized in the algorithm below.

Algorithm Main

```
(P, T, alpha, beta, iteration, Hmin, Hmax,
Xi min, Xi max, threshold, isadaptive)
```

Let BP be the collection of boundary point objects that stored in sequence of counterclockwise direction for all outside boundaries and clockwise direction for all inside boundaries:

Let P0 be the collection of background point objects;

```
Let P be the collection of point objects;
Let T be the collection of mesh objects;
Let alpha be the constant that controls shape of
    formed triangles;
Let beta be the constant that controls regularity
    of the triangulation;
Let iteration be the number of loops to refine
    meshes;
Let H_{min} and H_{max} be the minimum and maxi-
    mum element size, respectively;
Let Xi_min and Xi_max be the minimum and
    maximum scaling coefficients, respectively;
Let threshold be the number of minimum increa-
    sing points for each iteration;
Let isadaptive be the flag to generate background
    or adaptive meshes;
Bp. Initialize;
PO. Initialize:
P. Initialize;
T. Initialize:
If. (isadaptive) {
   PO. ReadBackgroundNodes;
   BP. RediscretizeBoundaryNodes;
   };
Else {
   BP. ReadBoundaryNodes;
}:
BP. CreateConvexHull;
P. AddNode (BP. pl, BP. p2, BP. p3, BP. p4);
T. AddTriangle (tl, BP. pl, BP. p2, BP. p3);
T. AddTriangle (t2, BP, p3, BP, p2, BP, p4);
Do p \leftarrow BP. NextBoundaryNode {
   Call DelaunayTriangulation (P, T, \rho);
}:
T. RemoveOutsideDomainTriangles;
Call MeshRefinement
      (P, T, alpha, beta, iteration);
If (isadaptive)
   Call AdaptiveRemeshing
```

```
(P. T. PO, alpha, beta, Hain, Hax, _Xi_min,
Xi max, threshold);
```

- T. MeshRelaxation;
- T. LaplaceSmoothing;

End;

To evaluate the performance of the adaptive remeshing technique with the Delaunay triangulation, the specification of element size, h_i , is given as an analytic function defined for twodimensional domain. The adaptive mesh generation process starts from an initial mesh generated in the domain, then the values of the element sizes at all points are computed by the given function. The mesh generation coupled with the adaptive remeshing procedure is iterated until the resulting mesh becomes globally stable. The iteration process is terminated if the total node increment is fewer than the specified number. The three examples of adaptive mesh generation with the analytical function for specifying element sizes presented herein are: (1) adaptive meshes along the centerline of a rectangular domain, (2) adaptive meshes along the diagonal of a square domain, and (3) an alpha-shape adaptive meshes in a square domain.

Adaptive Meshes along Centerline of a Rectangular Domain: The first example presents an adaptive mesh generation in a 3.0×5.0 rectangular domain. The element sizes at points in the domain are given by the distribution function,

$$h(y) = 0.42 - \frac{1}{\sqrt{2\pi}\sigma} e^{-\left[\frac{y-\mu}{2\sigma}\right]^2}$$
 (6)

where y is the variable and the values of μ and

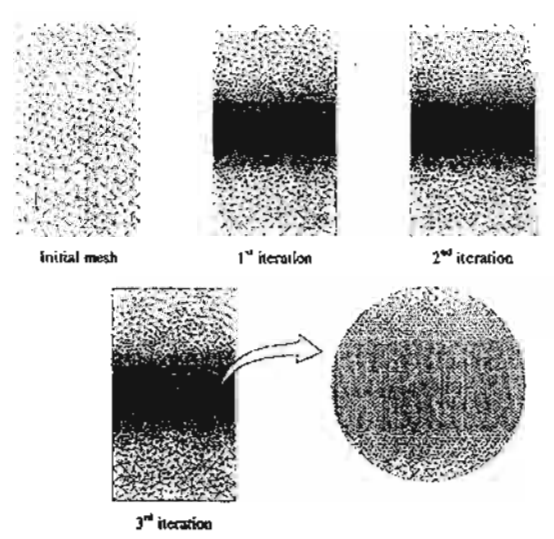


Fig. 1 Adaptive meshes along centerline of a rectangular domain

 σ are constants equal to zero and one, respectively. Figure 1 shows the series of adaptive meshes generated by three iterations based on a coarse initial mesh. The value of mesh generation coefficients. α . β . χ_{min} . χ_{max} are 0.5, 0.6, 0.75, and 1.10, respectively. Due to the prescribed distribution function in Eq. (6), small element sizes are specified around the centerline of the domain. The figure shows that size similarity of the adaptive meshes is generated along the narrow band around the centerline of the domain. The value of χ_{min} limits the number of point insertion along the centerline of the domain, while the value of χ_{max} allows more nodes to be inserted into the other regions.

The specification of scale range and χ_{\min} , χ_{\max} have strong effects on the resulting meshes as shown in Fig. 1. Without the scale range, the mesh is composed of small elements concentrated around line a (see Fig. 2) with progressively larger elements outwards as $h_a < h_b$, h_c . Hence, a mesh consisting of relatively uniform elements in a wider centerline band of the domain may be generated. This mesh has better physical correlation with the behaviors of shocks. The scale range function sorts the nodal spacing values into prescribed intervals according to χ_{\min} and χ_{\max} . In each interval, the generated element sizes are relatively uniform.

Adaptive Meshes along a Diagonal of a Square Domain: The second example concerns with an adaptive mesh generation in a unit square domain. The element sizes are calculated by Eq. $\langle 7 \rangle$ where the constant α is set to 0.5 for this test case. Because this function generates both

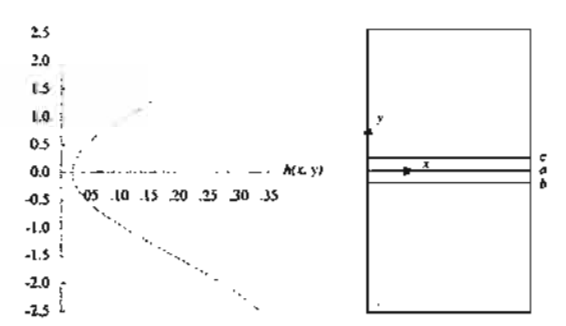


Fig. 2 Distribution of element sizes along the y direction

negative and positive values, only the positive values of this function are used to determine the element size by scaling into the new range of 0.001 and 0.2:

$$h(x, y) = 2y(1-y) \left[\tan^{-1} \beta - \frac{\alpha(1-2x)}{\sqrt{2}(1+\beta^2)} + \frac{\alpha^2 \beta x(1-x)}{2(1+\beta^2)^2} \right] + 2x(1-x) \left[\tan^{-1} \beta - \frac{\alpha(1-2y)}{\sqrt{2}(1+\beta^2)} + \frac{\alpha^2 \beta y(1-y)}{2(1+\beta^2)^2} \right]$$
(7)

where $\beta = \alpha \{(x+y)/\sqrt{2} - 0.8\}$. Figure 3 shows the sequence of adaptive meshes generated by five iterations based on a coarse initial mesh. The value of mesh generation coefficients, α , β , χ_{\min} , χ_{\max} are 0.5, 0.6, 0.4, and 0.75, respectively. The combination of the values of χ_{\min} and χ_{\max} , narrows the band along the diagonal line with small elements.

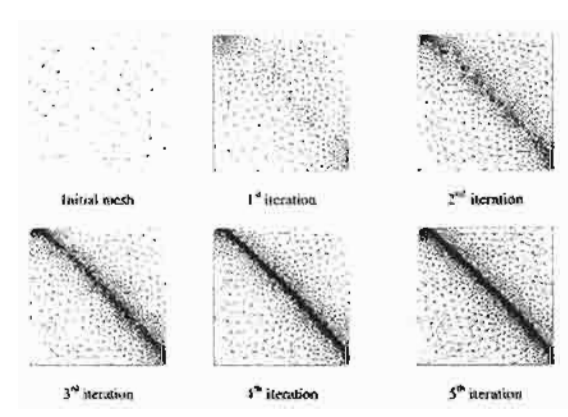


Fig. 3 Adaptive meshes along the diagonal of a square domain

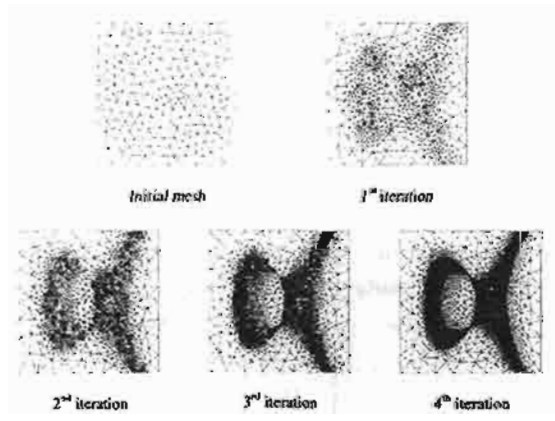


Fig. 4 An alpha-shape adaptive meshes in a square domain

An Alpha-Shape Adaptive Meshes in a Square Domain: The third example presents an alpha-shape adaptive mesh generation in a square domain. The alpha shape function (Borouchaki et al., 1997) is used to calculate element sizes in an 8×8 square domain:

$$h(x, y) = \begin{cases} \min(0.2(\lambda - 1)^3 + 0.005, 1.0) & \text{if } \lambda \ge 1\\ \min(0.2(\lambda - 1)^2 + 0.01, 1.0) & \text{if } \lambda < 1 \end{cases}$$
 (8)

where the value of parameter λ is determined from $x^3-y^2+2-3\lambda x=0$. Figure 4 shows the sequence of four adaptive meshes generated from a coarse initial mesh. The value of mesh generation coefficients, α , β , χ_{\min} , χ_{\max} are 0.5, 0.6, 0.5, and 0.85, respectively. The smaller elements are generated along the alpha-shape in the domain white larger elements are generated in the other regions.

For practical problems, the preferred values of α and β are 0.5 and 0.6, respectively (Karamete et al., 1997). In general, the acceptable ranges of these α and β values are 0.3~0.8, and 0.7~1.3, respectively. In addition, the values of 0.4 and 0.75 are chosen for χ_{min} and χ_{max} , respectively, for all high-speed compressible flow test cases presented later in this paper.

3. High-Speed Compressible Flow Solver

The performance of the Delaunay triangulation, the automatic point creation procedure, and the adaptive remeshing technique has been evaluated by applying to solve high-speed compressible flow problems. The Roc's flux-difference splitting method is widely used for compressible flow solutions due to its efficiency for providing solution accuracy. This section briefly explains the method and its flexibility for combining with adaptive unstructured meshes to further improve the solution accuracy.

Some certain problems for which the Roe's scheme may not provide correct solutions for the compressible Euler computation are presented in this section. Nonphysical numerical solutions may arise from the implementation of the one-dimensional upwinding numerical flux function

onto the multidimensional formulation. To avoid such solutions, a mixed entropy fix method that combines the entropy fix method of Van Leer et al. and the modified multidimensional dissipation method by Pandolfi and D'Ambrosio (2001) is proposed in this paper. Details of these entropy fix methods are presented herein and their performance are determined by test cases. All solutions in this section use the Roe's scheme with the first-order accuracy on structured triangular meshes.

3.1 Roe's flux-difference splitting scheme

The governing differential equations of the Euler equations for the two-dimensional inviscid flow are given by

$$\frac{\partial U}{\partial t} + \frac{\partial E}{\partial x} + \frac{\partial G}{\partial y} = 0 \tag{9}$$

where U is the vector of conservation variables, E and G are the vectors of the convection fluxes in x and y directions, respectively. The perfect gas equation of state is in the form,

$$p = \rho e(\gamma - 1) \tag{10}$$

where ρ is the pressure, ρ is the density, e is the internal energy, and γ is the specific heat ratio. By integrating Eq. (9) over a control volume, Ω , and applying the divergence theorem to the resulting flux integral,

$$\frac{\partial}{\partial t} \int_{\Omega} U d\Omega + \int_{\partial \Omega} \mathbf{F} \cdot \hat{\mathbf{n}} dS = 0 \tag{11}$$

where F is the numerical flux vector and \hat{n} is the unit normal vector of the cell boundary. The numerical flux vector at the cell interface between the left cell L and the right cell R according to the Roe's scheme (1981) is,

$$F_{n} = \frac{1}{2} (F_{nL} + F_{nR}) - \frac{1}{2} \sum_{k=1}^{4} \alpha_{k} |\lambda_{k}| r_{k}$$
 (12)

where α_k is the wave strength of the k^{th} wave, λ_k is the eigenvalue, and r_k is the corresponding right eigenvector. The eigenvalues in the above Eq. (12) are,

$$\lambda_{k} = \begin{bmatrix} V_{n} - a \\ V_{n} \\ V_{n} \\ V_{n} + a \end{bmatrix} \tag{13}$$

where V_n is the normal velocity, and a is the speed of sound at the cell interface.

3.2 The mixed entropy fix method

The original Roc's scheme previously described has been found to produce unphysical solutions of the Euler equations in some certain problems. These include the expansion shock from a flow over a step, and the carbuncle phenomenon of a flow over a blunt body. To avoid such unphysical solutions, the entropy fix methods (Harten, 1983; Van Leer et al., 1989; Pandolfi and D'Ambrosio, 2001; Lin, 1995; Sanders et al., 1998; Dechaumphai and Phongthanapanich, 2003) have been proposed and investigated. By numerical experiment, the Van Leer et al.'s entropy fix method can perform very well for flows with expansion shocks that contain sonic points such as flows over a forward facing step. Meanwhile, the Pandolfi and D'Ambrosio version of the H-correction entropy fix is suitable to correct the numerical instability from insufficient dissipation injected to the entropy and shear waves such as the flow over the blunt body problem. Thus, this paper proposes a mixed entropy fix method that combines the entropy fix method of Van Leer et al. and the modified multidimensional dissipation method by Pandolfi and D'Ambrosio, the modified H-correction, together by replacing the original eigenvalues as follows,

$$\{\lambda_{k}\} = \begin{cases} \frac{|\lambda_{1,k}|}{|\lambda_{1,k}|^{2}}, & |\lambda_{1,k}| \ge 2\eta^{\nu Z} \\ \frac{|\lambda_{1,k}|^{2}}{4\eta^{\nu Z}} + \eta^{\nu Z}, & |\lambda_{1,k}| < 2\eta^{\nu Z} \\ \max(|\lambda_{2,3}|, \eta^{PA}) \end{cases}$$
 (14)

where η^{VL} and η^{PA} are determined from,

$$\eta^{VL} = \max(\lambda_R - \lambda_{L_1} 0) \tag{15}$$

$$\eta^{PA} = \max(\eta_2, \eta_3, \eta_4, \eta_5)$$
(16)

The values η_i , i=2 to 5 as shown in Figures 5(a)-(b) for both the structured and unstructured meshes are given by $\eta_i=0.5\max_{A}(|\lambda_{kR}-\lambda_{kL}|)$ where L and R denote the left and right elements, respectively.

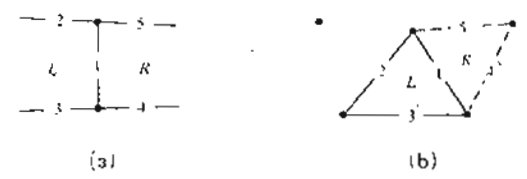


Fig. 5 Cell interfaces of: (a) structured uniform mesh; (b) unstructured triangular mesh

This mixed entropy fix method is equivalent to the Van Leer et al.'s entropy fix method in handling the acoustic waves (for k=1 and 4) and the Pandolfi and D'Ambrosio version of the H-correction entropy fix for the entropy and shear waves (for k=2 and 3). The mixed entropy fix method has been evaluated in this paper using three test cases involving expansion shocks, the carbuncle phenomenon, and the odd-even decoupling These test cases highlight the performance of the proposed entropy fix method on problems with different flow phenomena on structured triangular meshes.

The carbuncle phenomenon: An unrealistic flow solution, the so-called carbuncle phenomenon, of a steady-state flow over a blunt body from the original Roe's scheme was first reported by Perry and Imlay (1988). Such phenomenon refers to a spurious bump on the bow shock near the flow center line ahead of the blunt body. The phenomenon is highly grid-dependent (Pandolfi and D'Ambrosio, 2001), but does not require a large number of grid points to appear (Gressier and Moschetta, 2000). Figures 6(a)-(f) show the computed density contours from the mixed entropy fix method using meshes of three different element aspect ratios. The enlarged views of the elements near the flow center line of the first, second, and the third meshes are also shown in the figures. The carbuncle phenomenon does not appear in all of these meshes with different element aspect ratios.

The Quirk's test (odd-even decoupling): Another test case is a mach 6 moving shock along odd-even grid perturbation in a straight duct (Quirk, 1994). The computational domain consists of a uniform triangular mesh with 800 and 20 equal intervals respectively along the axial



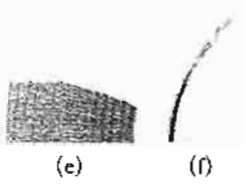


Fig. 6 Mach 15 flow over a blunt body, enlarged view of the mesh and computed density contours: (a) - (b) first mesh; (c) - (d) second mesh; and (e) - (f) third mesh



Fig. 7 Mach 6 moving shock along odd-even grid perturbation

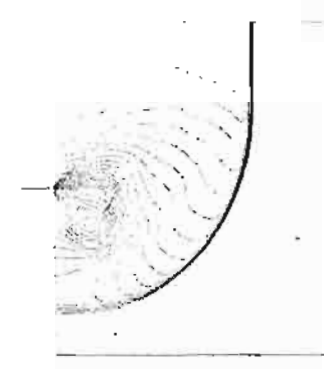


Fig. 8 Diffraction of a Mach 2 shock over a 90° corner

and the transverse directions of the duct. The grids along the duct centerline are perturbed in the transverse direction with a magnitude of $\pm 10^{-6}$. Figure 7 shows the computed density contours of the normal shock at three locations along the duct by the mixed entropy fix method that provides accurate shock resolution.

Shock diffraction: The last test case, the expansion shock problem, used to evaluate the nu-

merical instability is the diffraction of a Mach 2 shock moving over a 90° corner. Figure 8 shows the computed density contours obtained from the mixed entropy fix method. On the other hand, the original Roe's scheme could not provide proper solution due to the negative internal energy that occurs during the computation in the vicinity of the turning corner.

4. Higher-Order Extension and Application on Unstructured Triangular Meshes

4.1 Linear reconstruction for unstructured triangular mesh and temporal discretization

Solution accuracy from the first-order formulation described in the preceding section can be improved by implementing a higher-order formulation for both space and time. A higher-order spatial discretization is achieved by applying the Taylor' series expansion to the cell-centered solution for each cell face (Frink, 1994). For instance, the solutions at the midpoint of an element edge between node 1 and 2 can be reconstructed from,

$$q_{f_{1-2}} = q_c + \frac{\psi_c}{3} \left[\frac{(q_1 + q_2)}{2} - q_3 \right]$$
 (17)

where $q = [\rho \ u \ v \ p]^T$ consists the primitive variables of the density, the velocity components, and the pressure, respectively; q_c is the solution at the element centroid; q_n , n=1, 2, 3 are the solutions at nodes. In this paper, the pseudo-Laplacian method proposed by Holmes and Connell (Holmes and Connell, 1989) is used to determine nodal quantities,

$$q_n = \sum_{i=1}^{N} (w_i q_{C,i}) / \sum_{i=1}^{N} w_i$$
 (18)

where $q_{c,i}$ are the surrounding cell-centered values of node n, w_i is the cell weights, and N is the number of the surrounding cells. The cell weights, w_i , may be differed significantly from unity for some severe distorted meshes as indicated in Ref. (Holmes and Connell, 1989), with suggestion for clipping all the weights in the

range of 0 to 2. In this paper, the clipping of weights is slightly different by modifying only the value of weights of boundary meshes. If any weight becomes negative, its absolute value is used for simplicity. Several examples presented below have shown that such modification performs well. The $\Psi_{\rm C}$ in Eq. (17) represents the limiter for preventing spurious oscillation that may occur in the region of high gradients. In this study, Vekatakrishnan's limiter function (Vekatakrishnan, 1995) is selected.

The second-order temporal accuracy is achieved by implementing the second-order accurate Runge-Kutta time stepping method (Shu and Osher, 1988). To reduce computational effort, the local element time steps are used for steady-state analysis, while the minimum global time step based on the idea in Ref. (Linde and Roe, 1997) is used for the transient analysis.

4.2 Numerical evaluation

The higher-order extension of the Roe's scheme with the proposed entropy fix method described in the preceding section is evaluated by solving several test cases. The modified scheme is also combined with the adaptive meshing technique that generates unstructured triangular meshes for more complex flow phenomena. The selected test cases are: (1) Symmetric rarefaction wave, (2) Oblique shock reflection at a wall, (3) Mach 2 flow in a 15° channel, and (4) Mach 2 shock reflection over a wedge.

Symmetric rarefaction wave: The initial conditions of the flow on the left and right sides of the tube are given by $(\rho, u, p)_L = (7.0, -1.0, 0.2)$ and $(\rho, u, p)_R = (7.0, 1.0, 0.2)$. Such initial conditions are chosen (Linde and Roe, 1997) to produce vacumm at the central region. The 1.0×0.1 computational domain is divided into 400 and 40 equal intervals in the x and y directions, respectively, using all triangular elements. Figures 9(a)-(c) show the first order accurate computed density, pressure and u-velocity distributions along the tube length at time t=0.3 which are compared with the Steger-Warming FVS (Steger and Warming, 1981), AUSM (Liou and Steffen, 1993), HLLC (Toro et al., 1994),

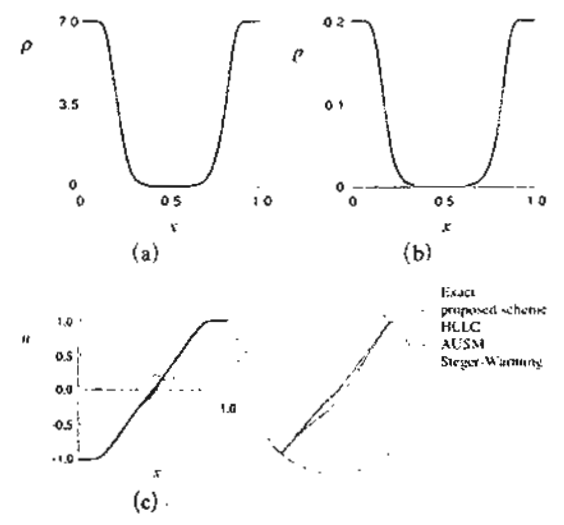


Fig. 9 Comparative exact and computed solutions at time t=0.3 for symmetric rarefaction wave problem $\theta(1)$: (a) density distributions; (b) pressure distributions; and (c) u-velocity distributions

and the exact solutions. The density and pressure distributions are nearly identical for the four schemes. But for the computed u-velocity, the AUSM and the HLLC schemes give less solution accuracy as compared to the Steger-Warming FVS and the proposed schemes in the vicinity of central region. This problem was repeated using the higher-order accurate scheme. Figures 10(a)-(c) show that such higher-order extension of Roe's scheme with the mixed entropy fix method can provide more accurate solution than its first-order solution.

Oblique shock reflection at a wall: The problem statement of an oblique shock reflection at a wall (Yee et al., 1985) on the domain 1.0×4.0 is presented in Fig. 11. The adaptive remeshing technique described is section 2.3 is used to generate adaptive unstructured triangular meshes. The procedure starts by creating a relatively uniform mesh as shown in Fig. 12(a). The fluid analysis is then performed to generate the corresponding solution such as the density contours as shown in Fig. 12(b). This flow solution is then used to generate an adaptive mesh to cluster small elements in the regions of high density gradients, and at the same time, to use larger

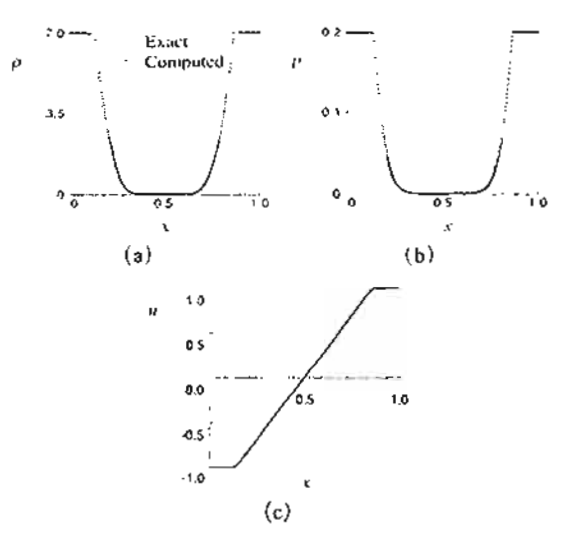


Fig. 10 Comparative exact and computed solutions at time t=0.3 for symmetric rarefaction wave problem $\vartheta(2)$: (a) density distributions; (b) pressure distributions; and (c) u-velocity distributions

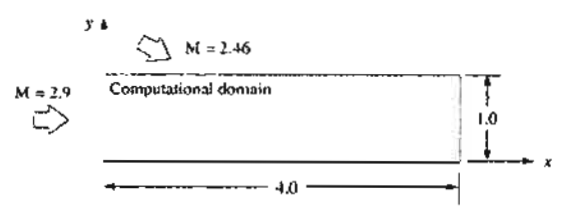


Fig. 11 Problem statement of an oblique shock reflection at a wall

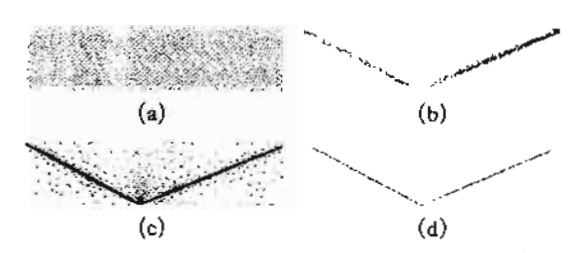


Fig. 12 An oblique shock reflection at a wall: (a) (b) Initial mesh and the corresponding density contours; and (c) -(d) Third adaptive mesh and the corresponding density contours

elements on the other regions. The fluid analysis is then performed again to yield a more accurate solution. The entire process is repeated to

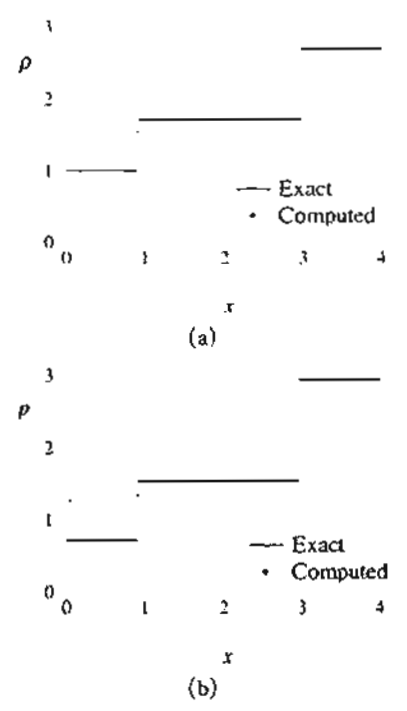


Fig. 13 Comparative solutions of an oblique shock reflection at a wall $\vartheta(2)$: (a) density distribution; and (b) pressure distribution

generate the third adaptive mesh and the corresponding solution as shown in Figs. 12(c)-(d). Figures 13(a)-(b) show comparative density and pressure distributions between the computed and exact solutions at y=0.5. The figures show the higher-order accurate scheme can capture abrupt change of the solutions across the shocks very well.

Mach 2 flow in a 15° channel: Both the first-order and higher-order Roe's schemes with the proposed entropy fix method are evaluated on unstructured meshes by using the problem of a Mach 2 flow in a 15° channel as presented in Fig. 14. The third adaptive mesh and its corresponding density contours computed by using the first-order scheme are shown in Figures 15 (a)-(b), respectively. The analysis of Mach 2 flow in the 15° channel is repeated but with the use of the higher-order scheme. The third adaptive mesh, and its corresponding density contours are shown in Figs. 16(a)-(b). These figures highlight the capability of the higher-order

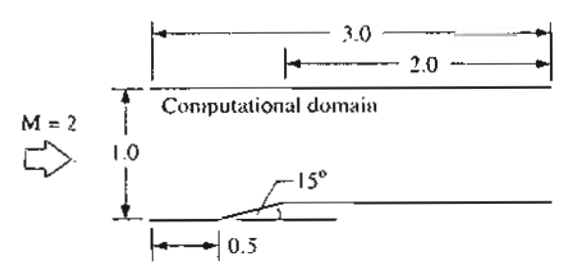


Fig. 14 Problem statement of a mach 2 flow in a 15° channel



Fig. 15 Mach 2 flow in a 15° channel $\vartheta(1)$: (a) Third adaptive mesh; and (b) Density contours



Fig. 16 Mach 2 flow in a 15° channel θ(2): (a) Third adaptive mesh; and (b) Density contours

scheme for providing more detailed flow behavior, such as the stem generated from the shock impinging on the upper wall which could not be captured by the first-order scheme.

Mach 2 shock reflection over a wedge: The computational domain for a Mach 2 shock reflection over a wedge at 46 degrees (Takayama and Jiang, 1997) is illustrated in Figure 17. Figure 18 shows series of the transient adaptive meshes and the corresponding computed density contours at different time instants as the reflection shock starts to form over a wedge. The transient adaptive meshes consist of approximately 20,000 elements in early time before the normal shock reaches the wedge corner, and the number of elements are increased to approximately 28,000 at bottom right image of Fig. 18. The figures highlight the use of the higher-order accurate scheme on adaptive meshes to effectively obtain detailed flow solution.

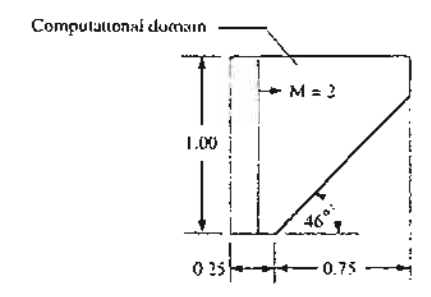


Fig. 17 Problem statement of a Mach 2 shock reflection over a wedge



Fig. 18 Transient adaptive meshes and the computed density contours of a Mach 2 shock reflection over a wedge at four different stages of the computation $\vartheta(2)$

5. Conclusion

A two-dimensional adaptive Delaunay mesh generation algorithm and its application for high-speed compressible flow were presented. The adaptive remeshing technique was described in detail with the pseudo-code presented in object-oriented programming concept. To capture fast variations of the solution effectively, a new element size scaling function was introduced into the adaptive remeshing technique. The combined algorithm was evaluated by generating adaptive meshes for three examples with prescribed element size functions.

A mixed entropy fix method was proposed to improve numerical stability of the Roe's flux-difference splitting scheme for solving high-speed compressible flow problems. The method combines the entropy fixes by Van Leer et al. together with Pandolfi and D'Ambrosio. The method was then evaluated by several well-known test cases and it was found to eliminate unphy-

sical solutions that may arise from the use of the original Roe's scheme. The method was also combined with an adaptive mesh generation technique to demonstrate its applicability for arbitrary unstructured meshes. The entire process was found to provide accurate solutions for both steady-state and transient flow test cases.

Acknowledgment

The authors are pleased to acknowledge the Thailand Research Fund (TRF) for supporting this research work.

References

Borouchaki, H., George, P. L. and Mohammadi, B., 1997, "Delaunay Mesh Generation Governed by Metric Specifications. Part II. Application," *Finite Elements in Analysis and Design*, Vol. 25, pp. 85~109.

Bowyer, A., 1981, "Computing Dirichlet Tessellations," *Computer Journal*, Vol. 24, pp. 162~166

Dechaumphai, P. and Morgan, K., 1992, "Transient Thermal-Structural Analysis using Adaptive Unstructured Remeshing and Mesh Movement," Thermal Structures and Materials for High-Speed Flight, AIAA, Washington, D.C., pp. 205~228.

Dechaumphai, P. and Phongthanapanich, S., 2003, "High-Speed Compressible Flow Solutions by Adaptive Cell-Centered Upwinding Algorithm with Modified H-correction Entropy Fix," Advances in Engineering Software, Vol. 32, pp. 533~538.

Frey, W. H., 1991, "Mesh Relaxation: A New Technique for Improving Triangulations," *International Journal for Numerical Methods in Engineering*, Vol. 31, pp. 1121~1133.

Frink, N. T., 1994, "Recent Progress toward a Three-dimensional Unstructured Navier-Stokes Flow Solver," 32th Aerospace Sciences Meeting, Reno, Nevada, AIAA Paper-94-0061.

Gressier, J. and Moschetta, J. M., 2000, "Robustness versus Accuracy in Shock-wave Computations," *International Journal for Numerical* Methods in Fluids, Vol. 33, pp. 313-332.

Harten, A., 1983, "High Resolution Schemes for Hyperbolic Conservation Laws," *Journal of Computational Physics*, Vol. 49, pp. 357~393.

Holmes, D. G. and Connell, S. D., 1989, "Solution of the 2D Navier-Stokes Equations on Unstructured Adaptive Grids," 9th Computational Fluid Dynamics Conference, Buffalo, New York, AIAA Paper-89-1932-CP.

Kang, H. K., Tsutahara, M., Ro, K. D. and Lec, Y. H., 2002, "Numerical Simulation of Shock Wave Propagation using the Finite Difference Lattice Boltzmann Method," KSME International Journal, Vol. 16, pp. 1327-1335.

Kang, H. K., Tsutahara, M., Ro, K. D. and Lee, Y. H., 2003, "Numerical Analysis of a Weak Shock Wave Propagating in a Medium using Lattice Boltzmann Method (LBM)," KSME International Journal, Vol. 17, pp. 2034~2041.

Karamete, B. K., Tokdemir, T. and Ger, M., 1997, "Unstructured Grid Generation and a Simple Triangulation Algorithm for Arbitrary 2-D Geometries using Object Oriented Programming," International Journal for Numerical Methods in Engineering, Vol. 40, pp. 251~268.

Lin, H. C., 1995, "Dissipation Additions to Flux-Difference Splitting," *Journal of Computational Physics*, Vol. 117, pp. 20-27.

Linde, T. and Roe, P. L., 1997, "Robust Euler Codes," AIAA Paper-97-2098, 13th Computational Fluid Dynamics Conference, Snowmass Village, CO.

Liou, M. S. and Steffen, C. J., 1993, "A New Flux Splitting Scheme," *Journal of Computational Physics*, Vol. 170, pp. 23-39.

Marchant, M. J. and Weatherill, N. P., 1993, "Adaptivity Techniques for Compressible Inviscid Flows," Computer Methods in Applied Mechanics and Engineering, Vol. 106, pp. 83-106.

Pandolfi, M. and D'Ambrosio, D., 2001, "Numerical Instabilities in Upwind Methods: Analysis and Cures for the 'Carbuncle' Phenomenon," *Journal of Computational Physics*, Vol. 166, pp. 271~301.

Perry, K. M. and Imlay, S. T., 1988, "Bluntbody Flow Simulations," 24th AIAA/SAE/ ASME/ASEE Joint Propulsion Conference, Boston, MA, AIAA Paper-88-2904.

Phongthanapanich, S. and Dechaumphai, P., 2004, "Evaluation of Combined Delaunay Triangulation and Remeshing for Finite Element Analysis of Conductive Heat Transfer," Transactions of the Canadian Society for Mechanical Engineering, Vol. 27, pp. 319~340.

Probert, J., Hassan, O., Peraire, J. and Morgan, K., 1991, "An Adaptive Finite Element Method for Transient Compressible Flows," *International Journal for Numerical Methods in Engineering*, Vol. 32, pp. 1145~1159.

Quirk, J. J., 1994, "A Contribution to the Great Riemann Solver Debate," *International Journal for Numerical Methods in Fluids*, Vol. 18, pp. 555~574.

Roe, P. L., 1981, "Approximate Riemann Solvers, Parameter Vectors, and Difference Schemes," *Journal of Computational Physics*, Vol. 43, pp. 357~372.

Sanders, R., Morano, E. and Druguet, M. C., 1998, "Multidimensional Sissipation for Upwind Schemes: Stability and Applications to Gas Dynamics," *Journal of Computational Physics*, Vol. 145, pp. 511~537.

Shu, C. W. and Osher, S., 1988, "Efficient Implementation of Essentially Non-Oscillatory Shock-capturing Schemes," *Journal of Computational Physics*, Vol. 77, pp. 439~471.

Steger, J. L. and Warming, R. F., 1981, "Flux Vector Splitting of the Inviscid Gasdynamic Equations with Applications to Finite Difference Methods," *Journal of Computational Physics*, Vol. 40, pp. 263~293.

Takayama, K. and Jiang, Z., 1997, "Shock Wave Reflection over Wedges: a Benchmark Test for CFD and Experiments," Shock Waves, Vol. 7, pp. 191~203.

Toro, E. F., Spruce, M. and Speares, W., 1994, "Restoration of the Contact Surface in the HLL-Riemann Solver," *Shock Waves*, Vol. 4, pp. 25-34.

Van Leer, B., Lee, W. T. and Powell, K. G., 1989, "Sonic-Point Capturing," 9th Computational Fluid Dynamics Conference, Buffalo, New York, AIAA Paper-89-1945-CP.

Vekatakrishnan, V., 1995, "Convergence to

Steady State Solutions of the Euler Equations on Unstructured Grids with Limiters," Journal of Computational Physics, Vol. 118, pp. 120-130.

Watson, D. F., 1981, "Computing the n-Dimensional Delaunay Tessellation with Application to Voronoi Polytopes," Computer Journal,

Vol. 24, pp. 167~172.

Yee, H. C., Warming, R. F. and Harten, A., 1985, "Implicit Total Variation Diminishing (TVD) Schemes for Steady-state Calculations," *Journal of Computational Physics*, Vol. 57, pp. 327-360.

บทความทางวิชาการ เรื่อง

Flux-Diffrence Splitting Scheme with Multidimensional Dissipation on Unstructured Meshes

Published in the

Journal of the Chinese Institute of Engineers

Vol. 27, No. 7, pp. 981-992

2005

FLUX-DIFFERENCE SPLITTING SCHEME WITH MODIFIED MULTIDIMENSIONAL DISSIPATION ON UNSTRUCTURED MESHES

Sutthisak Phongthanapanich and Pramote Dechaumphai*

ABSTRACT

A flux-difference splitting scheme with a modified multidimensional dissipation for high-speed compressible flow analysis on unstructured meshes is presented. The scheme eliminates unphysical flow behaviors such as a spurious bump of the carbuncle phenomenon that occurs on the bow shock from flow over a blunt body, and the expansion shock generated from flow over a forward facing step. The switching function suggested by Quirk is implemented as a choice to detect the vicinity of strong shock. The proposed scheme is further extended to obtain higher-order spatial and temporal solution accuracy. The scheme is, in addition, combined with an adaptive meshing technique that generates unstructured triangular meshes to resemble the flow phenomena for reducing computational effort. The entire procedure is evaluated by solving several benchmarks as well as steady-state and transient high-speed compressible flow problems.

Key Words: shock instabilities, carbuncle phenomenon, Roe's FDS, entropy fix, H-correction.

I. INTRODUCTION

High-speed compressible flows normally involve complex flow phenomena, such as strong shock waves, shock-shock interactions and shear layers. Various numerical inviscid flux formulations have been proposed to solve an approximate Riemann problem. Among these formulations, the flux-difference splitting scheme by Roe (1981) is widely used due to its accuracy, quality and mathematical clarity. However, the scheme may sometimes lead to unphysical flow solutions in certain problems, such as the carbuncle phenomenon (Perry and Imlay, 1988) with a spurious bump in the bow shock from flow over a blunt body. The scheme may not provide an accurate solution for the complex impinging shock phenomenon yielding kinked mach stem (Quirk, 1994) generated from a moving shock over a ramp. In the oddeven decoupling problem, an unrealistic perturbation

It has been known, for some time, that Roe's original scheme does not satisfy the entropy condition and may allow unrealistic expansion shock. Harten (1983) proposed an entropy fix formulation to replace the near zero small eigenvalues by some tolerances. The mathematical background of Harten's entropy fix with the suggested tolerance values was given by Van Leer et al. (1989).

The main objectives of this paper are to propose and evaluate a modified Roe's scheme on adaptive unstructured meshes for two-dimensional high-speed compressible flow analysis. The entropy fix method by Van Leer et al. (1989) and the multidimensional dissipation technique given by Pandolfi and D'Ambrosio (2001) are modified for unstructured triangular meshes and implemented into Roe's original scheme. To prevent unnecessary dissipation injection in some cases, the switching function suggested by Quirk may be applied as a choice to detect the

may grow with the planar shock as it moves along the duct. To improve the solution accuracy of these problems, Quirk pointed out that the original Roe's scheme should be modified or replaced by other schemes in the vicinity of a strong shock.

^{*}Corresponding author. (Tel: 66-2-2186621; Fax: 66-2-218-6621; Email: fmepdc@eng.chula.ac.th)

The authors are with the Mechanical Engineering Department, Chulalongkorn University, Bangkok 10330, Thailand.

vicinity of a strong shock.

The presentation in this paper starts at Section II describing some well-known problems which exhibit numerical shock instability from Roe's scheme. The entropy fix methods of Van Leer et al. (1989), Sanders et al. (1998), and Pandolfi and D'Ambrosio (2001) are examined to investigate their capabilities, as well as solution accuracy. A modified Roe's scheme with a mixed entropy fix method is then proposed. The presented scheme is further extended to higher-order solution accuracy and then evaluated by several benchmark test cases in Section III. Finally, the performance of the scheme is evaluated on adaptive unstructured meshes for solving both steady-state and transient high-speed compressible flow problems.

II. NUMERICAL SHOCK INSTABILITY AND MIXED ENTROPY FIX METHOD FOR ROE'S SCHEME

Some problems in which Roe's scheme may not provide correct solutions for the compressible Euler computation are presented in this section. Unphysical numerical solutions may arise from the implementation of the one-dimensional upwinding numerical flux function onto the multidimensional formulation. To avoid such solutions, the three entropy fix methods (Van Leer et al., 1989; Pandolfi and D'Ambrosio, 2001; Sanders et al., 1998) have been recently suggested because of their simplicity and convenient code implementation. A mixed entropy fix method that combines the entropy fix method of Van Leer et al. (1989) and the modified multidimensional dissipation method by Pandolfi and D'Ambrosio (2001), is proposed in this paper. Details of these entropy fix methods are presented herein and their performance determined by test cases. All solutions in this section use the Roe's scheme with the first-order accuracy on unstructured triangular meshes.

1. Roe's Flux-Difference Splitting Scheme with Dissipation

The governing differential equations of the Euler equations for two-dimensional inviscid flow are given by,

$$\frac{\partial U}{\partial t} + \frac{\partial E}{\partial x} + \frac{\partial G}{\partial y} = 0 \tag{1}$$

where U is the vector of conservation variables, E and G are the vectors of the convection fluxes in x-and y-directions, respectively. The perfect gas equation of state is in the form,

$$p = \rho e(\gamma - 1) \tag{2}$$

where p is the pressure, p is the density, e is the internal energy, and γ is the specific heat ratio.

By integrating Eq. (1) over a control volume, Ω , and applying the divergence theorem to the resulting flux integral,

$$\frac{\partial}{\partial t} \int_{\Omega} U d\Omega + \int_{\partial \Omega} F \cdot \hat{n} dS = 0$$
 (3)

where F is the numerical flux vector and \bar{n} is the unit normal vector of the cell boundary. The numerical flux vector at the cell interface between the left cell L and the right cell R according to Roe's scheme (1981) is

$$F_n \simeq \frac{1}{2} (F_{nL} + F_{nR}) - \frac{1}{2} \sum_{k=1}^{4} \alpha_k |\hat{\lambda}_k| r_k$$
 (4)

where α_k is the wave strength of the k^{th} wave, λ_k is the eigenvalue, and r_k is the corresponding right eigenvector. The eigenvalues in the above Eq. (4) are

$$\lambda_{k} = \begin{bmatrix} V_{n} - a \\ V_{n} \\ V_{n} \\ V_{n} + a \end{bmatrix}$$
 (5)

where V_n is the normal velocity, and a is the speed of sound at the cell interface.

Roe's original scheme, previously described, has been found to produce unphysical solutions of the Euler equations in certain problems. These include the expansion shock from a flow over a step, and the carbuncle phenomenon of a flow over a blunt body. To avoid such unphysical solutions, the entropy fix methods (Harten, 1983; Van Leer et al., 1989; Lin, 1995; Sanders et al., 1998; Pandolfi and D'Ambrosio, 2001) have been proposed and investigated. The performance of these three versions of entropy fix methods are first evaluated for structured meshes herein. These methods are then extended to unstructured meshes and presented in this paper later.

Van Leer's entropy fix method (RoeVL) is designed to correct unphysical expansion shock. The one-dimensional entropy fix was developed by replacing the characteristic speeds of the acoustic waves (for k=1 and 4) with

$$\left|\lambda_{k}\right|^{*} = \begin{cases} \left|\lambda_{k}\right|, & \left|\lambda_{k}\right| \geq 2\eta^{VL} \\ \left|\frac{\left|\lambda_{k}\right|^{2}}{4\eta^{VL}} + \eta^{VL}, & \left|\lambda_{k}\right| < 2\eta^{VL} \end{cases}$$
 (6)

where

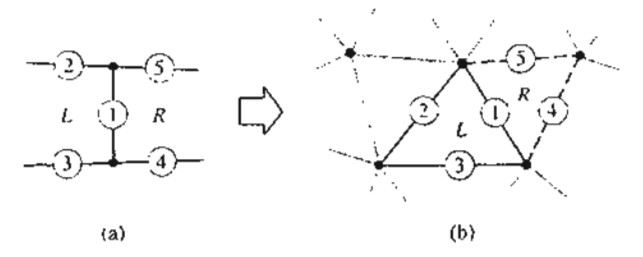


Fig. 1 Cell interfaces of: (a) structured uniform mesh; (b) unstructured triangular mesh.

$$\eta^{\prime\prime} = \max(\lambda_R - \lambda_L, 0) \tag{7}$$

Sanders et al. (1998) introduced an idea of multidimensional dissipation, the so-called H-correction entropy fix method. The method has been shown to eliminate the unrealistic carbuncle phenomenon of the flow over a blunt body by using the structured uniform mesh as shown in Fig. 1(a). The advantages of the method are the simplicity in the implementation into the existing scheme and the parameter-free characteristics. For the two triangular cells shown in Fig. 1(b), the H-correction entropy fix according to Sanders et al. (1998), (RoeSA) has been modified as described by Dechaumphai and Phongthanapanich (2003) to

$$\eta^{SA} = \max(\eta_1, \eta_2, \eta_3, \eta_4, \eta_5)$$
 (8)

where η_i , i=1 to 5 are

$$\eta_i = \frac{1}{2} \max(|\lambda_{kR} - \lambda_{kL}|) \tag{9}$$

Pandolfi and D'Ambrosio (2001) proposed another version of the H-correction entropy fix by excluding the η_1 from Eq. (8) to avoid an erroneous injection of artificial viscosity, and this method is applicable only to entropy and shear waves (for k=2 and 3). The method was used by Druguet and Zeitoun (2003) to study shock wave reflections in supersonic steady flows. The modified H-correction entropy fix by Pandolfi and D'Ambrosio (2001), (RoePA) is

$$\eta^{PA} = \max(\eta_2, \, \eta_3, \, \eta_4, \, \eta_5)$$
 (10)

where η_i , i=2 to 5 are given in Eq. (9).

It has been found that the above three methods, namely the RoeVL, RoeSA and RoePA, perform well on certain problems but may fail for others. For example, as presented later, the RoeVL can perform very well for flows with expansion shocks that contain sonic points such as the flow over a forward facing step. Meanwhile, the RoePA is suitable to correct the numerical instability from insufficient dissipation injected to the entropy and shear waves such as the kinked mach stem problem and the flow over the blunt

body problem. Thus, this paper proposes a mixed entropy fix method (RoeVLPA) that combines the entropy fix method of Van Leer et al. (1989) and the modified multidimensional dissipation method by Pandolfi and D'Ambrosio (2001), the modified H-correction, by replacing the original eigenvalues as follows

$$\left\{ \lambda_{k} \right\} = \begin{cases} \left| \lambda_{1,4} \right|, & \left| \lambda_{1,4} \right| \ge 2\eta^{VL} \\ \frac{\left| \lambda_{1,4} \right|^{2}}{4\eta^{VL}} + \eta^{VL}, & \left| \lambda_{1,4} \right| < 2\eta^{VL} \\ \max(\left| \lambda_{2,3} \right|, \eta^{PA}) \end{cases}$$
(11)

where η^{VL} and η^{PA} are defined in Eqs. (7) and (10), respectively. This mixed entropy fix method (RoeVLPA) is equivalent to the RoeVL in handling acoustic waves (for k=1 and 4) and the RoePA for entropy and shear waves (for k=2 and 3).

The above four methods have been evaluated using five test cases involving expansion shocks, the kinked mach stem, the carbuncle phenomenon, and the odd-even decoupling as presented in the following sections. These test cases highlight the performance of the RoePA, RoeSA, RoeVL, and the proposed RoeVLPA on problems with different flow phenomena on structured triangular meshes.

2. The Expansion Shocks

Roe's original scheme may produce an unphysical expansion shock because it does not satisfy the entropy condition. To illustrate this phenomenon, a Mach 3 flow over a forward facing step (Woodward and Colella, 1984) is investigated. The density contours computed from the RoePA, RoeSA, RoeVL, and RoeVLPA are shown in Fig. 2(a)-(d), respectively. The figures show that the RoePA produces an unphysical expansion shock on top of the step corner, whereas the RoeSA, RoeVL, and RoeVLPA provide realistic solutions.

Another expansion shock problem used to evaluate numerical instability is the diffraction of a Mach 2 shock moving over a 90° corner. Figs. 3(a) and (b) show the computed density contours obtained from the RoeVL and RoeVLPA, respectively. On the other hand, neither RoePA nor RoeSA could provide a proper solution due to negative internal energy that occurs during the computation in the vicinity of the turning corner.

3. The Kinked Mach Stem

The kinked mach stem generated from a shock

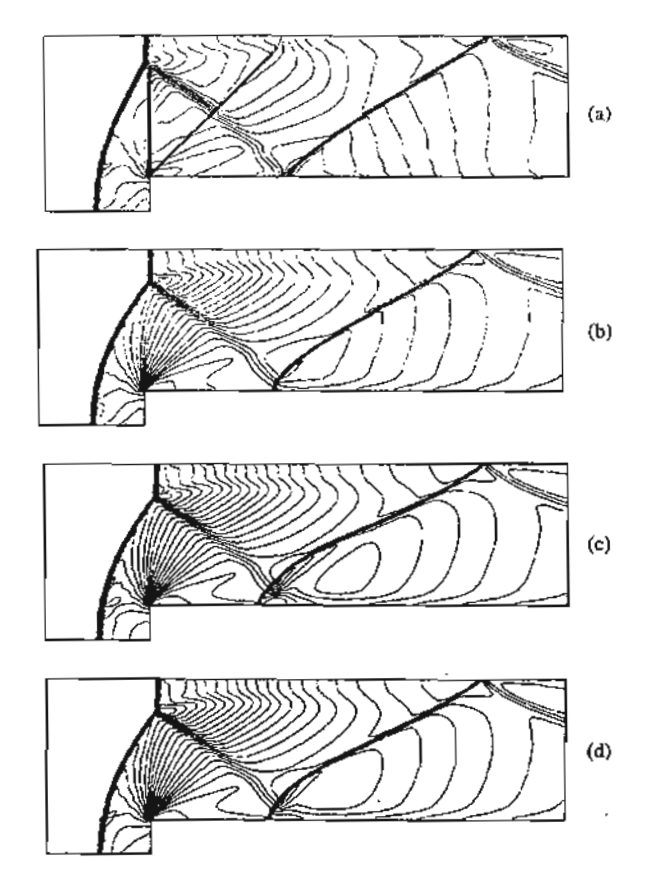


Fig. 2 Mach 3 flow over a forward facing step: (a) RoePA; (b) RoeSA; (c) RoeVL; and (d) RoeVLPA.

moving over a ramp is another test case used to highlight the performance of these four methods. Figs. 4(a)-(d) respectively show the density contours obtained from the RoePA, RoeSA, RoeVL, and RoeVLPA for a Mach 5 normal shock moving over a 46° ramp. The RoePA, RoeSA and RoeVLPA provide reasonably accurate solutions, such that the kinked mach stem is recovered with the slightly broken-down incident shock. The RoeVL, however, yields a brokendown incident shock with severely kinked mach stem. Such a solution may be caused by insufficient dissipation that cannot counteract the transverse perturbation (Quirk, 1994; Gressier and Moschetta, 2000).

4. The Carbuncle Phenomenon

An unrealistic flow solution, the so-called carbuncle phenomenon, of a steady-state flow over a blunt body from Roe's original scheme was first reported by Perry and Imlay (1988). Such a phenomenon refers to a spurious bump on the bow shock near the flow center line ahead of the blunt body. The phenomenon is highly grid-dependent (Pandolfi and D'Ambrosio, 2001), but does not require a large number of grid points to appear (Gressier and

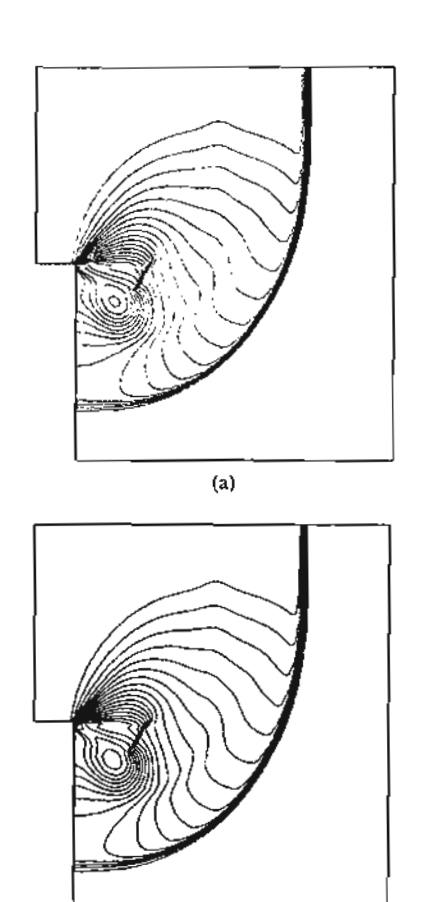


Fig. 3 Diffraction of a Mach 2 shock over a 90° corner: (a) RoeVL; and (b) RoeVLPA.

Moschetta, 2000). To demonstrate this grid-dependent phenomenon, the RoePA, RoeSA, RoeVL, and RoeVLPA methods are employed with three meshes of different element aspect ratios. An enlarged view of the elements near the flow centerline of the first mesh and the corresponding density contours are shown in Figs. 5(a)-(e). The carbuncle phenomenon does not appear in any scheme with the use of this relatively crude mesh. The second mesh has more elements which are refined in the circumferential direction as shown in Fig. 6(a). The RoePA and RoeVLPA provide realistic flow behavior while the RoeSA and RoeVL exhibit small bumps on the bow shock as shown in Figs. 6(b)-(e). The carbuncle phenomenon can be clearly seen in a more refined mesh with higher element aspect ratio as shown in Fig. 7(a). While the RoePA and the proposed RoeVLPA still provide reasonable flow solutions, the carbuncle phenomena are easily observed in the RoeSA and RoeVL as shown in Figs. 7(b)-(e).

5. The Quirk's Test (Odd-Even Decoupling)

The last test case is a Mach 6 moving shock

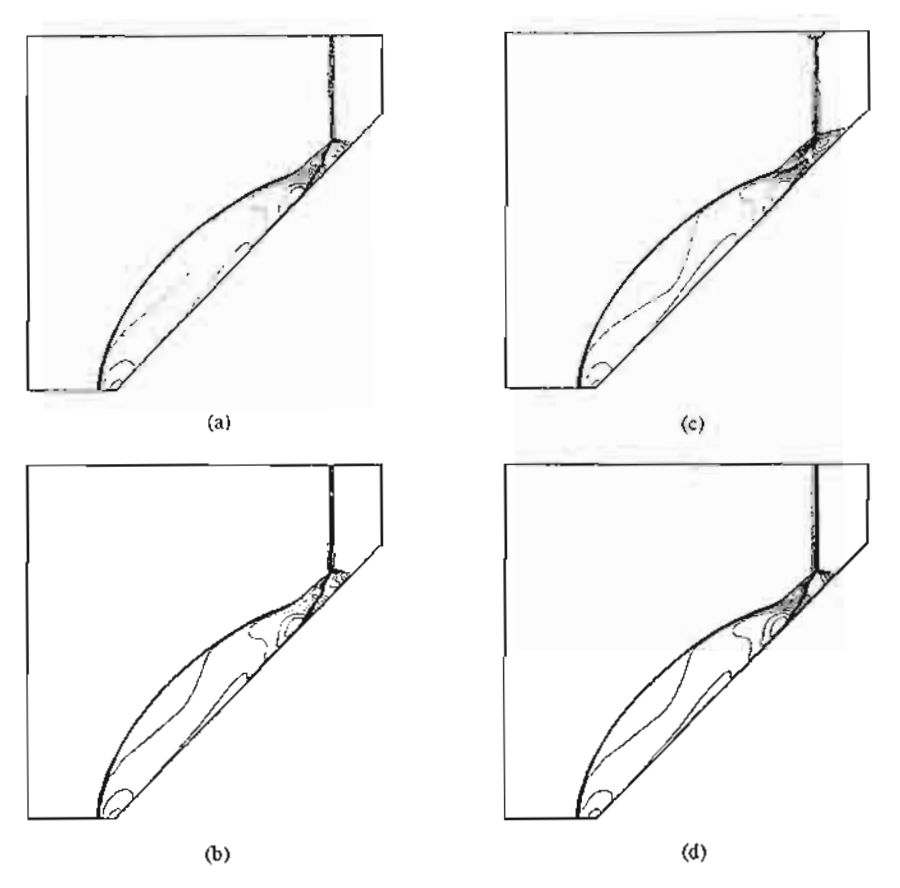


Fig. 4 A kinked much stem from a Mach 5 shock moving over a 46° ramp: (a) RoePA; (b) RoeSA; (c) RoeVL; and (d) RoeVLPA.

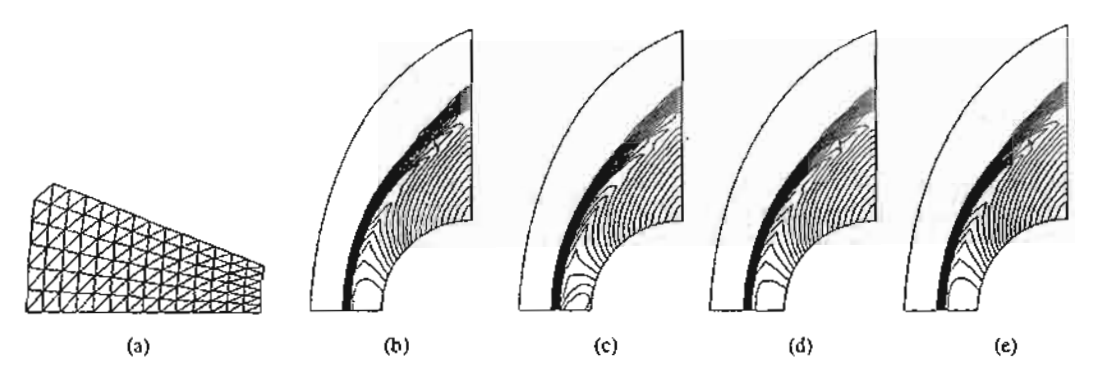


Fig. 5 Mach 15 flow over a blunt body (first mesh): (a) enlarged view of the mesh; (b) RoePA; (c) RoeSA; (d) RoeVL; and (e) RoeVLPA.

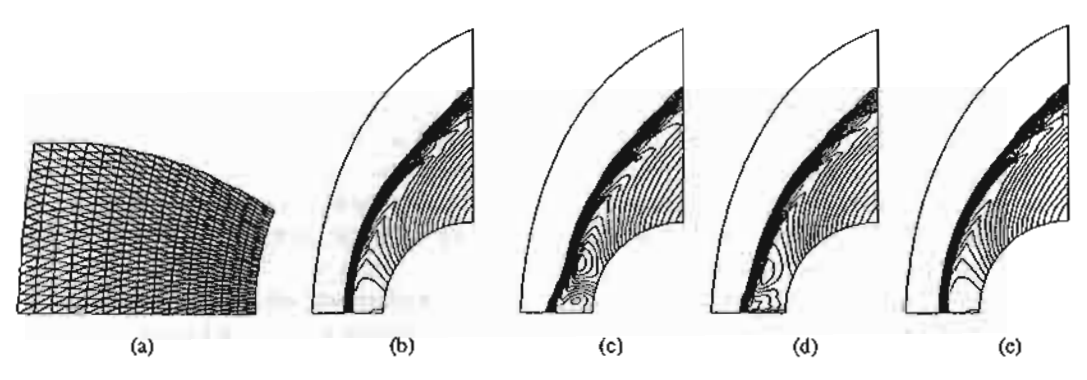


Fig. 6 Mach 15 flow over a blunt body (second mesh): (a) enlarged view of the mesh; (b) RocPA; (c) RoeSA; (d) RoeVL; and (e) RoeVLPA.

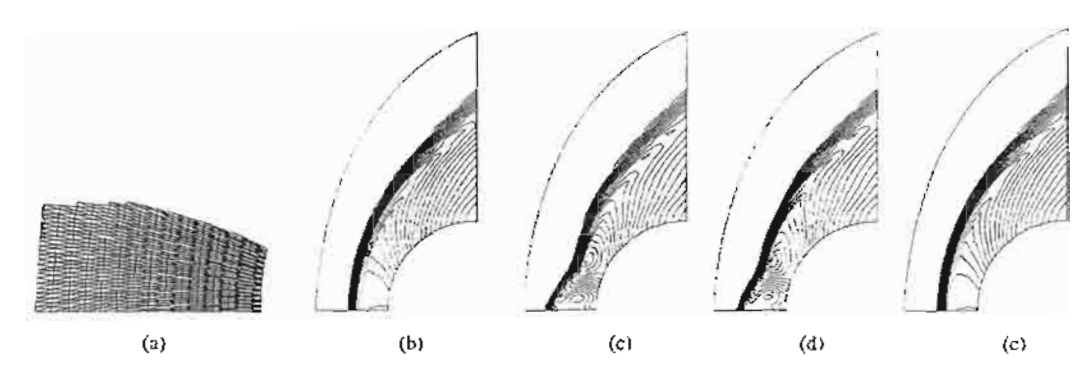


Fig. 7 Mach 15 flow over a blunt body (third mesh): (a) enlarged view of the mesh; (b) RoePA; (c) RoeSA; (d) RoeVL; and (e) RoeVLPA

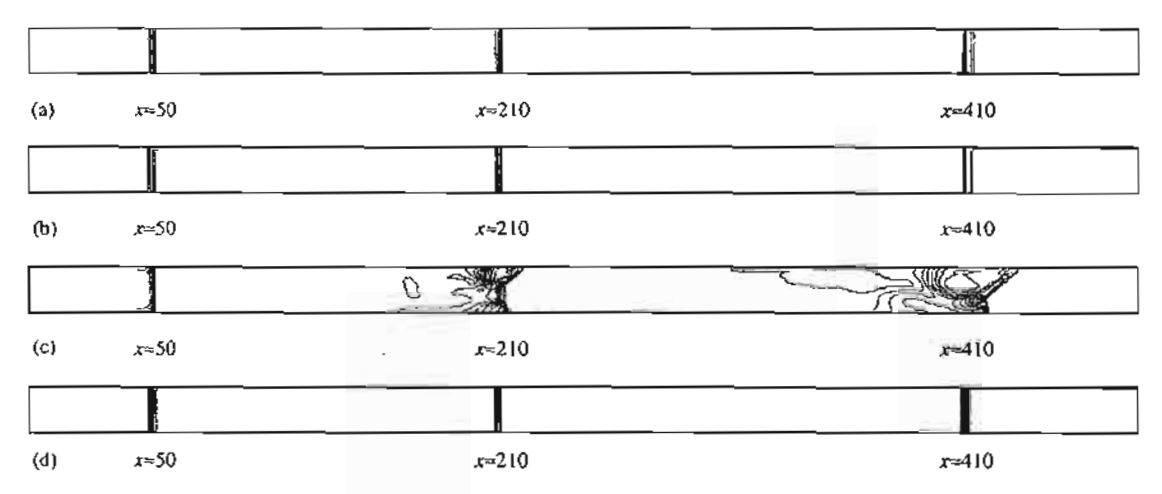


Fig. 8 Mach 6 moving shock along odd-even grid perturbation: (a) RoePA; (b) RocSA; (c) RocVL; and (d) RocVLPA.

along odd-even grid perturbation in a straight duct (Quirk, 1994). The computational domain consists of a uniform triangular mesh with 800 and 20 equal intervals respectively along the axial and the transverse directions of the duct. The grids along the duct centerline are perturbed in the transverse direction with magnitude of ±10-6. Figs. 8(a)-(d) show the computed density contours of the normal shock at the three locations along the duct by the RoePA, RoeSA, RoeVL, and RoeVLPA, respectively. The RoePA, RoeSA, and RoeVLPA can provide accurate shock resolution whereas the RoeVL suffers from numerical instabilities. As explained by Gressier and Moschetta (2000), the exact capture of contact discontinuity and strict stability cannot be simultaneously satisfied in any upwind scheme. The solution suggests that additional dissipation injection to the entropy and shear waves is thus needed to stabilize Roe's scheme as done by RoePA, RoeSA, and RocVLPA.

The results obtained from the above five test cases show that the proposed RoeVLPA method performs well to provide realistic flow solutions for all test cases.

6. Quirk's Pressure Switching Function

Roe's original flux-difference splitting scheme may not provide a stable solution in the vicinity of a strong shock. Quirk (1994) suggested that the scheme should be replaced by a more dissipative scheme such as the HLLE scheme (Einfeldt, 1988) in such a region. To detect the vicinity of a strong shock, Quirk proposed a pressure switching function,

$$\frac{|p_{L} - p_{R}|}{\min(p_{L}, p_{R})} > \alpha \tag{12}$$

where α is a threshold parameter which is problem-dependent; p_L and p_R are the pressures of the left and right cells that act on the cell interface.

This pressure switching function has been examined as a condition for modifying the eigenvalues that correspond to the entropy and shear waves of the proposed RoeVLPA method. The test case of the Mach 6 moving shock along the odd-even grid perturbation in a straight duct is repeated with the use of the above switching function. Figs. 9(a)-(b) show density contours obtained from the RoeVLPA method with the pressure

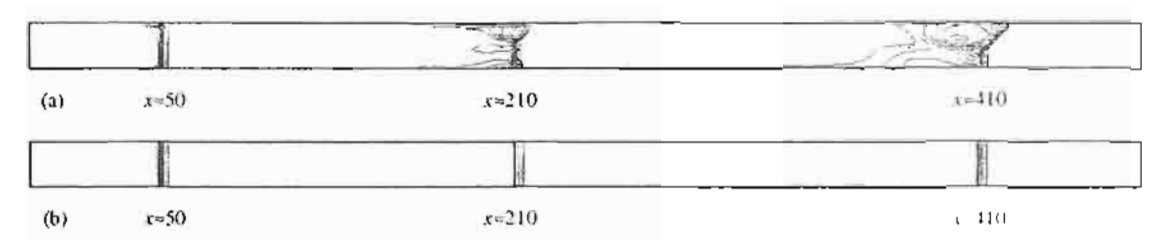


Fig. 9. A Mach 6 moving shock along odd-even grid perturbation (RoeVLPA and Quirk's switching function): (a) α=2; and (b) α=4.

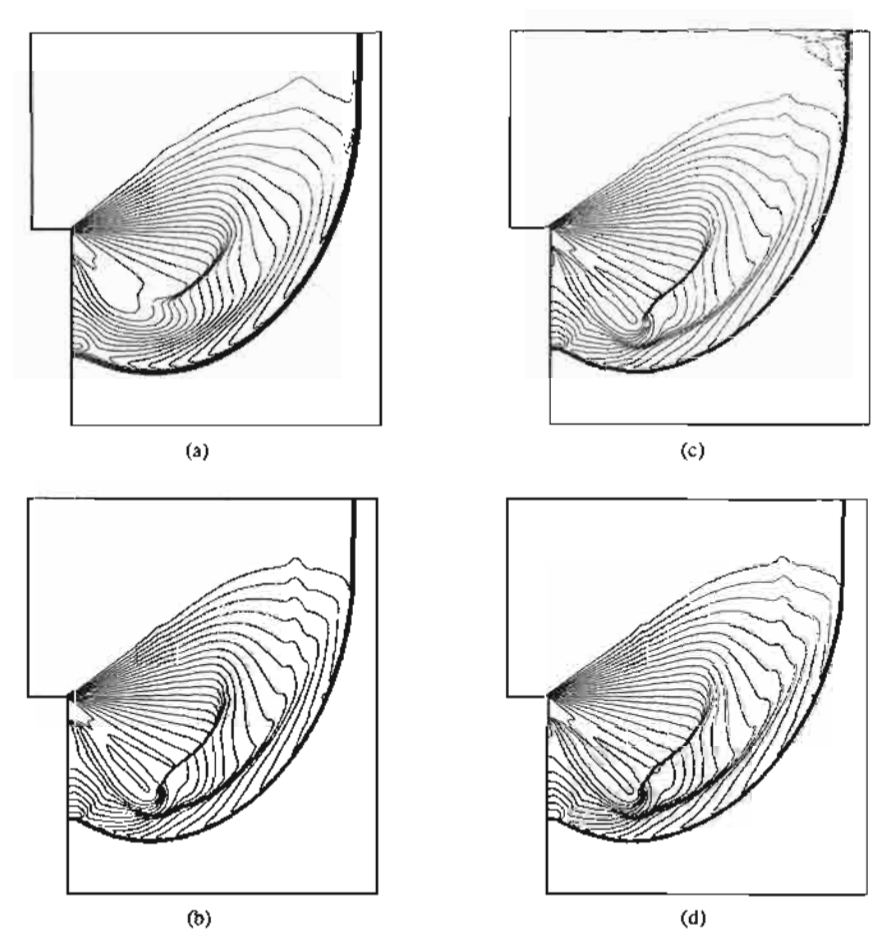


Fig. 10 Density contours of a diffraction of Mach 5.09 shock over a 90° corner at time t=0.25: (a) $\theta(1)$ -RoeVLPA: (b) $\theta(2)$ -RoeVLPA with $\alpha=15$; and (d) $\theta(2)$ -RoeVLPA with $\alpha=1$.

switching function of $\alpha=2$ and 1, respectively. The figures clearly indicate that the quality of the shock resolution depends on the selected threshold values. This example, however, also shows that the suggested replacement of Roe's original scheme by a more dissipative scheme in the vicinity of strong shock can be avoided. The proposed RoeVLPA method may be used for the entire computational domain if the threshold parameter is selected properly. The Quirk's pressure switching function described in this section will be examined again for the problem of Mach 5.09 shock over a 90° corner as shown in Fig. 10. But for the rest of the problems presented in this paper, all computations are performed without activating this Quirk's pressure switching function.

III. HIGHER-ORDER EXTENSION AND APPLICATION ON UNSTRUCTURED TRIANGULAR MESHES

1. Linear Reconstruction and Limiter

Solution accuracy from the first-order formulation described in the preceding section can be improved using a higher-order formulation for both space and time. A higher-order spatial discretization is achieved by applying the Taylor's series expansion to the cell-centered solution for each cell face (Frink et al., 1991). For instance, the solutions at the midpoint of an element edge between node I and 2 shown in Fig. 11, can be reconstructed from

$$q_{f_{1-2}} = q_C + \frac{\Psi_C}{3} \left[\frac{(q_1 + q_2)}{2} - q_3 \right]$$
 (13)

where $q=[p\ u\ v\ p]^r$ consists of the primitive variables of the density, the velocity components, and the pressure, respectively; q_C is the solution at the element centroid; q_n , n=1,2,3 are the solutions at nodes. In this paper, the inverse-distance weighting from the centroid to the nodes that preserves the principle of positivity (Frink and Pirzadeh, 1998) is used

$$q_n = \sum_{i=1}^{N} \frac{q_{C,i}}{|\vec{r}_i|} / \sum_{i=1}^{N} \frac{1}{|\vec{r}_i|}$$
 (14)

where $q_{C,i}$ are the surrounding cell-centered values of node n, $|\vec{r}_i|$ is the distance from the centroid to node n, and N is the number of the surrounding cells.

The Ψ_C in Eq. (13) represents the limiter for preventing spurious oscillation that may occur in the region of high gradients. In this study, Vekatakrishnan's limiter function (Venkatakrishnan, 1995) is selected,

$$\Psi_{C} = \min_{i=1,2,3} \begin{cases}
\phi(\frac{\Delta_{+,\max}}{\Delta_{-}}), & \Delta_{-} \ge 0 \\
\phi(\frac{\Delta_{+,\min}}{\Delta_{-}}), & \Delta_{-} < 0 \\
1, & \Delta_{-} = 0
\end{cases} (15)$$

where $\Delta_{-}=q_c-q_i$, $\Delta_{+, max}=q_{max}-q_i$, and $\Delta_{+, min}=q_{min}-q_i$. The q_{max} and q_{min} are respectively the maximum and minimum values of all distance-one neighbouring cells. The function ϕ is similar to the Van Albada limiter (Van Albada et al., 1982) which is expressed in the form

$$\phi(y) = \frac{y^2 + 2y + \varepsilon^2}{y^2 + y + 2 + \varepsilon^2}$$
 (16)

The value ε^2 is equal to $(Kh)^3$, where K is a constant of 5 in this paper and h is the average mesh size.

2. Second-Order Temporal Discretization

Second-order temporal accuracy is achieved by implementing the second-order accurate Runge-Kutta time stepping method (Shu and Osher, 1988)

$$U_{i}^{*} = U_{i}^{n} - \frac{\Delta t}{\Omega_{i}} \sum_{j=1}^{3} F^{n} \cdot n_{j}$$

$$U_{i}^{n+1} = \frac{1}{2} [U_{i}^{0} + U_{i}^{*} - \frac{\Delta t}{\Omega_{i}} \sum_{j=1}^{3} F^{*} \cdot n_{j}]$$
(17)

where Δt is the time step. To reduce the computation effort, the local element time steps are used for steady-state analysis, while the minimum global time step based on spectral radii (Vijayan and Kallinderis, 1994) is used for transient analysis.

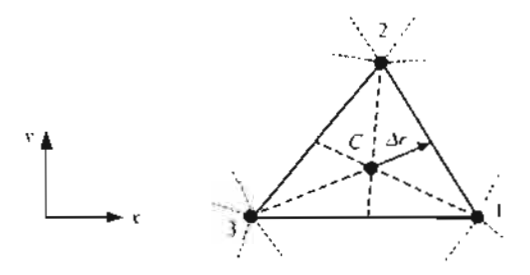


Fig. 11 Linear reconstruction on a typical triangular element

3. Numerical Evaluation

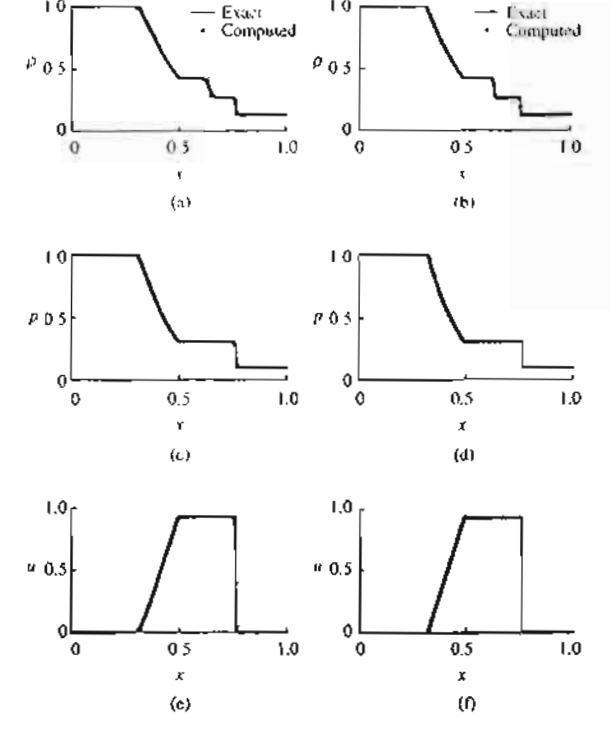
The higher-order extension of Roe's scheme with the proposed entropy fix method described in the preceding section is evaluated by solving several test cases. The modified scheme is also combined with an adaptive meshing technique that generates unstructured triangular meshes for more complex flow phenomena. The selected test cases are: (1) Sod shock tube, (2) Diffraction of Mach 5.09 shock over a 90° corner, (3) Oblique shock reflection at a wall, (4) Mach 2 flow in a 15° channel, and (5) Mach 2 shock reflection over a wedge.

(i) Sod Shock Tube

The one-dimensional shock tube test case, the so-called Sod shock tube (Sod, 1978), is solved by using a two-dimensional domain. The initial conditions of the fluids on the left and right sides are given by $(\rho, u, \rho)_L$ =(1.0, 0.0, 1.0) and $(\rho, u, \rho)_R$ =(0.125, 0.0, 0.1). The 1.0×0.1 computational domain is divided into 400 and 40 equal intervals in the x- and y-directions, respectively. The domain is discretized with uniform triangular elements. Figs. 12(a)-(f) show the computed density, pressure and u-velocity distributions along the tube length which are compared with the exact solutions at time t=0.15. The figures show that the higher-order extension of Roe's scheme with the entropy fix RoeVLPA method provides more accurate solutions than its first-order solutions.

(ii)Diffraction of Mach 5.09 Shock Moving over a 90° Corner

This test case is taken from Quirk (1994) as the Mach 5.09 normal shock moves from left to right. Figs. 10(a)-(b) show the computed density contours at time t=0.25 from the first-order and higher-order accurate RoeVLPA, respectively. The better detailed flow field, including higher shock resolution and sharper contact surface behavior, can be obtained using the higher-order accurate RoeVLPA. Figs. 10(c)-(d) show the computed density contours from the higher-order accurate RoeVLPA again using the Quirk's



1.0

Fig. 12 Comparative computed and exact solutions at time t=0.15for Sod shock tube (RoeVLPA): (a, b) O(1) and O(2) density distributions; (c, d) &(1) and &(2) pressure distributions; and (c, f) $\vartheta(1)$ and $\vartheta(2)$ u-velocity distributions.

pressure switching function with threshold parameters, α , of 15 and 1, respectively. High value of the parameter \alpha prevents adequate dissipation required to suppress oscillation in the vicinity of the strong shock as can be seen on the upper right of Fig. 10(c). The spurious oscillation of the incident shock is eliminated by reducing the parameter α to 1 as shown in Fig. 10(d). The solution contour shown in this figure agrees very well with that obtained by Quirk (1994).

(iii) Oblique Shock Reflection at a Wall

The problem statement of an oblique shock reflection at a wall (Yee et al., 1985) on the domain 1.0×4.0 is presented in Fig. 13. The adaptive remeshing technique described by Phongthanapanich and Dechaumphai (2002) is used to generate adaptive unstructured triangular meshes. The procedure starts by creating a relatively uniform mesh as shown in Fig. 14(a). The fluid analysis is then performed to generate the corresponding solution, such as the density contours, as shown in Fig. 14(b). This flow solution is then used to generate an adaptive mesh to cluster small elements in the regions of sharp changes of the density gradients, and at the same time, to use larger elements on the other regions. The fluid analysis is then performed again to yield a more accurate solution. The entire process is repeated to generate the third adaptive mesh

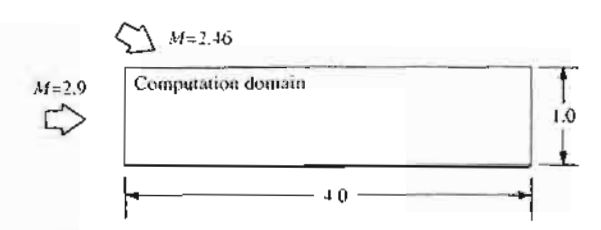


Fig. 13 Problem statement of an oblique shock reflection at a wall

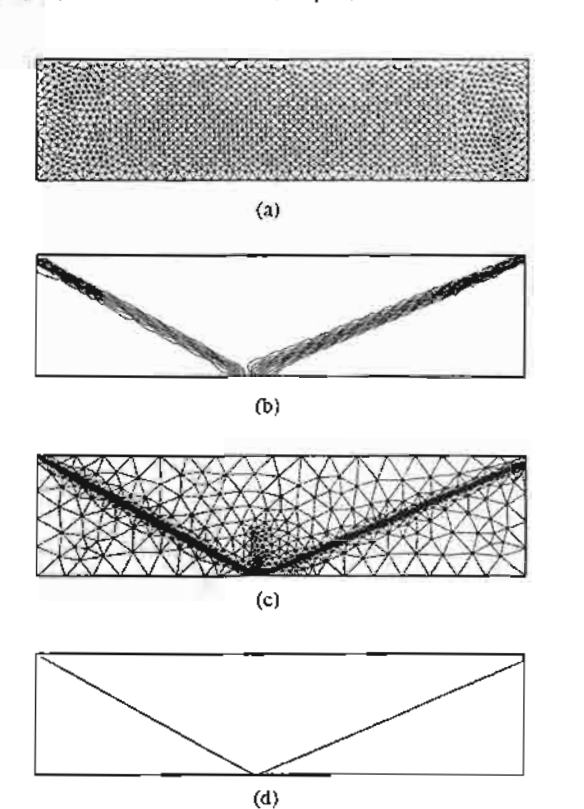


Fig. 14 An oblique shock reflection at a wall: (a)-(b) Initial mesh and the corresponding density contours; and (c)-(d) Third adaptive mesh and the corresponding density contours

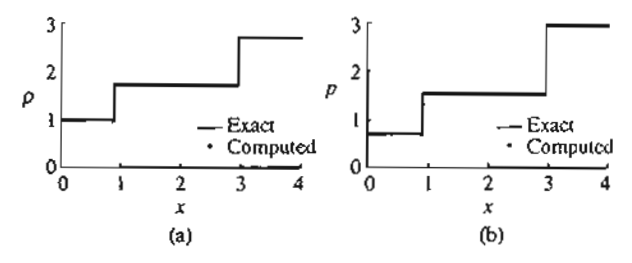


Fig. 15 Comparative solutions of an oblique shock reflection at a wall (\$(2)-RoeVLPA): (a) density distribution; and (b) pressure distribution.

and the corresponding solution as shown in Figs. 14(c)-(d). Figs. 15(a)-(b) show comparative density and pressure distributions between the computed and exact solutions at y=0.5. The figures show the higherorder accurate RoeVLPA can deal with abrupt change of solutions across shocks very well.

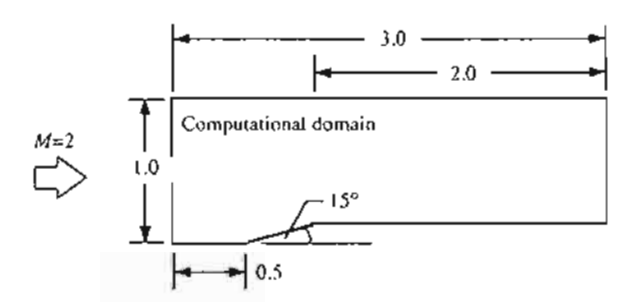


Fig. 16 Problem statement of a Mach 2 flow in a 15° channel

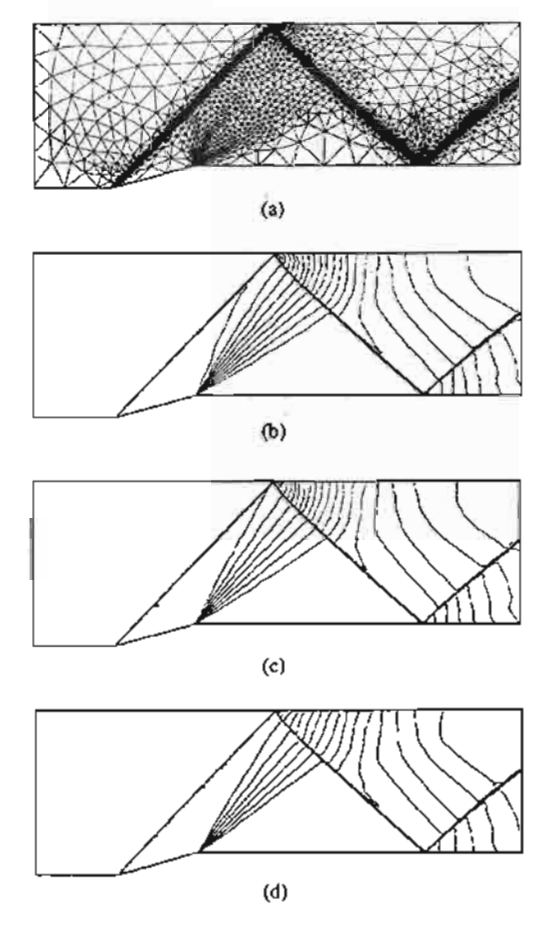


Fig. 17 Mach 2 flow in a 15° channel (£(1)-RoeVLPA): (a) Third adaptive mesh (b) Density contours; (c) Pressure contours; and (d) Mach contours.

(iv) Mach 2 Flow in a 15° Channel

Both the first-order and higher-order Roe's schemes with the proposed entropy fix RoeVLPA are evaluated on unstructured meshes by using the problem of a Mach 2 flow in a 15° channel as presented in Fig. 16. The third adaptive mesh and their corresponding flow solutions computed by using the first-order RoeVLPA such as the density, pressure, and Mach number are shown in Figs. 17(a)-(d), respectively. The analysis of Mach 2 flow in the 15°

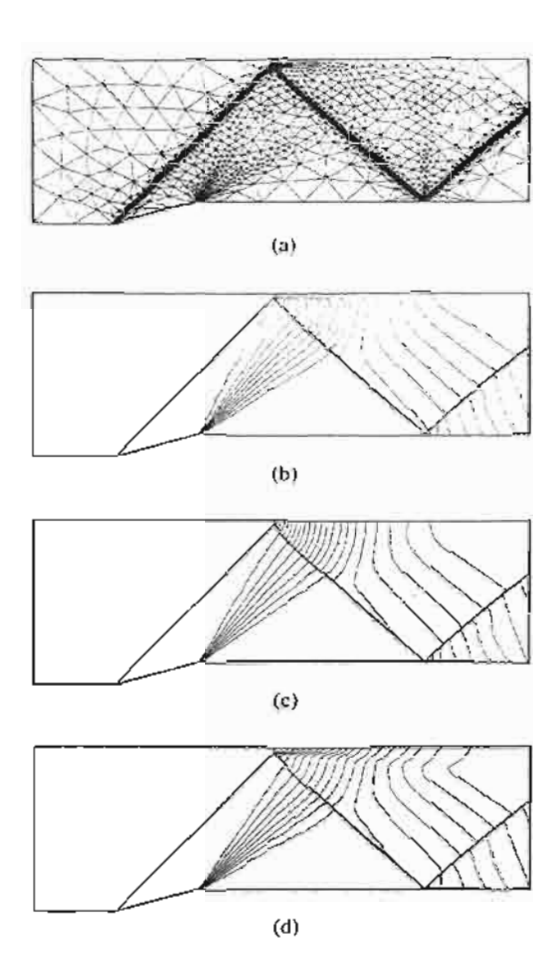


Fig. 18 Mach 2 flow in a 15° channel (#(2)-RoeVLPA): (a) Third adaptive mesh (b) Density contours; (c) Pressure contours; and (d) Mach contours.

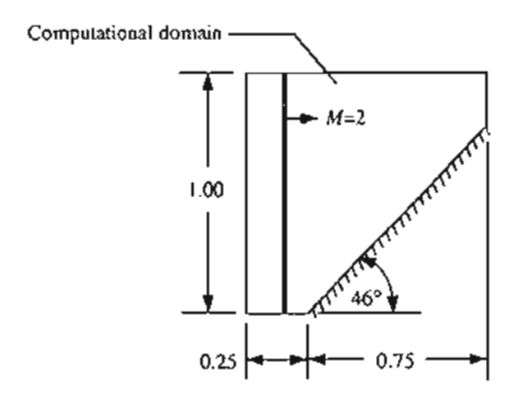


Fig. 19 Problem statement of a Mach 2 shock reflection over a wedge

channel is repeated but with the higher-order RoeVLPA. The third adaptive mesh, and their corresponding solutions are shown in Figs. 18(a)-(d). These figures highlight the capability of the higher-order RoeVLPA to provide more detailed flow behavior, such as the stem generated from the shock impinging on the upper wall, which could not be captured by the first-order RoeVLPA.

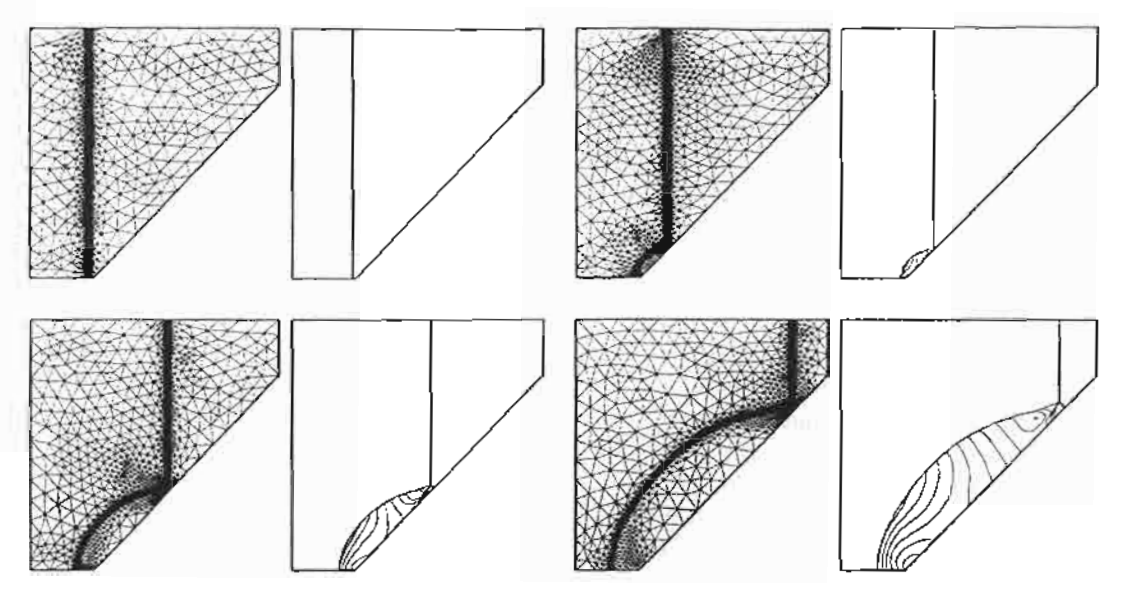


Fig. 20 Transient adaptive meshes and the computed density contours of a Mach 2 shock reflection over a wedge at four different stages of the computation (β(2)-RoeVLPA)

(v) Mach 2 Shock Reflection over a Wedge

The computational domain for a Mach 2 shock reflection over a wedge at 46 degrees (Takayama and Jiang, 1997) is illustrated in Fig. 19. Fig. 20 shows series of transient adaptive meshes and the corresponding computed density contours at different time steps, as the reflection shock starts to form over a wedge. The transient adaptive meshes consist of approximately 20,000 elements in early time before the normal shock reaches the wedge corner, and are increased to approximately 30,000 elements at the bottom right image of Fig. 20. The figures highlight the use of the higher-order accurate RoeVLPA on adaptive meshes to effectively obtain the detailed flow solution.

IV. CONCLUSIONS

A mixed entropy fix method is proposed to improve numerical stability of Roe's flux-difference splitting scheme. The method combines the modified entropy fixes proposed by Van Leer et al. together with the Pandolfi and D'Ambrosio methods. The method was then evaluated by several wellknown test cases and found to eliminate unphysical solutions that may arise from the use of Roe's original scheme. These unphysical solutions include the carbuncle phenomenon on the bow shock of the flow over a blunt body, and the expansion shock generated from the flow over a forward facing step. The switching function suggested by Quirk for identifying the region of the strong shock was investigated. Such a condition was combined with the proposed method in order to avoid the application of a more

dissipative scheme in such a region. This, thus, allows the use of the same entropy fix method for the entire flow domain. To further improve solution accuracy, higher-order spatial and second-order Runge-Kutta temporal discretization were also implemented. The method was also combined with an adaptive mesh generation technique to demonstrate its applicability for arbitrary unstructured meshes. The entire process was found to provide more accurate solutions for both the steady-state and transient flow test cases.

ACKNOWLEDGMENTS

The authors are pleased to acknowledge the Thailand Research Fund for supporting this research work.

NOMENCLATURE

а	speed of sound at the cell interface
e	internal energy
E, G	convection fluxes in x- and y-directions, re-
	spectively.
F	numerical flux vector
h	average mesh size
K	user-specified constant
ñ	unit normal vector
p	pressure ·
q	vector of primitive variables
r_k	right eigenvector
U	vector of conservation variables
V_n	normal velocity
Ω	control volume

threshold parameter

 α

- α_k wave strength of the k^{th} wave
- λ_k eigenvalue
- Ψ_C Vekatakrishnan's limiter function
- φ limiter function
- η numerical dissipation
- y specific heat ratio
- ρ density

REFERENCES

- Dechaumphai, P., and Phongthanapanich, S., 2003, "High-Speed Compressible Flow Solutions by Adaptive Cell-Centered Upwinding Algorithm with Modified H-Correction Entropy Fix," Advances in Engineering Software, Vol. 34, No. 9, pp. 533-538.
- Druguet, M. C., and Zeitoun, D. E., 2003, "Influence of Numerical and Viscous Dissipation on Shock Wave Reflections in Supersonic Steady Flows," Computers and Fluids, Vol. 32, No. 4, pp. 515-533.
- Einfeldt, B., 1988, "On Godunov-Type Methods for Gas Dynamics," SIAM Journal on Numerical Analysis, Vol. 25, No. 2, pp. 294-318.
- Frink, N. T., Parikh, P., and Pirzadeh, S., 1991, "A Fast Upwind Solver for the Euler Equations on Three-Dimensional Unstructured Meshes," Proceedings of the 29th Aerospace Sciences Meeting and Exhibit, Reno, Nevada, AIAA Paper-91-0102.
- Frink, N. T., and Pirzadeh, S. Z., 1998, "Tetrahedral Finite-Volume Solutions to the Navier-Stokes Equations on Complex Configurations," NASA/TM-1998-208961.
- Gressier, J., and Moschetta, J. M., 2000, "Robustness Versus Accuracy in Shock-Wave Computations," International Journal for Numerical Methods in Fluids, Vol. 33, No. 3, pp. 313-332.
- Harten, A., 1983, "High Resolution Schemes for Hyperbolic Conservation Laws," Journal of Computational Physics, Vol. 49, No. 3, pp. 357-393.
- Lin, H. C., 1995, "Dissipation Additions to Flux-Difference Splitting," *Journal of Computational Physics*, Vol. 117, No. 1, pp. 20-27.
- Pandolfi, M., and D'Ambrosio, D., 2001, "Numerical Instabilities in Upwind Methods: Analysis and Cures for the "Carbuncle" Phenomenon," Journal of Computational Physics, Vol. 166, No. 2, pp. 271-301.
- Perry, K. M., and Imlay, S. T., 1988, "Blunt-Body Flow Simulations,", Proceedings of the 24th AIAA, SAE, ASME and ASEE Joint Propulsion Conference, Boston, MA., USA. AIAA Paper-88-2904.
- Phongthanapanich, S., and Dechaumphai, P., 2002, "Underwater Explosion Simulation by Transient Adaptive Delaunay Triangulation Meshing Technique," Royal Thai Navy Technical Report,

- TR-3894. Bangkok.
- Quirk, J. J., 1994, "A Contribution to the Great Riemann Solver Debate," *International Journal* for Numerical Methods in Fluids, Vol. 18, No. 6, pp. 555-574.
- Roe, P. L., 1981, "Approximate Riemann Solvers, Parameter Vectors, and Difference Schemes," Journal of Computational Physics, Vol. 43, No. 2, pp. 357-372.
- Sanders, R., Morano, E., and Druguet, M. C., 1998, "Multidimensional Dissipation for Upwind Schemes: Stability and Applications to Gas Dynamics," *Journal of Computational Physics*, Vol. 145, No. 2, pp. 511-537.
- Shu, C. W., and Osher, S., 1988, "Efficient Implementation of Essentially Non-Oscillatory Shock-Capturing Schemes," Journal of Computational Physics, Vol. 77, No. 2, pp. 439-471.
- Sod, G. A., 1978, "A Survey of Several Finite Difference Methods for Systems of Nonlinear Hyperbolic Conservation Laws," Journal of Computational Physics, Vol. 27, No. 1, pp. 1-31.
- Takayama, K., and Jiang, Z., 1997, "Shock Wave Reflection over Wedges: A Benchmark Test for CFD and Experiments," *Shock Waves*; Vol. 7, No. 4, pp. 191-203.
- Van Albada, G. D., Van Leer, B., and Roberts, W. W., 1982, "A Comparative Study of Computational Methods in Cosmic Gas Dynamics," Astronomy and Astrophysics, Vol. 108, pp. 76-84.
- Van Leer, B., Lee, W. T., and Powell, K. G., 1989, "Sonic-Point Capturing," Proceedings of the 9th Computational Fluid Dynamics Conference, Buffalo, New York, USA, AIAA Paper-89-1945-CP,
- Venkatakrishnan, V., 1995, "Convergence to Steady State Solutions of the Euler Equations on Unstructured Grids with Limiters," *Journal of Computa*tional Physics, Vol. 118, No. 1, pp. 120-130.
- Vijayan, P., and Kallinderis, Y., 1994, "A 3D Finite-Volume Scheme for the Euler Equations on Adaptive Tetrahedral Grids," Journal of Computational Physics, Vol. 113, No. 2, pp. 249-267.
- Woodward, P., and Colella, P., 1984, "The Numerical Simulation of Two-Dimensional Fluid Flow with Strong Shocks," *Journal of Computational Physics*, Vol. 54, No. 1, pp. 115-173.
- Yee, H. C., Warming, R. F., and Harten, A., 1985, "Implicit Total Variation Diminishing (TVD) Schemes for Steady-State Calculations," *Journal* of Computational Physics, Vol. 57, No. 3, pp. 327-360.

Manuscript Received: Oct. 22, 2003 Revision Received: Feb. 26, 2004 and Accepted: Mar. 24, 2004

บทความทางวิชาการ เรื่อง

Fatigue Crack Growth Behavior in Sn-Pb Eutectic Solder/Copper Joint Under Mode I Loading

Published in the

Mechanics of Materials

Vol. 37, pp. 1166-1174

2005



Available online at www.sciencedirect.com





Mechanics of Materials 37 (2005) 1166-1174

www.elsevier.com/locate/mechmat

Fatigue crack growth behavior in Sn-Pb eutectic solder/copper joint under mode I loading

C. Kanchanomai a.*, W. Limtrakarn a, Y. Mutoh b

* Department of Mechanical Engineering, Faculty of Engineering, Thommasat University, Pathumthani 12120, Thailand

b Department of Mechanical Engineering, Nagaoka University of Technology, 1603-1 Kamitomioka, Nagaoka 940-2188, Japan

Received 31 March 2004

Abstract

Fatigue crack growth (FCG) behavior along 63Sn-37Pb solder/copper interface was investigated using a solder-jointed plate specimen with a single-edge crack under opening tensile loading (mode I). Finite element analysis was conducted for evaluating stress intensity factor (K) and J-integral (J) of the crack tip. Under frequency of 10 Hz and stress ratio of 0.1, the fatigue crack propagation rate could be characterized successfully by either stress intensity factor range (ΔK) or J-integral range (ΔJ). A fatigue crack propagated in transgranular manner through Pb-rich phases and Sn-rich phases near the solder-copper interface. With increasing crack length, the size of plastic zone at the crack tip and the von Mises stress along the solder-copper interface increased, which resulted in the interfacial debonding near the crack tip. The critical crack length (a/W) and adhesive strength for interfacial debonding were 0.46 and 20.2 MPa, respectively.

© 2005 Elsevier Ltd. All rights reserved.

Keywords: Fatigue crack growth; Sn-Pb eutectic solder; Solder joint; Solder/copper interface; Adhesive strength

1. Introduction

Eutectic Sn-Pb solders have been widely used for electrical joints because of their low melting points, good wettability, good plasticity, reasonable electrical conductivity (Kang and Sarkhel,

E-mail uddress: kchao@engr.tu.ac.th (C. Kanchanomai).

1994). Due to their low melting temperature, the room temperature corresponds to a high homologous temperature (greater than 0.5). It is known that the time-dependent mechanisms, e.g. grain boundary sliding, cavitation and phase transformation, are possible to occur during fatigue test under high homologous temperature condition. These damage processes lead to premature failure when compared to cyclic-dependent fatigue failure, and life under low cycle fatigue (LCF) is

0167-6636/\$ - see front matter © 2005 Elsevier Ltd. All rights reserved. doi:10.1016/j.mechmat.2005.02.002

^{*} Corresponding author. Tel.: +66 02 564 3001; fax: +66 02 564 3010.

dominated by crack propagation (Kanchanomai et al., 2002a,b). Zhao et al. (2001) reported that the mode I fatigue crack growth (FCG) behavior of bulk Sn-Pb eutectic solder was dominantly cyclic dependence at low stress ratios and high frequencies, while time-dependent behavior became dominant at high stress ratios and low frequencies. For the single Sn-Pb cutectic solder ball lap joint specimens, it was observed that the fatigue life reduced with increasing the cycles of thermal cycling aging (-40 to 125 °C) and the fatigue crack propagated in the Pb-rich region adjacent to the intermetallic layer in the solder material (Pang et al., 2001). Based on the finite element analysis, the stress state of a solder joint in surface mount assemblies was a combination between normal and shear stress states (Liu et al., 1987), which results in the mixed-mode loading condition at the interfacial crack tip even when external loading is pure mode I or pure mode II (Nayeb-Hashemi and Yang, 2001). The proportion of normal and shear stresses at the interfacial crack tip depends on both distances ahead of the crack tip and the elastic mismatches across the interface (Hutchinson et al., 1987; Sou and Hutchinson, 1989; Hutchinson and Sou, 1991).

While extensive work has been carried out on LCF and FCG of bulk Sn-Pb eutectic solder under mode I and mode II loading, very little is known about FCG behavior and mechanism of crack along solder/substrate interface. In the present study, the FCG behavior and mechanisms of crack along 63Sn-37Pb solder/copper interface under mode I loading were investigated and compared with those of bulk Sn-Pb eutectic solder.

2. Specimen and experimental procedures

FCG test under mode I loading was conducted on a solder-jointed plate specimen with a single-edge notch, as shown in Fig. 1. To make a specimen, two copper bars (99.9 wt.%) were jointed together by Sn-Pb eutectic solder (63Sn-37Pb). Before soldering, the copper bars were cleaned in order to remove the oxides according to the following procedure. First, the surfaces of copper bars were lightly polished using 600-grit emery

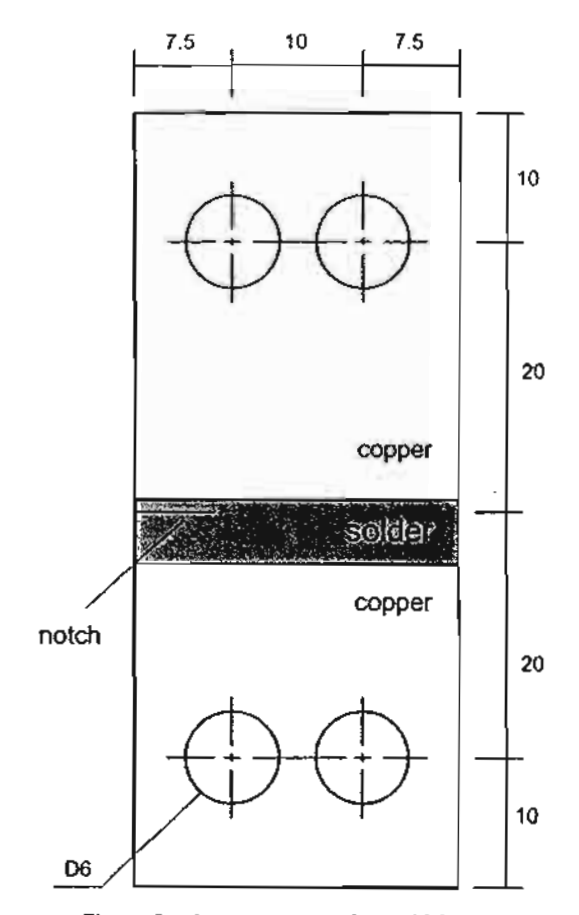


Fig. 1. Specimen geometry (6-mm thickness).

paper, then dipped in a dilute nitric acid solution and rinsed in distilled water. The copper bars were coated with flux (Hakko 89-400, Japan) and placed in a special fixture made from nonsolderable material (aluminum alloy), as shown in Fig. 2. Bulk solder (63Sn-37Pb) was melted and reflowed into cavity between two copper bars. In order to allow the remaining flux to escape, the temperature of fixture and specimen was maintained at 250 °C (above solder reflow temperature) for 10 min before left to cool in air. By using this procedure, specimens can be manufactured with good alignment, a specific solder layer thickness, and a minimal void content. The excess solder was removed by milling and then lightly polished to obtain the geometry, as shown in Fig. 1. The geometry of specimen was designed in accordance with an ASTM recommendation (1998), i.e.

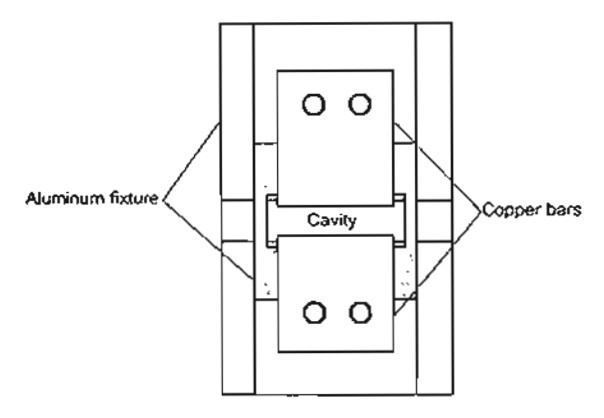


Fig. 2. Specimen reflow fixture.

 $W/20 \le B \le W/4$, where W is the width and B is the thickness. The initial notch was introduced 1 mm far from the copper/solder interface by electrodischarge machining (EDM), and then the precracking (ASTM, 1998) was performed to obtain sharp initial crack $(a_0 = 0.25W)$ before the FCG test.

FCG test was conducted in air at a constant temperature of 25 °C ($T/T_{\rm m} > 0.5$), and a constant relative humidity of 55%. A servo-hydraulic fatigue machine (Instron 8872) with the load sensor capacity of 25 kN has been used in the present study. Cyclic loading was applied sinusoidally under a frequency of 10 Hz, a maximum load of 0.8 kN, and a load ratio of 0.1. Crack length was measured by using a traveling microscope with a precision of 10 μ m. Scanning electron microscopy (SEM) and optical microscope examinations were performed directly on the specimens before and after tests.

3. Finite element analysis

According to the theory of fracture mechanics (Anderson, 1994), stress intensity factor (K) can be defined as the severity of the crack situation of a linear-elastic material as affected by crack size, stress, and geometry. For an interfacial crack under plane strain condition, the stress intensity factors in mode I and II $(K_1 \text{ and } K_{11})$ along the traction ahead of the crack tip $(\theta = 0)$ are simply the real and imaginary parts of a complex stress

intensity factor, whose physical meaning can be understood from the interface traction expressions (Hutchinson et al., 1987; Sou and Hutchinson, 1989):

$$(\sigma_{yy} + i\sigma_{yy})_{n=0} = \frac{(K_1 + iK_{11})r^n}{\sqrt{2\pi r}}$$
 (1)

where, r and θ are polar coordinates centered at the crack tip. The x-axis coincides with the interface, while y-axis is perpendicular to the interface. The linear-elastic singularity solution in the crack tip region can be developed using the bimaterial constant (ε) , defined as:

$$\varepsilon = \frac{1}{2\pi} \ln \frac{1-\beta}{1+\beta} \tag{2}$$

$$\beta = \frac{G_1(k_2 - 1) - G_2(k_1 - 1)}{G_1(k_2 + 1) + G_2(k_1 + 1)}$$
(3)

$$k = 3 - 4v \tag{4}$$

where, β is Dundurs' parameter (Dundurs, 1969), subscripts 1 and 2 refer to materials 1 and 2. G and v are shear modulus of elasticity and Poisson's ratio, respectively.

Considering the low yield strengths of solders, i.e. below 20 MPa, a large plastic zone is possible to form ahead of the crack tip during FCG test. For such a condition, the energy release rate in a nonlinear elastic body that contains a crack, i.e. *J*-integral, can be used to describe crack tip conditions (Rice, 1968). The *J*-integral for an interfacial crack between two dissimilar isotropic materials under plane strain condition (Hutchinson and Sou, 1991), can be determined as follows

$$J = \frac{1 - \beta^2}{E} (K_{\rm t}^2 + K_{\rm II}^2) \tag{5}$$

where

$$\frac{1}{E^*} = \frac{1}{2} \left(\frac{1}{\overline{E}_1} + \frac{1}{\overline{E}_2} \right) \tag{6}$$

$$\overline{E} = \frac{E}{(1 - v^2)} \tag{7}$$

In the present work, finite element analysis (ABAQUS version 6.2-1) based on the interaction integral method (Shih and Asaro, 1988), was used to extract the individual stress intensity factors (K)

and J-integral for a crack along solder/copper interface under plane strain condition. The mechanical properties of 63Sn-37Pb and copper used in the calculation are summarized in Table 1. The two-dimensional finite element model of the specimen (Fig. 3) consists of 2118 plane strain elements and 4,388 degrees of freedom (DOF). The maximum load of 0.8 kN and the stress ratio of 0.1 were used for the finite element analysis. The calculation results are shown in Fig. 4. The stress intensity factors (K) and J-integral increase with increasing crack length (a) in accordance with the basic theory of fracture mechanics (Anderson, 1994). The stress intensity factor range is in a combination between mode I and mode II, however the magnitude of K_I is significantly greater than that of K_{II} , i.e. K_{I} is the dominated fracture parameter for the present FCG test.

Table I Mechanical properties of solder and copper

Mechanical properties	63Sn-37Pb	Copper
Young's modulus (GPa)	32	134
Yielding strength (MPa)	18.1	140
Tensile strength (MPa)	39.7	295
Strain hardening exponent	0.30	-
Poisson's ratio	0.32	0.34

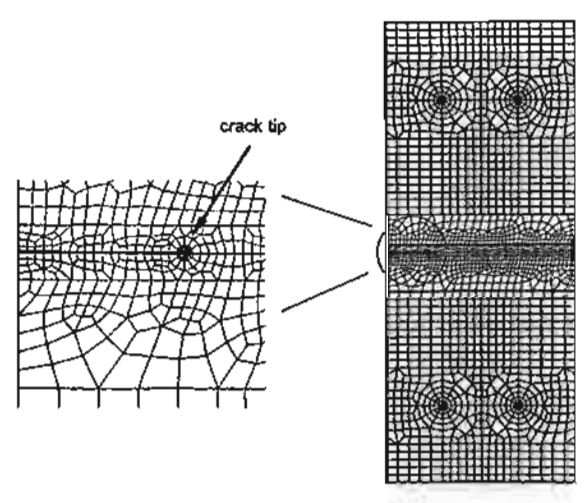
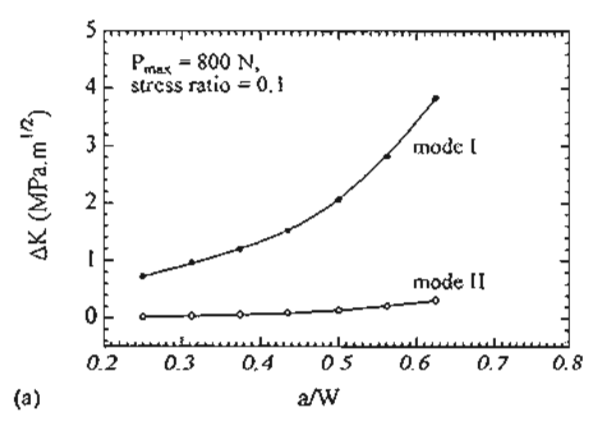


Fig. 3. Finite element mesh.



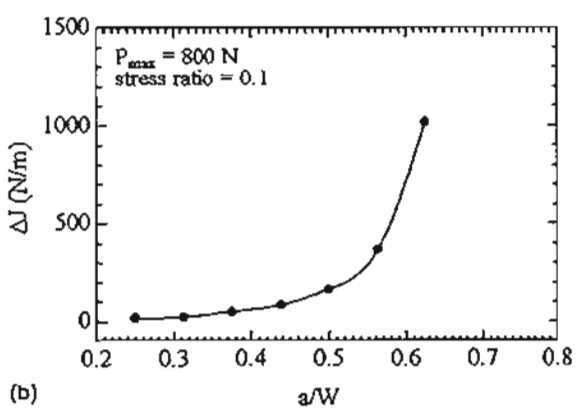


Fig. 4. Relationships between (a) stress intensity factor range and crack length, and (b) J-integral range and crack length.

4. Results and discussion

4.1. Microstructure

SEM micrograph of solder-copper interface is shown in Fig. 5. In the region of Sn-Pb eutectic solder, the microstructure consists of alternating phases of Pb (light) and β-Sn (dark), similar to those observed previously in the solder joints (Morris et al., 1994). Between solder and copper, the intermetallic layer due to the reaction between molten solder and copper surface could be observed. The intermetallic phase is a double layer of Cu₃Sn(ε) on copper substrate and Cu₆Sn₅(η) in contact with molten solder (Morris et al., 1994). Lee and Chen (2002) found that the activation energies of Cu₃Sn and Cu₆Sn₅ growth for 60Sn-40Pb are 59.2 kJmol⁻¹ and 42.25 kJmol⁻¹.

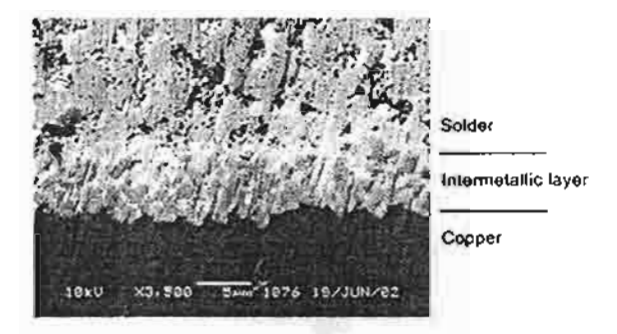


Fig. 5. Microstructures of the bonded interface.

respectively. Due to the lower activation energy, it is likely that the intermetallic layer was mainly the layer of Cu_6Sn_3 intermetallic. As seen from the Fig. 5, the intermetallic layer is about 8 μm in width and has a wavy profile along the interface. It should be noted that the variation of size and profile of intermetallic layer has some effects on adhesive and fatigue strength (Pang et al., 2001; Lee and Chen, 2002).

4.2. Fatigue crack growth curve

Relationship between crack length (a) and crack propagation rate (da/dN) is shown in Fig. 6a. The crack propagation rate increases with increasing crack length. The scattering of the data could be observed when the crack is short and it became less for the longer crack. In order to study the crack closure behavior, relationship between load and load-point displacement is plotted in Fig. 6b. No evidence of crack closure occurred during the FCG test, which is in accordance with the results reported previously by Logsdon et al. (1990).

Generally, if the plastic zone size at the crack tip (ω) is small relative to the local geometry, i.e. the small scale yielding condition $(\omega/a < 0.1)$, the stress intensity factor (K) can be used without significant violation of the linear elastic fracture mechanics (LEFM) principals. For plane strain problem, the plastic zone size at $\theta = 0^{\circ}$ crack plane can be estimated as follows

$$\omega = \frac{1}{3\pi} \left(\frac{K_1}{\sigma_y} \right)^2 \tag{8}$$

where σ_y is the yield stress. From the estimation of the plastic zone size at $\theta = 0^{\circ}$ crack plane, it was

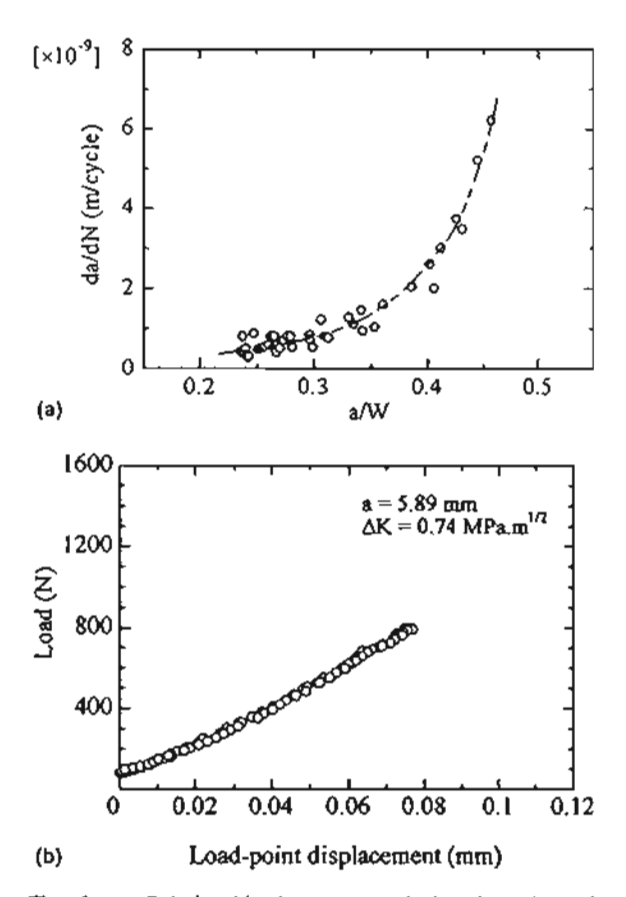


Fig. 6. (a) Relationship between crack length and crack propagation rate, and (b) relationship between load and loadpoint displacement.

found that the ω/a ratio was less than 0.08 in the range of the present experiment. Therefore, the LEFM can be assumed to be valid and K can be used to characterize da/dN. For comparison purpose, the relationship between mode I stress intensity factor range (ΔK_I) and crack propagation rate (da/dN) is plotted in Fig. 7a together with that of bulk 63Sn-37Pb compact-tension specimen under the similar stress ratio and frequency (Zhao et al., 2001). From the figure, it can be seen that the present result correlates well with that of bulk 63Sn-37Pb solder.

However, the small scale yielding condition may not occur for the case of a small crack in actual solder joint. In such elastic-plastic situation, ΔJ should be used as a fracture mechanics parameter instead of ΔK . The possibility of using ΔJ

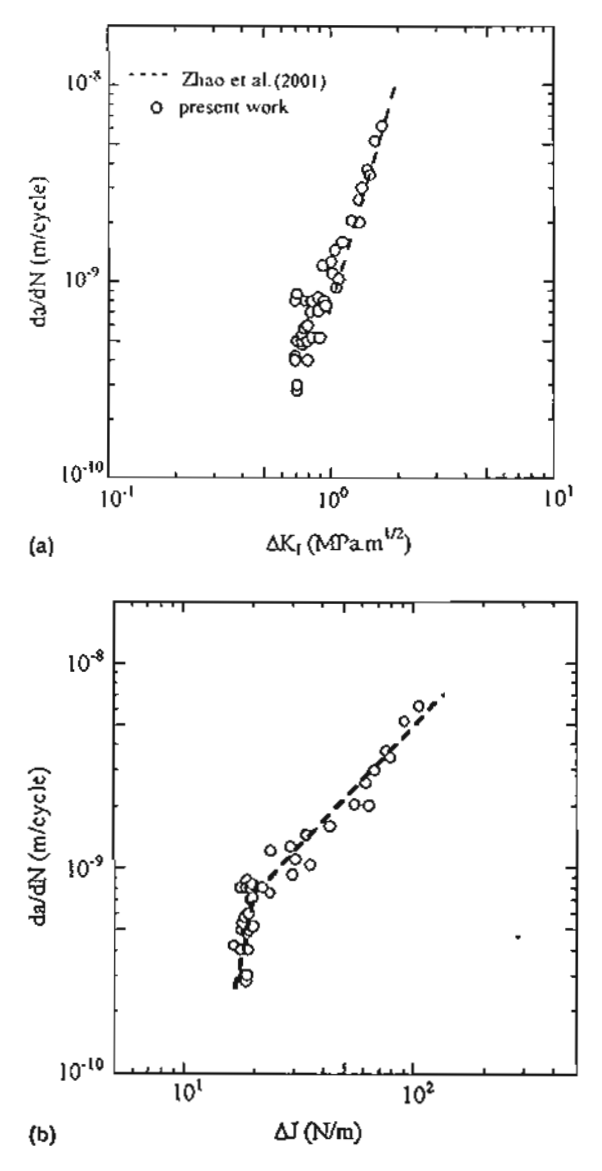


Fig. 7. Relationships between (a) stress intensity factor range and crack propagation rate, and (b) *J*-integral range and crack propagation rate.

to characterize the FCG rate has been investigated and shown in Fig. 7b. It is seen that the data points lie on a double-slope line, which represents two regions: one where a crack grows at very slow rate, and the other where the relationship between ΔJ and $\Delta d/dN$ is linear. As an importance characteristic to assess the resistance of a material to fatigue crack growth, the ΔJ and ΔK that correspond to

the crack growth rate of 10^{-10} m/cycle are defined as $\Delta J_{\rm th}$ and $\Delta K_{\rm th}$, respectively (ASTM, 1998). By extrapolating the present fatigue crack growth curve to lower level, the estimated threshold value of J-integral range ($\Delta J_{\rm th}$) is about 14 N/m, while that of stress intensity factor range ($\Delta K_{\rm th}$) is about 0.6 MPa m^{1/2}, which are in accordance with the results reported earlier by Zhao et al. (2001).

4.3. Fatigue crack path under interaction with interface

A crack initially propagated in the solder parallel to the solder-copper interface and perpendicularly to the load direction. As shown in Fig. 8, the crack propagated in transgranular manner, i.e. through Pb-rich phases (dark) and Sn-rich phases (light). Since the present FCG test was performed under low stress ratio and high frequency condition, it is likely that the manner of propagation is dominated by the cyclic-dependent FCG mechanism, i.e. transgranular manner of propagation (Zhao et al., 2001). Furthermore, the crack path is near the interface, only 1 mm far from it, which is much smaller than specimen width. The copper only elastically deforms in the present experiment, while the solder can plastically deform. Therefore, the region near the crack tip cannot deform freely under the plastic constraint due to copper. It is reasonable that the plane strain

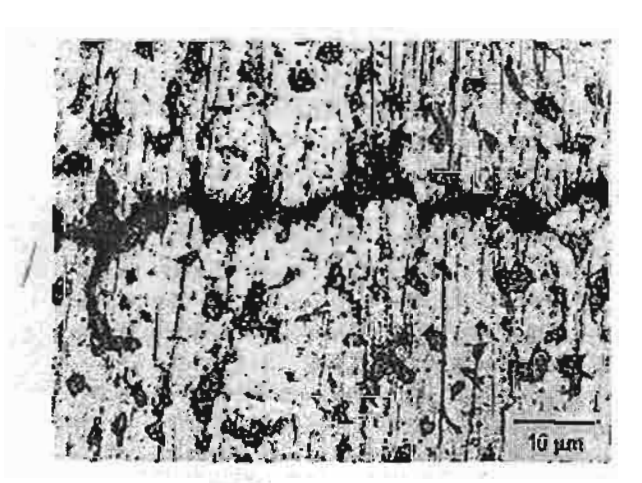


Fig. 8. Crack propagation path: Pb (dark) and β -Sn (light) (loading is in vertical direction).

condition can be assumed for the deformation near the interface of the present joint.

After some amount of crack propagation in the solder, the crack turned to the interface and propagated along the interface, as shown in Fig. 9. In order to investigate this growth phenomenon, the distribution of von Mises stress and strain near the crack tip at the maximum load for various crack lengths was estimated by using finite element analysis, as shown in Fig. 10. The discontinuity and irregular distribution of the stress and strain are mainly due to the difference of elastic modulus and yield strength between solder and copper. According to von Mises criterion, yielding occurs when von Mises stress reaches the uniaxial yield strength. Since the yield strength of the present solder is 18.1 MPa, the arrows in the solder region of Fig. 10a-c indicate the plastic zone. The plastic

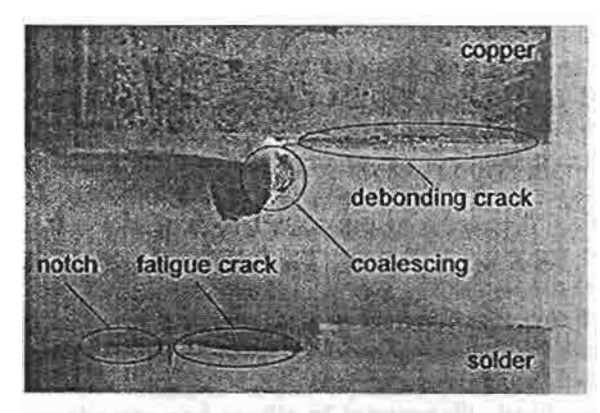


Fig. 9. Micrograph of final failure (loading is in vertical direction).

deformation occurs only in the solder side, as can be seen from Fig. 10f. The distributions of

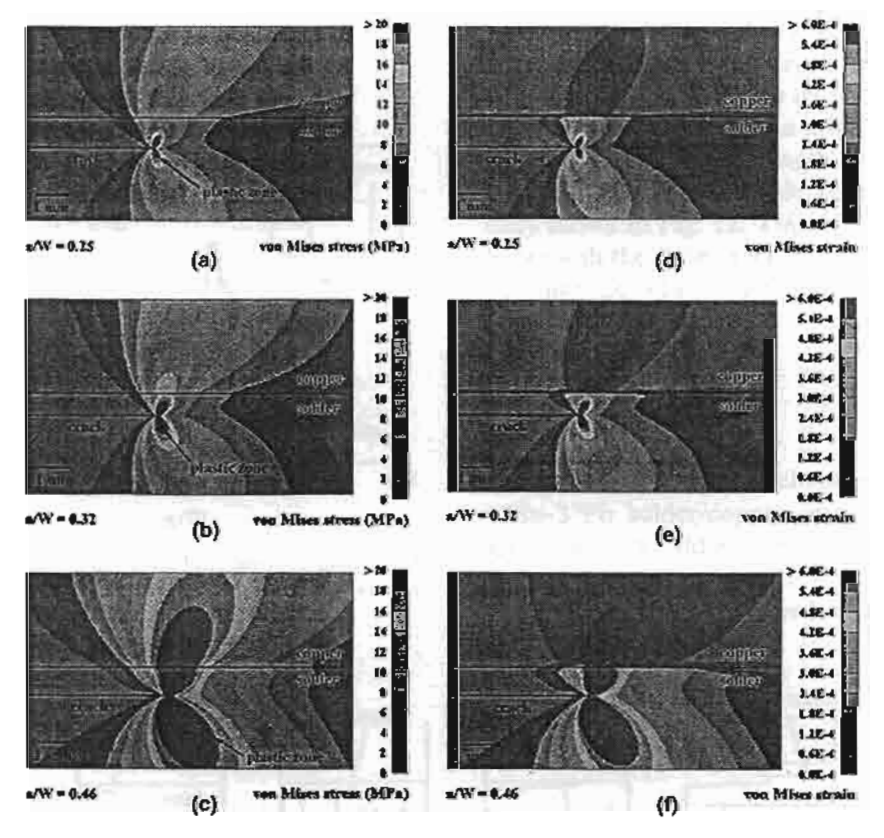


Fig. 10. von Mises stresses of the specimen for various crack lengths (a) a/W = 0.25, (b) a/W = 0.32, and (c) a/W = 0.46, and von Mises strains of the specimen for various crack lengths (d) a/W = 0.25, (e) a/W = 0.32, and (f) a/W = 0.46 (loading is in vertical direction).

von Mises stress and strain along the interface are shown in Fig. 11a and b, respectively. It can be estimated from Fig. 11a that the plastic zone ahead of the crack tip reaches the interface when the crack length is longer than a/W = 0.42. Based on the experimental result, where the interface debonding occurs at the crack length of a/W = 0.46 (critical crack length), the interfacial von Mises

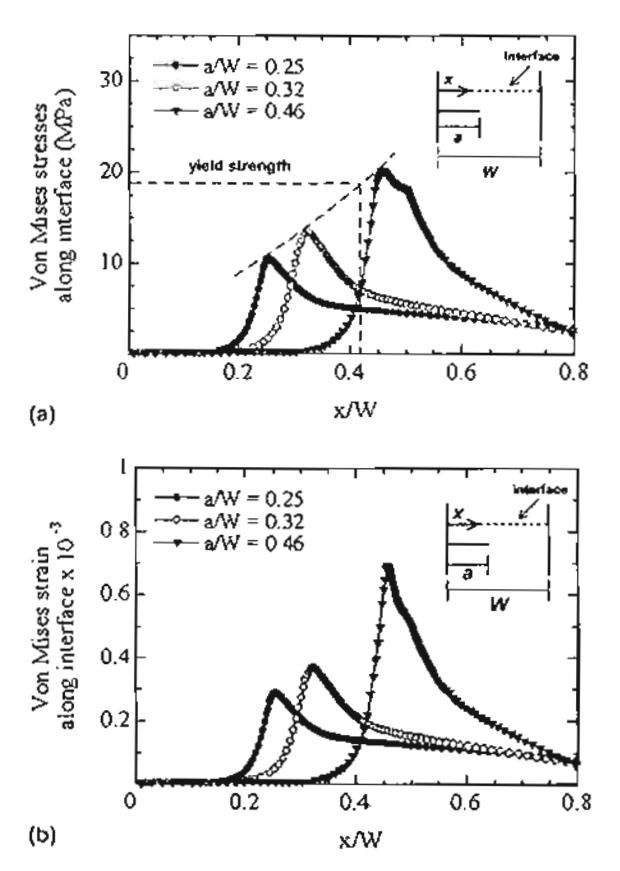


Fig. 11. (a) von Mises stresses along interface for various crack lengths, and (b) von Mises strains along interface for various crack lengths.

stress, i.e. adhesive strength, can be estimated to be 20.2 MPa.

Quan et al. (1987) measured the adhesive strength of 60Sn-40Pb with a cross section of 3.18 × 7.62 mm by tensile test as 82.8 MPa, and became 46.23 MPa after storage at 250 °C for 6 h. Similar reduction in adhesive strength with increasing storage time was reported by Chiou et al. (1995), and Lee and Chen (2002). Since the size and profile of intermetallic band become thicker and rougher with the increasing storage time, it is likely that the adhesive strength depends on the size and profile of intermetallic band, i.e. become weaker with thicker and rougher intermetallic band, and results in the differences of the adhesive strength among literatures.

From the foregoing discussion, the crack growth behavior, where the crack turned to the interface and propagated along the interface after some amount of crack propagation in the solder, can be explained as follows. With increasing crack length, the size of plastic zone and the magnitude of stress near the crack tip increase. Consequently, the plastic zone reaches the interface and the stress exceeds the adhesive strength of interface, which results in the interfacial debonding, as schematically shown in Fig. 12. This debonding crack coalesces with the main crack and forms a crack along the interface, which unstably propagates in a brittle manner.

5. Conclusions

The behavior and mechanisms of FCG along 63Sn-37Pb solder/copper interface were investigated using a solder-jointed plate specimen with a single-edge crack under mode I loading. The main conclusions obtained are summarized as follows:

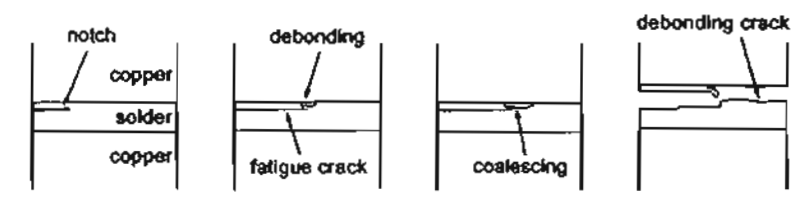


Fig. 12. Schematic of the crack propagation process.

- 1. Crack propagation rate (da/dN) could be characterized successfully by either stress intensity factor range (ΔK) or J-integral range (ΔJ) . The threshold levels $(\Delta K_{th}$ and $\Delta J_{th})$, which represent the resistance of a material to fatigue crack growth, were 0.6 MPa m^{1/2} and 14 N/m, respectively.
- Fatigue crack propagated in the solder parallel
 to the solder-copper interface and perpendicularly to the load direction. The manner of propagation is dominated by the cyclic-dependent
 FCG mechanism, i.e. transgranular manner of
 propagation through Pb-rich phases and Snrich phases.
- 3. With increasing crack length, the size of plastic zone reaches the interface and the stress exceeds the adhesive strength of interface, which results in the interfacial debonding. This debonding crack coalesces with the main crack and forms a crack along the interface, which unstably propagates in a brittle manner. The critical crack length (a/W) and adhesive strength for interfacial debonding were 0.46 and 20.2 MPa, respectively.

Acknowledgments

The authors would like to acknowledge discussions and supports from Dr. P. Dechaumphai, the Thailand Research Fund, the National Research Council of Thailand, and the National Metal and Materials Technology Center (Thailand).

References

- Anderson, T.L., 1994. Fracture Mechanics: Fundamental and Applications, second ed. CRC Press, New York.
- ASTM: E647, 1998. Standard Test Method for Measurement of Fatigue Crack Growth Rates. ASTM standards, The American Society for Testings and Materials. 03.01, pp. 562-598.
- Chiou, B.S., Chang, J.H., Duh, J.G., 1995. Metallurgical reactions at the interface of Sn/Pb solder and electroless copper-plated AiN substrate. IEEE Transaction of Component, Hybrids and Manufacturing Technology—Part B 18 (3), 537-542.

- Dundurs, J., 1969. Mathematical Theory of Dislocations. ASME, New York.
- Hutchinson, J.W., Mear, M.E., Rice, J.R., 1987. Crack paralleling an interface between dissimilar materials. Journal of Applied Mechanics 54, 828-832.
- Hutchinson, J.W., Sou, Z., 1991. Mixed mode cracking in layered materials. Advance of Applied Mechanics 29, 63-191.
- Kanchanomai, C., Miyashita, Y., Mutoh, Y., 2002a. Low cycle fatigue and mechanisms of a eutectic Sn-Pb solder 63Sn/ 37Pb. International Journal of Fatigue 24, 671-683.
- Kanchanomai, C., Miyashita, Y., Mutoh, Y., 2002b. Strainrate effects on low cycle fatigue mechanisms of a eutectic Sn-Pb solder. International Journal of Fatigue 24 (9), 987-993.
- Kang, S.K., Sarkhel, A.K., 1994. Lead (PB)-free solders for electronic packaging. Journal of Electronic Materials 23 (8), 701-708.
- Lee, H., Chen, M., 2002. Influence of intermetallic compounds on the adhesive strength of solder joints. Materials Science and Engineering A 333, 24-34.
- Liu, J.H., Rice, D.W., Avery, P.A., 1987. Elastoplastic analysis of surface-mount solder joints. IEEE Transaction of Component, Hybrids and Manufacturing Technology 10 (3), 346-357.
- Logsdon, W.A., Liaw, P.K., Burke, M.A., 1990. Fracture behavior of 63Sn-37Pb solder. Engineering Fracture Mechanics 36 (2), 183-218.
- Morris Jr., J.W., Freer Goldstein, J.L., Mei, Z., 1994. Microstructural influences on the mechanical properties of solder. In: Frear, D.R. (Ed.), The Mechanics of Solder Alloy Interconnects. Van Nostrand Reinhold, New York, pp. 7-41.
- Nayeb-Hashemi, H., Yang, P., 2001. Mixed mode I/II fracture and fatigue crack growth along 63Sn-37Pb solder/brass interface. International Journal of Fatigue 23, 325-335.
- Pang, H.L.J., Tan, K.H., Shi, X.Q., Wang, Z.P., 2001. Microstructure and intermetallic growth effects on shear and fatigue strength of solder joints subjected to thermal cycling aging. Materials Science and Engineering A 307 (1-2), 42-50.
- Quan, L., Frear, D., Grivas, D., Morris Jr., J.W., 1987. Tensile behavior of Pb-Sn solder/Cu joints. Journal of Electronic Materials 16 (3), 203-208.
- Rice, J.R., 1968. A path independent integral and the approximate analysis of strain concentration by notches and cracks. Journal of Applied Mechanics 35, 379-386.
- Shih, C.F., Asaro, R.J., 1988. Elastic-plastic analysis of cracks on bimaterial interfaces: Part I—Small scale yielding. Journal of Applied Mechanics 55, 299-316.
- Son, Z., Hutchinson, J.W., 1989. Sandwich test specimens for measuring interface crack toughness. Materials Science and Engineering A 107, 135-143.
- Zhao, J., Mutoh, Y., Miyashita, Y., Ogawa, T., McEvily, A.J., 2001. Fatigue crack growth behavior in 63Sn-37Pb and 95Pb-5Sn solder materials. Journal of Electronic Materials 30 (4), 415-421.

บทความทางวิชาการ เรื่อง

Modified Multidimensional Dissipation Scheme on Unstructured Meshes for High-Speed Compressible Flow Analysis

Published in the

International Journal of Computational Fluid Dynamics

Vol. 18, pp. 631-640

2004



Modified Multidimensional Dissipation Scheme on Unstructured Meshes for High-speed Compressible Flow Analysis

S. PHONGTHANAPANICH and P. DECHAUMPHAI*

Mechanical Engineering Department, Chulalongkorn University, Bangkok 10330, Thailand

A Roe's flux-difference splitting scheme, combining with the entropy fix method according to Van Leer et al., and the H-correction entropy fix method by Pandolfi and D'Ambrosio, is proposed. The presented scheme eliminates unphysical flow behaviors such as a spurious bump of the carbuncle phenomenon that occurs on the bow shock from flow over a blunt body, and the expansion shock generated from flow over a forward facing step. The proposed scheme is further extended to obtain high-order spatial and temporal solution accuracy. The scheme is, in addition, combined with an adaptive meshing technique that generates unstructured triangular meshes to resemble the flow phenomena for reducing computational effort. The entire procedure is evaluated by solving several benchmarks as well as complex steady-state and transient high-speed compressible flow problems.

Keywords: Shock instabilities; Carbuncle phenomenon; Roe's FDS; Entropy fix; H-correction

INTRODUCTION

High-speed compressible flows normally involve complex flow phenomena, such as strong shock waves, shock-shock interactions and shear layers. Various numerical inviscid flux formulations have been proposed to solve an approximate Riemann problem. Among these formulations, the flux-difference splitting scheme by Roe (1981) is widely used due to its accuracy, quality and mathematical clarity. However, the scheme may sometimes lead to unphysical flow solutions in certain problems, the carbuncle phenomenon (Perry and Imlay, 1988) with a spurious bump in the bow shock from flow over a blunt body. The scheme could not provide accurate solutions for the complex impinging shock phenomenon yielding kinked Mach stem (Quirk, 1994) generated from a moving shock over a ramp. In the odd-even decoupling problem, an unrealistic perturbation may grow with the planar shock as it moves along the duct. To improve the solution accuracy of these problems, Quirk (1994) pointed out that the original Roe's scheme should be modified in the vicinity of strong shock.

The main objective of this paper is to propose and evaluate a modified Roe's scheme with adaptive unstructured meshes for two-dimensional high-speed compressible flow analysis. The entropy fix method by Van Leer et al. (1989) and the multidimensional dissipation

technique of Pandolfi and D'Ambrosio (2001) are modified for unstructured triangular meshes and implemented into the original Roe's scheme.

The presentation in this paper starts with the describing of some well-known problems, which exhibit the numerical shock instability from the Roe's scheme in the second section. The entropy fix methods of Van Leer et al. (1989); Sanders et al. (1998); Pandolfi and D'Ambrosio (2001) are examined to investigate their capabilities as well as the solution accuracy. The modified Roe's scheme with a mixed entropy fix method is then proposed in the third section. The presented scheme is further extended to high-order solution accuracy and then evaluated by several benchmark test cases in the fourth section. Finally, the scheme with adaptive unstructured meshes is applied for solving both the steady-state and transient highspeed compressible flow problems to demonstrate its performance.

NUMERICAL SHOCK INSTABILITY

Some certain problems for which the Roe's scheme may not provide correct solutions for the compressible Euler computation are presented in this section. Unphysical numerical solutions may arise from the implementation of the one-dimensional upwinding numerical flux

^{*}Corresponding author. TeL/Fax: +66-2-218-6621. E-mail: fmepdc@eng.chula.ac.th

function onto the multidimensional formulation. To avoid such solutions, three entropy fix methods (Van Leer et al., 1989; Sanders et al., 1998; Pandolfi and D'Ambrosio, 2001) have been recently suggested because of their simplicity and convenient code implementation. These entropy fix methods are presented herein and their performances are determined by test cases. All solutions in this section use the Roe's scheme with the first-order accuracy on structured triangular meshes.

Roe's Flux-difference Splitting Scheme with Dissipation

The governing differential equations of the Euler equations for the two-dimensional inviscid flow are given by,

$$\frac{\partial \mathbf{U}}{\partial t} + \frac{\partial \mathbf{E}}{\partial x} + \frac{\partial \mathbf{G}}{\partial y} = 0 \tag{1}$$

where U is the vector of conservation variables, and E and G are the vectors of the convection fluxes in the x and y directions, respectively. The perfect gas equation of state is in the form,

$$p = \rho \, e(\gamma - 1) \tag{2}$$

where p is the pressure, ρ is the density, e is the internal energy and γ is the specific heat ratio.

By integrating Eq. (1) over a control volume, Ω , and applying the divergence theorem to the resulting flux integral,

$$\frac{\partial}{\partial t} \int_{\Omega} \mathbf{U} \, d\Omega + \int_{\partial \Omega} \mathbf{F} \cdot \hat{\mathbf{n}} \, dS = 0 \tag{3}$$

where F is the numerical flux vector and \hat{n} is the unit normal vector of the cell boundary. The numerical flux vector at the cell interface between the left cell L and the right cell R according to Roe's scheme (1981) is,

$$\mathbf{F}_n = \frac{1}{2}(\mathbf{F}_{nL} + \mathbf{F}_{nR}) - \frac{1}{2} \sum_{k=1}^4 \alpha_k |\lambda_k| \mathbf{r}_k \tag{4}$$

where α_k is the wave strength of the k-th wave, λ_k is the eigenvalue and r_k is the corresponding right eigenvector. The eigenvalues in the above Eq. (4) are,

$$\lambda_{k} = \begin{bmatrix} V_{n} - a \\ V_{\kappa} \\ V_{n} \\ V_{n} + a \end{bmatrix}$$
 (5)

where V_n is the normal velocity and a is the speed of sound at the cell interface.

The original Roe's scheme previously described has been found to produce unphysical solutions such as the expansion shock from a flow over a step, and the carbuncle phenomenon of a flow over a blunt body. To avoid such unphysical solutions, the entropy fix methods (Harten, 1983; Van Leer et al., 1989; Lin, 1995; Sanders et al., 1998; Pandolfi and D'Ambrosio, 2001; Dechaumphai and Phongthanapanich, 2003) have been proposed and investigated. The three versions of the entropy fix methods by Van Leer et al., Pandolfi and D'Ambrosio and Sanders et al., are first evaluated for structured meshes herein. These methods are then extended to unstructured meshes and presented later in this paper.

The Van Leer's entropy fix method (RoeVL) is designed to correct the unphysical expansion shock. The one-dimensional entropy fix was developed by replacing the characteristic speeds of the acoustic waves (for k = 1 and 4) with,

$$\left|\lambda_{k}\right|^{*} = \begin{cases} \left|\lambda_{k}\right|_{1} & \left|\lambda_{k}\right| \ge 2\eta^{\text{VL}} \\ \frac{\left|\lambda_{k}\right|^{2}}{4\eta^{\text{VL}}} + \eta^{\text{VL}}, & \left|\lambda_{k}\right| < 2\eta^{\text{VL}} \end{cases}$$
(6)

where

$$\eta^{VL} = \max(\lambda_R - \lambda_L, 0) \tag{7}$$

Sanders et al. introduced an idea of a multidimensional dissipation, the so-called H-correction entropy fix method. The method has shown to eliminate the unrealistic carbuncle phenomenon of the flow over a blunt body in the structured uniform mesh as shown in Fig. 1(a). The advantages of the method are the simplicity in the implementation into the existing scheme and the parameter-free characteristics. For the two triangular cells shown in Fig. 1(b), the H-correction entropy fix according to Sanders et al. (Roes A) has been modified as described by Dechaumphai and Phongthanapanich (2003) to,

$$\eta^{SA} = \max(\eta_1, \eta_2, \eta_3, \eta_4, \eta_5)$$
(8)

where η_i , i = 1, ..., 5 is given as,

$$\eta_l = \frac{1}{2} \max_{k} (|\lambda_{kR} - \lambda_{kL}|) \tag{9}$$

Pandolfi and D'Ambrosio proposed another version of the H-correction entropy fix by excluding η_1 from Eq. (8)

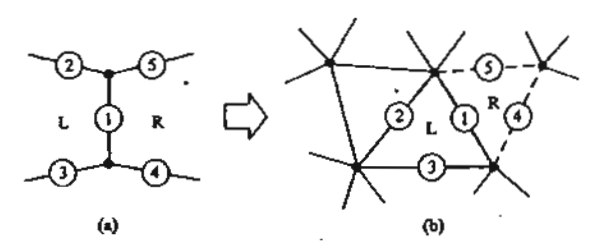


FIGURE 1 Cell interfaces of (a) structured uniform mesh and (b) unstructured triangular mesh.

to avoid an erroneous injection of artificial viscosity, and is applicable only to the entropy and shear waves (for k = 2 and 3). The modified H-correction entropy fix by Pandolfi et al. (RoePA) is,

$$\eta^{PA} = \max(\eta_2, \eta_3, \eta_4, \eta_5)$$
(10)

where η_i , i = 2, ..., 5 is given in Eq. (9).

The above three methods have been evaluated using five test cases involving expansion shocks, the kinked Mach stem, the carbuncle phenomenon and the odd-even decoupling as presented in the following sections.

The Expansion Shocks

To illustrate an unphysical expansion shock, a Mach 3 flow over a forward facing step (Woodward and Colella, 1984) is investigated. The density contours computed from the RoePA, RoeSA and RoeVL are shown in Fig. 2(a)-(c), respectively. The figures show that the RoePA produces an unphysical expansion shock on top of the facing step corner, whereas both the RoeSA and RoeVL provide realistic solutions.

Another expansion shock problem used to evaluate the numerical instability is the diffraction of a Mach 2 shock moving over a 90° corner. Figure 3 shows the computed density contours obtained from the RoeVL. On the other hand, both the RoePA and RoeSA could not provide proper solutions due to negative internal energy that occurs during the computation in the vicinity of the turning corner.

The Kinked Mach Stem

The kinked Mach stem generated from a shock moving over a ramp is another test case used to highlight the performance of these three methods. Figure 4(a)-(c),

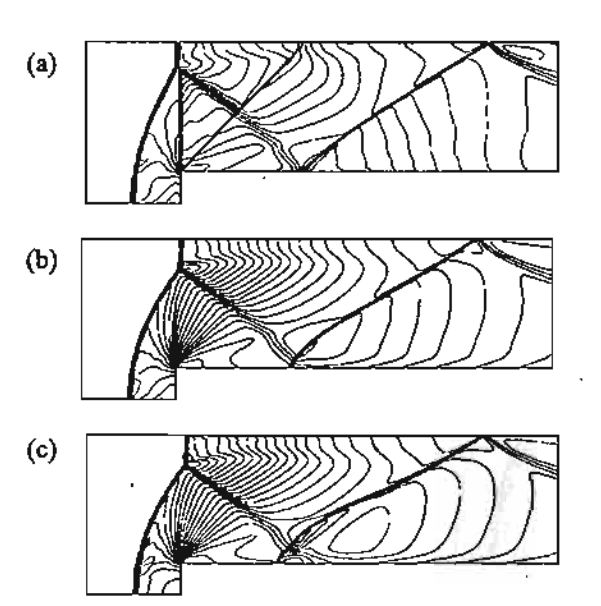


FIGURE 2 Mach 3 flow over a forward facing step; (a) RoePA, (b) RoeSA and (c) RoeVL.

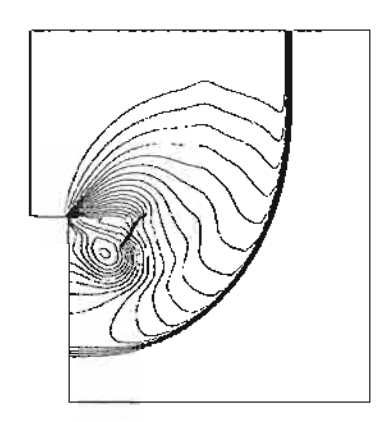
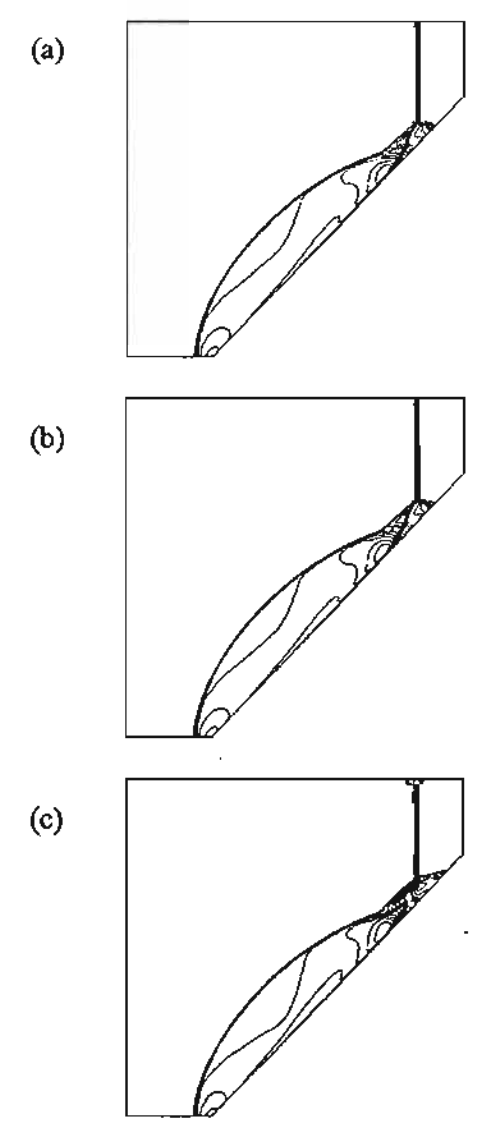


FIGURE 3 Diffraction of a Mach 2 shock over a 90° corner (RoeVL).



PIGURE 4 A kinked Mach stem from a Mach 5 shock moving over a 46° ramp; (a) RoePA, (b) RoeSA and (c) RoeVL.

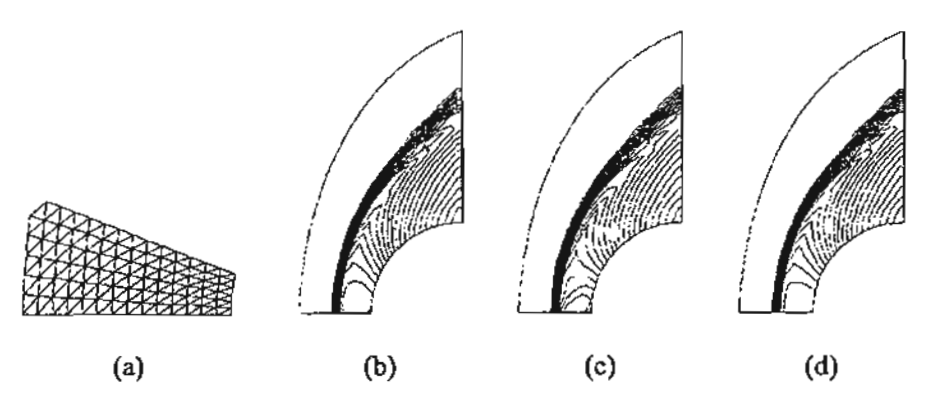


FIGURE 5 Mach 15 flow over a blunt body (first mesh); (a) enlarged view of the mesh, (b) RoePA, (c) RoeSA and (d) RoeVL.

respectively, shows the density contours obtained from the RoePA, RoeSA and RoeVL for a Mach 5 normal shock moving over a 46° ramp. Both the RoePA and RoeSA provide reasonable accurate solutions such that the kinked Mach stem is recovered with the slightly broken-down incident shock. The RoeVL, however, yields the broken-down incident shock with severely kinked Mach stem. Such solution may be caused by insufficient dissipation that cannot counteract the transverse perturbation (Quirk, 1994; Gressier and Moschetta, 2000).

The Carbuncle Phenomenon

The carbuncle phenomenon (Perry and Imlay, 1988) refers to a spurious bump on the bow shock near the flow centerline ahead the blunt body. The phenomenon is highly grid-dependent (Pandolfi and D'Ambrosio, 2001), but does not require a large number of grid points to appear (Gressier and Moschetta, 2000). To demonstrate this grid-dependent phenomenon, the schemes RoePA, RoeSA and RoeVL are employed with three meshes of different element aspect ratios for each scheme. An enlarged view of the elements near the flow centerline of the first mesh and the corresponding density contours are shown in Fig. 5(a)-(d). The carbuncle phenomenon does not appear in any scheme with the use of this relatively crude mesh. The second mesh has more elements which are refined in the circumferential direction as shown in

Fig. 6(a). The RoePA provides realistic flow behavior while the RoeSA and RoeVL exhibit small bump on the bow shock as shown in Fig. 6(b)-(d). The carbuncle phenomenon can be clearly seen in a more refined mesh with higher element aspect ratio as shown in Fig. 7(a). While the RoePA still provides reasonable flow solutions, the carbuncle phenomena are easily observed in the RoeSA and RoeVL as shown in Fig. 7(b)-(d).

The Quirk's Test (Odd-Even Decoupling)

The last test case is a Mach 6 moving shock along the odd-even grid perturbation in a straight duct (Quirk, 1994). The computational domain consists of a uniform triangular mesh with 800 and 20 equal intervals, respectively, along the axial and the transverse directions of the duct. The grids along the duct centerline are perturbed in the transverse direction with a magnitude of ± 10⁻⁶. Both the RoePA and RoeSA can provide accurate shock resolutions whereas the RoeVL suffers from the numerical instabilities as depicted in Fig. 8(a)-(c), respectively. As explained by Gressier and Moschetta (2000), the exact capture of contact discontinuity and strict stability cannot be simultaneously satisfied in any upwind scheme. The solution suggests that additional dissipation injection to the entropy and shear waves is thus needed to stabilize the Roe's scheme as done by RoePA and RoeSA.

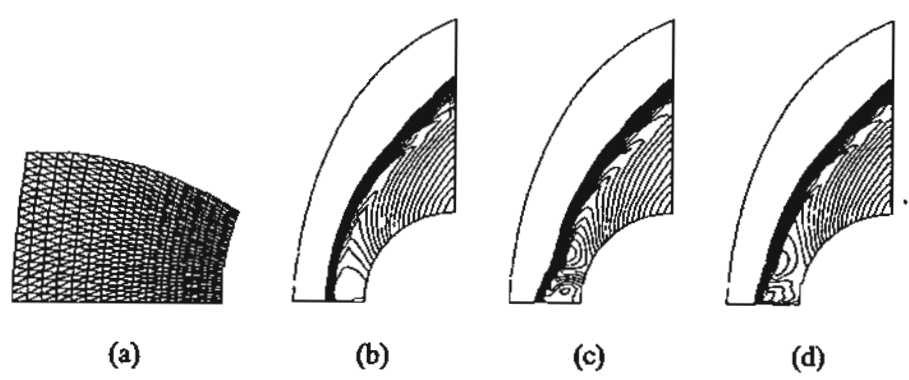


FIGURE 6 Mach 15 flow over a blunt body (second mesh): (a) enlarged view of the mesh, (b) RoePA, (c) RoeSA and (d) RoeVL.

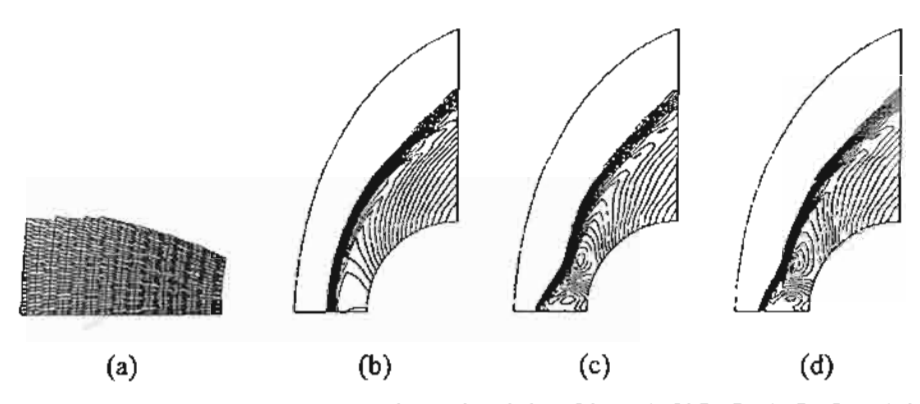


FIGURE 7 Mach 15 flow over a blunt body (third mesh): (a) enlarged view of the mesh, (b) RocPA, (c) RocSA and (d) RocVL

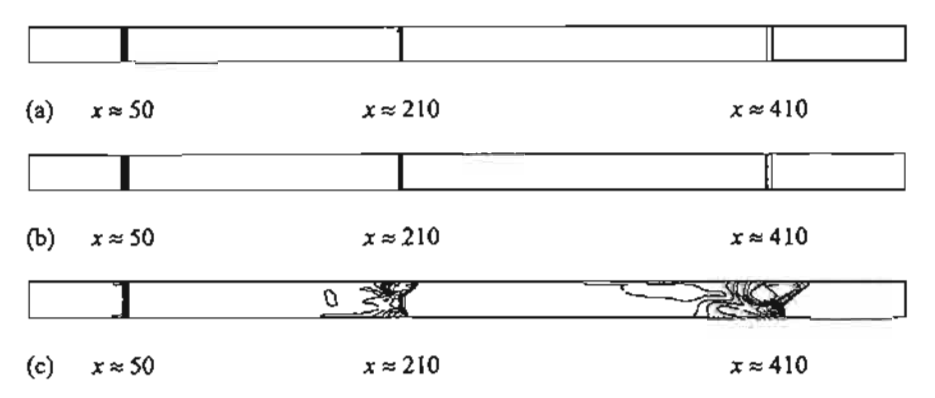


FIGURE 8 Mach 6 moving shock along odd-even grid perturbation: (a) RoePA, (b) RoeSA and (c) RoeVL.

MIXED ENTROPY FIX METHOD FOR ROE'S SCHEME

The flow behaviors obtained from the test cases in the "Numerical shock instability", section using the RoeVL, RoeSA and RocPA schemes which were modified to avoid the numerical shock instability have been studied. The flow over a forward facing step and the diffraction of a shock over 90° comer problems show that RoeVL can perform very well for flows with expansion shock that contain sonic points. Meanwhile, the RoePA is suitable to correct the numerical instability from insufficient dissipation injected to the entropy and shear waves as demonstrated by the kinked Mach stem, the flow over the blunt body, and the moving shock along the odd-even grid perturbation problems. Thus, this paper proposes a mixed entropy fix method (RoeVLPA) that combines the entropy fix method of Van Leer and the modified multidimensional dissipation method by Pandolfi, the modified H-correction, together by replacing the original eigenvalues as follows,

$$|\lambda_k| = \begin{cases} |\lambda_{1,4}|, & |\lambda_{1,4}| \ge 2\eta^{\text{VL}} \\ \frac{|\lambda_{k,4}|^2}{4\eta^{\text{VL}}} + \eta^{\text{VL}}, & |\lambda_{1,4}| < 2\eta^{\text{VL}} \\ \max(|\lambda_{2,3}|, \eta^{\text{PA}}) \end{cases}$$
(11)

where η^{VL} and η^{PA} are defined in Eqs. (7) and (10), respectively.

The mixed entropy fix method (RoeVLPA) is equivalent to the RoeVL in handling the acoustic waves (for k = 1 and 4) and the RoePA for entropy and shear waves (for k = 2 and 3). The efficiency of the mixed entropy fix method is re-evaluated by solving the five test cases presented in Figs. (2)—(8).

For the Mach 3 flows past over a forward facing step, the mixed entropy fix method (RoeVLPA) eliminates the unrealistic expansion shock as shown in the computed density contours in Fig. 9. Figure 10 shows the computed density contours for the diffraction of a Mach 2 shock moving over a 90° corner. Figure 11 depicts the computed density contours of a shock moving over a ramp and clearly shows the recovered kinked Mach stem and the preserved incident shock. The computed density

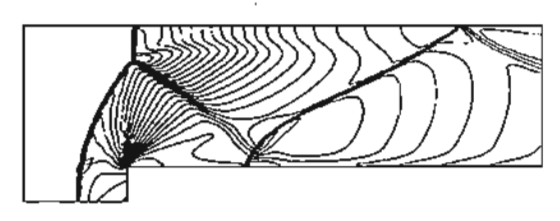


FIGURE 9 The Mach 3 flow over a forward facing step (RocVLPA).

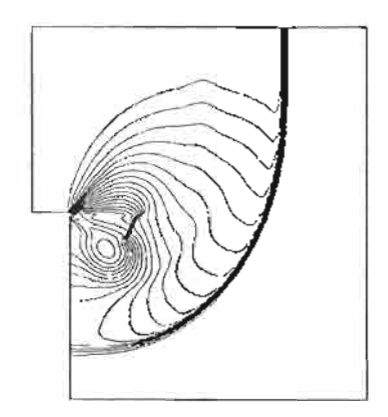


FIGURE 10. The diffraction of a Mach 2 shock over a 90° corner (RoeVLPA).

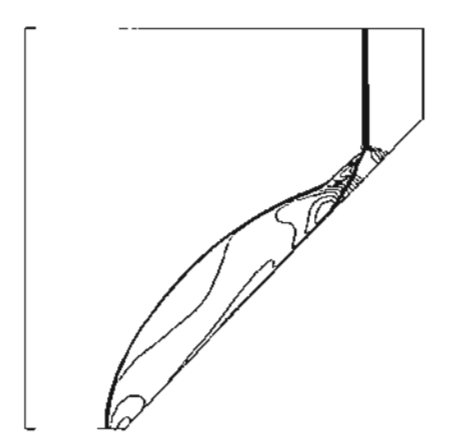


FIGURE 11 The kinked Mach stem from a Mach 5 shock moving over a 46° ramp (RocVLPA).

contours of the Mach 15 flow over a blunt body for the three meshes with different element aspect ratios are shown in Fig. 12 without the unphysical carbuncle phenomenon. Finally, for the test case of the Mach 6

moving shock along the odd-even grid perturbation in which the RoeVL yields unstable shock solution, the proposed RoeVLPA can capture the shock accurately without perturbation growth with time as shown in Fig. 13.

HIGH-ORDER EXTENSION AND APPLICATION ON UNSTRUCTURED TRIANGULAR MESHES

High-order Reconstruction and Limiter

Solution accuracy from the first-order formulation described in the preceding sections can be improved by implementing a high-order formulation for both the space and time. A high-order spatial discretization is achieved by applying the Taylor's series expansion to the cell-centered solution for each cell face (Frink et al., 1991). For instance, the solutions at the midpoint of an element edge between nodes 1 and 2, shown in Fig. 14, can be reconstructed from,

$$q_{f_{1-2}} = q_C + \frac{\Psi_C}{3} \left[\frac{(q_1 + q_2)}{2} - q_3 \right]$$
 (12)

where $\mathbf{q} = [P \quad u \quad v \quad P]^T$ consists the primitive variables of the density, the velocity components and the pressure, respectively; \mathbf{q}_C is the solution at the element centroid; \mathbf{q}_n , n = 1, 2, 3 are the solutions at nodes. In this paper, the inverse-distance weighting from the centroid to the nodes that preserves the principle of positivity (Frink and Pirzadeh, 1998) is used,

$$q_n = \frac{\sum_{i=1}^{N} \frac{q_{C,i}}{|\vec{r}_i|}}{\sum_{i=1}^{N} \frac{1}{|\vec{r}_i|}}$$
(13)

where \mathbf{q}_{CJ} are the surrounding cell-centered values of node n. $|\vec{\mathbf{r}}_{i}|$ is the distance from the centroid to the node n, and N is the number of the surrounding cells.

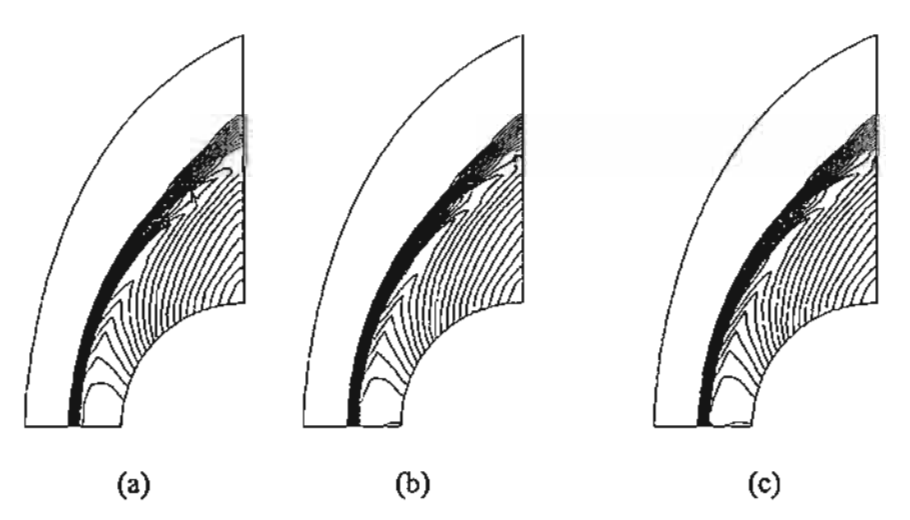


FIGURE 12 The Mach 15 flow over a blunt body (RoeVLPA): (a) first grid. (b) second grid and (c) third grid.

HIGH-SPEED COMPRESSIBLE FLOW ANALYSIS

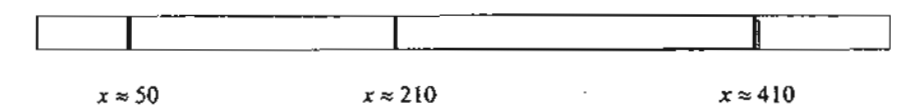


FIGURE 13 The Mach 6 moving shock along odd-even grid perturbation (RoeVLPA).

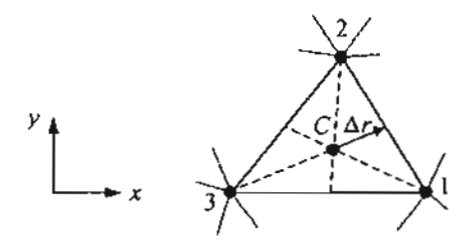


FIGURE 14 Linear reconstruction on a typical triangular element.

The $\Psi_{\rm C}$, in Eq. (12), represents the limiter, preventing spurious oscillation that may occur in the region of high gradients. In this study, Vekatakrishnan's (1995) limiter function is selected,

$$\Psi_{C} = \min_{i=1,2,3} \begin{cases} \phi\left(\frac{\Delta_{+,\text{min}}}{\Delta_{-}}\right), & \Delta_{-} \geq 0 \\ \phi\left(\frac{\Delta_{+,\text{min}}}{\Delta_{-}}\right), & \Delta_{-} < 0 \\ 1, & \Delta_{-} = 0 \end{cases}$$
 (14)

where $\Delta_{-} = \mathbf{q}_c - \mathbf{q}_i$, $\Delta_{+,\max} = \mathbf{q}_{\max} - \mathbf{q}_i$ and $\Delta_{+,\min} = \mathbf{q}_{\min} - \mathbf{q}_i$. The \mathbf{q}_{\max} and \mathbf{q}_{\min} are, respectively, the maximum and minimum values of all distance-one neighboring cells. The function ϕ is similar

to the Van Albada limiter (Van Albada et al., 1982), which is expressed in the form,

$$\phi(y) = \frac{y^2 + 2y}{y^2 + y + 2}.$$
 (15)

Second-order Temporal Discretization

The second-order temporal accuracy is achieved by implementing the second-order accurate Runge-Kutta time stepping method (Shu and Osher, 1988),

$$\mathbf{U}_{i}^{*} = \mathbf{U}_{i}^{n} - \frac{\Delta t}{\Omega_{i}} \sum_{j=1}^{3} \mathbf{F}^{n} \cdot \mathbf{n}_{j}$$

$$\mathbf{U}_{i}^{n+1} = \frac{1}{2} \left[\mathbf{U}_{i}^{0} + \mathbf{U}_{i}^{*} - \frac{\Delta t}{\Omega_{i}} \sum_{j=1}^{3} \mathbf{F}^{*} \cdot \mathbf{n}_{j} \right]$$
(16)

where Δt is the time step. Local element time steps are used for steady-state analysis, while the minimum global time step based on spectral radii (Vijayan and Kallinderis, 1994) is used for the unsteady analysis to reduce the computation effort.

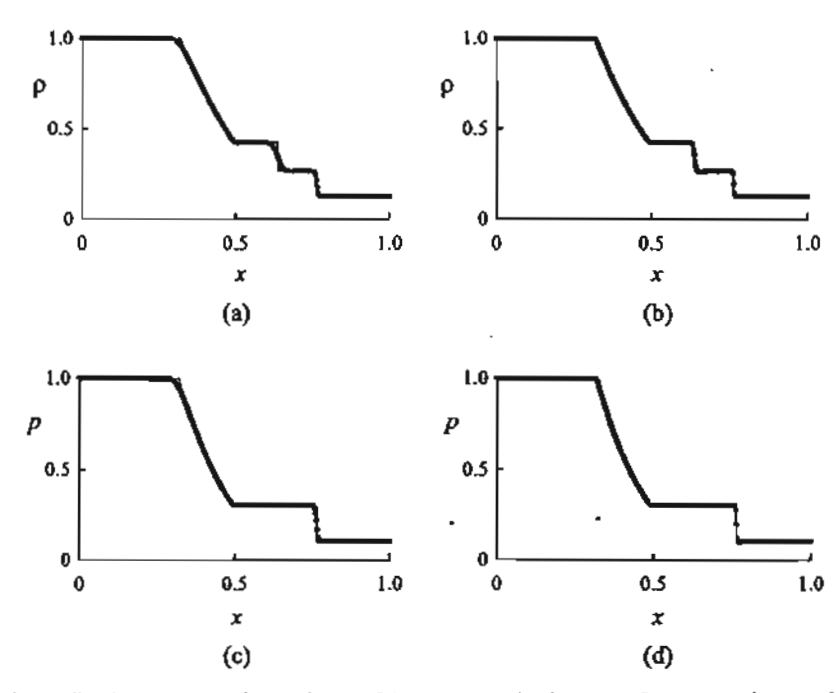


FIGURE 15 Comparative predicted and exact solutions at time t = 0.15 for Sod shock tube (RoeVLPA): (a), (b) $\vartheta(1)$ and $\vartheta(2)$ density distributions; (c), (d) $\vartheta(1)$ and $\vartheta(2)$ pressure distributions.

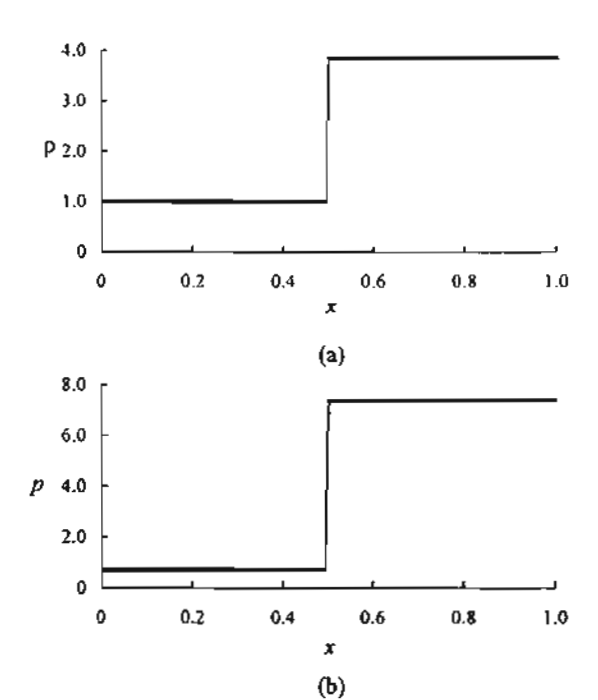


FIGURE 16 Computed solutions of the stationary normal shock at 500 iterations ($\theta(2)$ -RoeVLPA): (a) density distribution and (b) pressure distribution.

Numerical Evaluation

The high-order extension of the Roe's scheme with the mixed entropy fix method, RoeVLPA, presented in the preceding section is evaluated by solving several problems. The modified scheme is also combined with an adaptive meshing technique that generates unstructured triangular meshes for more complex problems. These selected test cases are: (1) Sod shock tube, (2) Stationary normal shock, (3) Diffraction of Mach 5.09 shock over a 90° corner and (4) Mach 3 flow in a convergent—divergent channel.

Sod Shock Tube

The one-dimensional shock tube test case, the so called Sod shock tube (Sod, 1978), is solved by using

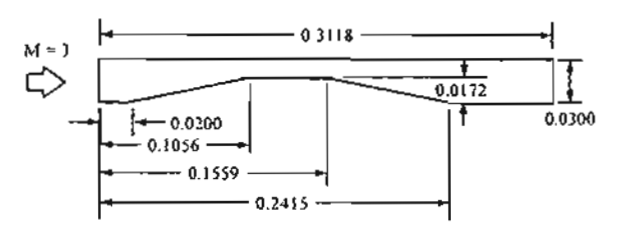


FIGURE 18 Problem statement of a Mach 3 flow in a convergent-divergent channel.

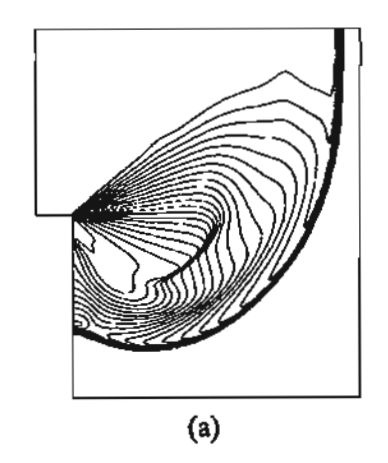
a two-dimensional domain. The initial conditions of the fluids on the left and right sides are given by $(\rho, u, p)_L = (1.0, 0.0, 1.0)$ and $(\rho, u, p)_R = (0.125, 0.0, 0.1)$. The 1.0×0.1 computational domain is discretized with uniform triangular elements into 400 and 40 equal intervals in the x and y directions, respectively. Figure 15(a)-(d) shows the predicted density and pressure distributions along the tube length and is compared with the exact solutions at time t = 0.15. The figure shows that the high-order extension of Roe's scheme with the entropy fix Roe VLPA provides more accurate solutions than the first-order solutions.

Stationary Normal Shock

The normal shock of Mach 3 (Kim et al., 2001) is used as another test case for the proposed high-order accurate RoeVLPA. The initial conditions are given by $(\rho, u, \rho)_L = (1.0, 3.0, 0.714)$ and $(\rho, u, \rho)_R = (3.857, 0.778, 7.381)$. After computation with 500 iterations with the Courant number of 0.5, the high-order accurate RoeVLPA predicts the density and pressure distributions as shown in Fig. 16. The figure shows that the normal shock is captured by approximately three intermediate points.

Diffraction of Mach 5.09 Shock Moving over a 90° Corner

This test case is taken from Quirk (1994) as Mach 5.09 normal shock is moving from left to right. Figure 17(a),(b) shows the computed density contours at



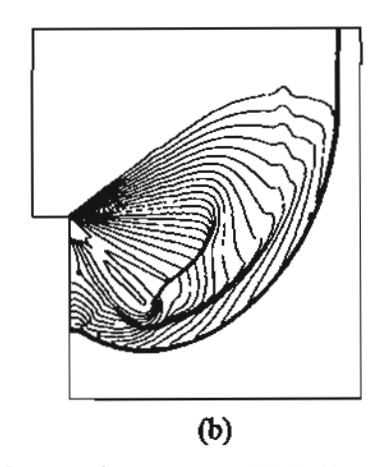


FIGURE 17 Density contours of a diffraction of Mach 5.09 shock over a 90° corner at time t = 0.25: (a) ϑ (1)-RoeVLPA and (b) ϑ (2)-RoeVLPA

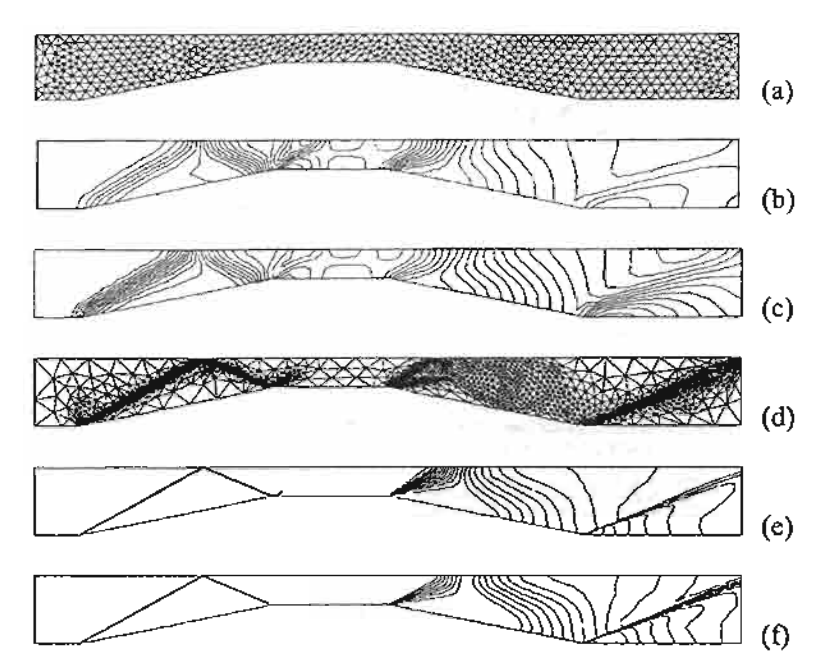


FIGURE 19 Mach 3 flow in a convergent-divergent channel ($\vartheta(1)$ -RoeVLPA): (a) initial mesh; (d) third adaptive mesh; (b), (e) density contours; (c), (f) Mach contours.

time t = 0.25 from the first-order and high-order accurate RoeVLPA, respectively. The high-order accurate RoeVLPA can better capture detailed flow field, including higher shock resolution and sharper contact surface behavior.

Mach 3 Flow in a Convergent-Divergent Channel

Both the first and high-order RoeVLPA are further evaluated for adaptive unstructured meshes using a problem with more complex flow phenomena. Figure 18

shows the problem statement of a Mach 3 flow in a convergent-divergent channel, which results in complex flow behavior involving incident and reflecting shocks with expansion waves. The first-order RoeVLPA is combined with the adaptive mesh generation technique for capturing detailed flow behavior as presented in Fig. 19(a)-(f). The entire procedure is then repeated with the use of the high-order RoeVLPA. The adaptive meshes and their corresponding solutions are shown in Fig. 20(a)-(f). This figure highlights the use

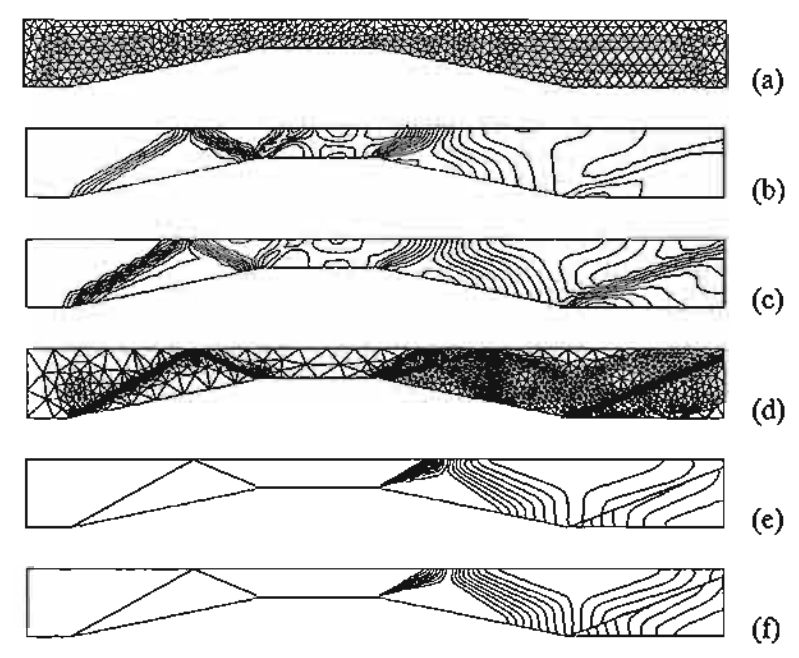


FIGURE 20 Mach 3 flow in a convergent-divergent channel ($\vartheta(2)$ -RoeVLPA): (a) initial mesh; (d) third adaptive mesh; (b), (e) density contours; (c), (f) Mach contours.

of the high-order accurate scheme on adaptive meshes to effectively obtain detailed flow solutions.

CONCLUSION

A mixed entropy fix method is proposed to improve numerical stability of the Roe's flux-difference splitting scheme. The method combines the modified entropy fixes by Van Leer et al. and Pandolfi and D'Ambrosio, together. The method was then evaluated by several well-known test cases and found to eliminate unphysical solutions that may arise from the use of the original Roe's scheme. These unphysical solutions include the carbuncle phenomenon on the bow shock of the flow over a blunt body, and the expansion shock generated from the flow over a forward facing step, etc. To further improve solution accuracy, the high-order spatial and second-order Runge-Kutta temporal discretization were also implemented. The method was also combined with anadaptive mesh generation technique to demonstrate its applicability for arbitrary unstructured meshes. The entire process was found to provide more accurate solutions for both the steady-state and transient flow test cases.

Acknowledgements

The authors are pleased to acknowledge the Thailand Research Fund for supporting this research work.

References

- Dechaumphai, P. and Phongthanapanich, S. (2003) "High-speed compressible flow solutions by adaptive cell-centered upwinding algorithm with modified H-correction entropy fix", Adv. Eng. Software. 32, 533-538.
- Frink, N.T. and Pirzadeh, S.Z. (1998). "Tetrahedral finite-volume solutions to the Navier-Stokes equations on complex configurations", NASA/TM 1998 208961.

- Frink, N.T., Parikh, P. and Pirzadeh, S. (1991). "A fast upwind solver for the Euler equations on three-dimensional unstructured meshes," AIAA Paper-91-0102, AIAA, 29th Aerospace Sciences Meeting and Exhibit, Reno, Nevada.
- Gressier, J. and Moschetta, J.M. (2000) "Robustness versus accuracy in shock-wave computations", Int. J. Numer. Meth. Fluids 33, 313-332.
- Harten, A. (1983) "High resolution schemes for hyperbolic conservation laws", J. Comp. Phys. 49, 357-393.
- Kim, K.H., Kim, C. and Rho, O.H. (2001) "Methods for the accurate computations of hypersonic flows", J. Comp. Phys. 174, 38-80.
- Lin, H C. (1995) "Dissipation additions to flux-difference splitting", J. Comp. Phys. 117, 20-27.
- Pandolfi, M. and D'Ambrosio, D. (2001) "Numerical instabilities in upwind methods: analysis and cures for the "carbuncle" phenomenon", J. Comp. Phys. 166, 271~301.
- Perry, K.M. and Imlay, S.T. (1988) "Blunt-body flow simulations", AIAA Paper-88-2904, 24th AIAA, SAE, ASME and ASEE Joint Propulsion Conference, Boston, MA.
- Quirk, J.J. (1994) "A contribution to the Great Riemann Solver Debate", Int. J. Numer. Methods Fluids 18, 555-574.
- Roe, P.L. (1981) "Approximate Riemann solvers, parameter vectors, and difference schemes", J. Comp. Phys. 43, 357-372.
- Sanders, R., Morano, E. and Druguet, M.C. (1998) "Multidimensional dissipation for upwind schemes: stability and applications to gas dynamics", J. Comp. Phys. 145, 511-537.
- Shu, C.W. and Osher, S. (1988) "Efficient implementation of essentially non-oscillatory shock-capturing schemes", J. Comp. Phys. 77, 439-471.
- Sod, G.A. (1978) "A survey of several finite difference methods for systems of nonlinear hyperbolic conservation laws", J. Comp. Phys. 27, 1-31.
- Van Albada, G.D., Van Leer, B. and Roberts, W.W. (1982) "A comparative study of computational methods in cosmic gas dynamics", Astron. Astrophys. 108, 76-84.
- Van Leer, B., Lee, W.T. and Powell, K.G. (1989) "Sonic-point capturing", AIAA Paper-89-1945-CP, AIAA, 9th Computational Fluid Dynamics Conference, Buffalo, NY.
- Vekatakrishnan, V. (1995) "Convergence to steady state solutions of the Euler equations on unstructured grids with limiters", J. Comp. Phys. 118, 120-130.
- Vijayan, P. and Kallinderis, Y. (1994) "A 3D finite-volume scheme for the Euler equations on adaptive tetrahedral grids", J. Comp. Phys. 113, 249-267.
- Woodward, P. and Colella, P. (1984) "The numerical simulation of twodimensional fluid flow with strong shocks", J. Comp. Phys. 54, 115-173.

บทความทางวิชาการ เรื่อง

Application of a Multiobjective Optimization to Risk-Based Inservice Testing

Published in the

Journal of Pressure Vessel Technology

Vol. 127, pp. 13-19

2005

Juksanee Virulsri¹

e-mail: juksanee.v@chuta.ac.th Department of Mechanical Engineering, Chulalongkorn University, Bangkok 10330, Thailand

> Shinsuke Sakai Satoshi Izumi Atsushi Iwasaki

Department of Mechanical Engineering, The University of Tokyo, Tokyo 113-8656, Japan

Application of a Multiobjective Optimization to Risk-Based Inservice Testing

This paper proposes a methodology for applying a multiobjective optimization to risk-based inservice testing with robustness. The multiobjective optimization is applied to solve the tradeoff between maintenance costs and unavailability of a standby system and then assist in determining the robust solution. In order to obtain the most robust solution, a decision-making method for the multiobjective optimization in the viewpoint of robustness is proposed. The risk ranking and revising risk-ranking processes are then used to assist in finding the most optimal surveillance test interval based on risk management. The applicability of the proposed methodology is confirmed by case studies for a standby system of a simplified high-pressure injection system in a nuclear power plant's pressurized water reactor. The results showed that the proposed methodology provides an effective scheme to achieve the most optimal surveillance test interval based on risk and robustness. [DOI: 10.1115/1.1845451]

Keywords: Risk-Based Inservice Testing, Multiobjective Optimization, Surveillance Test Interval, Unavailability, Maintenance Costs, Probabilistic Risk Analysis

1 Introduction

For a standby system in the maintenance of nuclear power plants, a surveillance test [1] is performed to detect hidden failures and to assure that the component is still promptly operate when the system is needed. When the standby system does not operate properly, severe damage to plant may occur. Therefore, the surveillance test is important. The surveillance test policy consists of several parameters such as unavailability, maintenance costs, and surveillance test interval. The unavailability is probability that the system or component does not operate expected function when it is required. Therefore, low unavailability is required for the maintenance activities. On the other hand, reduction of the maintenance costs is also needed from the economical viewpoint. From the literature reviews it is apparent that single-objective optimization is widely used in probabilistic risk analysis (PRA) for nuclear power plants; unavailability is considered an objective and cost function is considered an implicit constraint, or vice versa [2-4]. Nevertheless, an obvious tradeoff (conflicting scenarios) exists among these purposes. Consequently the multiobjective optimization [5] is required to solve such tradeoff problems. The results of the multiobjective optimization usually consist of a number of nondominated optimal solutions that are called Paretooptimal solutions.

Furthermore, one of the important parameters for the surveillance test is the surveillance test interval, which will be adopted as the decision variable for the optimization process. In the surveillance test, the system components have been grouped into different test strategies. All components in the same group are determined as the same surveillance test interval. Therefore, the management of the surveillance test interval groups is also significant for improving the maintenance activities. So, only the multiobjective optimization may not lead to the satisfactory results in the risk management point of view. In order to manage the most satisfactorily surveillance test interval groups in the viewpoint of risk, the optimization including prioritization of maintenance should be treated.

The risk-based maintenance (R&M) is the method for determining the priority of the maintenance using components risk. Hence, the RBM can be applied for managing the surveillance test interval groups. There are several guidelines [6,7] that are developed about risk-based maintenance and many researches [8-11] have shown that the RBM has been efficiently applied in maintenance activities. For components in the standby system, such as pumps and valves, risk-based maintenance for testing is called as risk-based inservice testing [12,13]. However, the methodology for updating multiobjective optimization by risk-based inservice testing has not been reported.

The purpose of this paper is to propose a methodology to determine the robust surveillance test with the most optimal surveillance test interval based on risk based inservice testing. The methodology for applying a multiobjective optimization to risk-based inservice testing is proposed in the following section to determine the most optimal test interval based on risk consideration. In order to obtain the robust solution, the decision-making for the multi-objective optimization in the viewpoint of robustness is then proposed.

Finally, the proposed methodology is applied to a standby system of a simplified high-pressure injection system (HPIS) of a nuclear power plant's pressurized water reactor (PWR). It is confirmed that proposed method gives the satisfactory results in view of RBM.

2 The Proposed Methodology

In this section, the methodology for applying the multiobjective optimization to risk-based inservice testing having robustness is proposed.

The proposed methodology is illustrated in Fig. 1. At first, the methodology begins with the definition of the standby system. The inventory of the system is performed to determine unavailability parameters, cost parameters of each component, and initial inservice testing groups of system components. After that, the multiobjective optimization is performed for the initial inservice

¹To whom correspondence should be addressed.

Contributed by the Pressure Vessels and Piping Division for publication in the JOURNAL OF PRESSURE VESSEL TECHNOLOGY. Manuscript received by the PVP Division September 3, 2004; revision received September 30, 2004. Review conducted by: S. Zastrik.

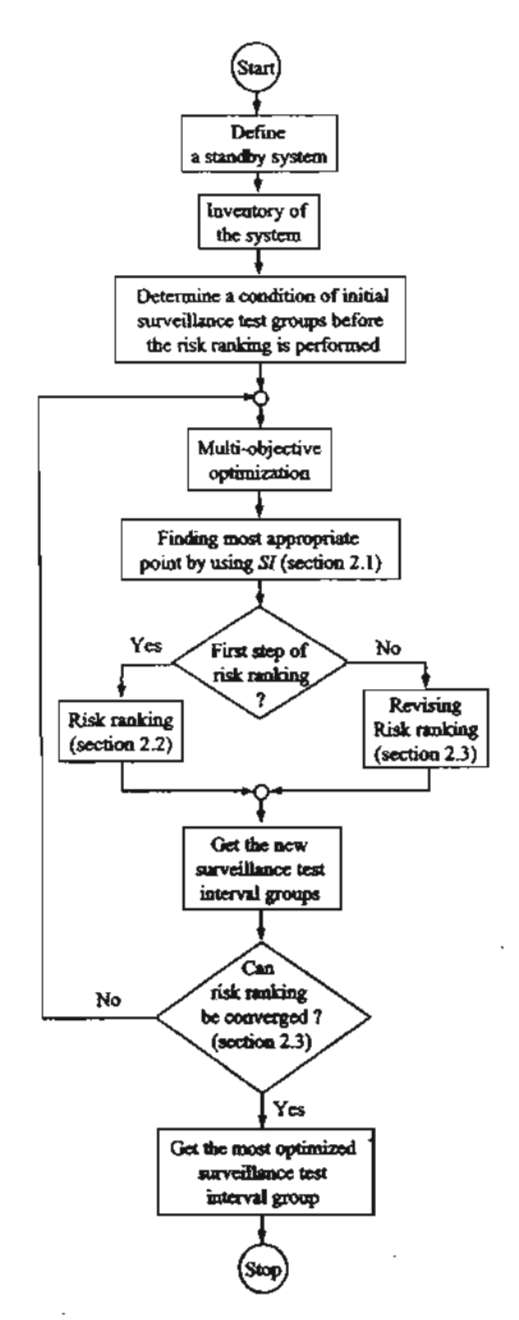


Fig. 1 Process of the methodology for applying the multiobjective optimization to risk-based inservice testing

testing groups of components. This paper considered system unavailability and maintenance costs as a simultaneous multiobjective optimization.

Because the Pareto-optimal solutions consist of a number of solutions, a solution that has lowest sensitivity is selected as the representative solution of the Pareto-optimal solutions. This point is specified as the point where proposed sensitivity index (SI)=1. The detail of SI is shown in Sec. 2.1. Then, the selected solution is used to construct the proposed risk matrix.

The risk matrix assists in categorizing the risk significance of the components into first approximation of test interval groups. Thereafter, the revision of risk ranking is performed to update the multiobjective optimization result.

The revision of the risk ranking and the multiobjective optimization are repeated to improve the multiobjective optimization results until the test interval groups are converged. By this updating process, the optimal surveillance test interval groups based on

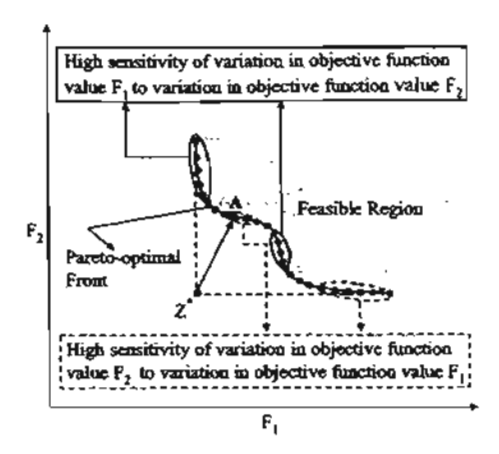


Fig. 2 The typical Pareto-optimal solutions in minimization of objective functions F_1 and F_2

risk consideration are obtained and satisfactorily Pareto-optimal solutions in the viewpoint of risk management are achieved.

2.1 Decision Making for the Multiobjective Optimization Because the Pareto-optimal solutions consist of a number of solutions, the decision making must be done for the multiobjective optimization in order to select the point to be improved.

The conventional method called global criteria [5] is widely used for the decision making on the Pareto-optimal solutions. By using this method, the one solution among the Pareto-optimal solutions that is closest to a given reference point (ideal point) is selected. The ideal point is denoted as the point of the lower bound of all objective functions in the feasible region. For a two-objective minimization problem, the ideal point is typically represented as Z^* in Fig. 2.

However, in the robust point of view, the decision making by the conventional method may not be appropriate. For example, point A in Fig. 2 is the solution that has minimum distance from the given ideal point. Nevertheless, this solution is located in a high sensitivity zone, where objective function value F_2 is highly sensitive to variations in objective function F_1 values. In this case, the decision made by the conventional method does not have the robustness in the view of sensitivity.

Therefore, the sensitivity of the solution should be considered in order to determine the solution that is robust. The sensitivity of the solution on the Pareto-optimal curve is expressed by the proposed SI, defined by the following dimensionless expression:

$$SI = \frac{\Delta F_j / \overline{F_j}}{\Delta F_k / \overline{F_k}} \tag{1}$$

where ΔF_i and ΔF_k are the variation around specified objective function values $\overline{F_i}$ and $\overline{F_k}$ on the Pareto-optimal curve.

The basic idea of this proposed sensitivity index is that when SI=1, the variation ratios of each objective function are almost same and the solution at this point has the lowest sensitivity for both objectives.

2.2 The Proposed Risk Matrix. The concept of risk usually consists of the likelihood of the failure and the consequence of the failure for the interested part. In the standby system, the unavailability is a very important parameter. Therefore, this research corresponds the likelihood of the failure to the unavailability of each component.

In addition, the consequence of a component's failure to the system unavailability is defined in reference of the concept of importance measure of the risk achievement worth (RAW) [14]. The RAW is defined as the following equation:

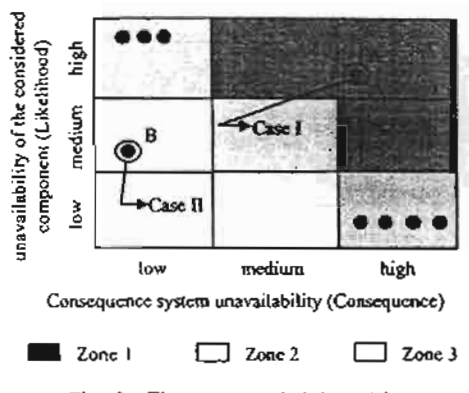


Fig. 3 The proposed risk matrix

$$RAW = \frac{U(U_i = 1)}{U(base)}$$
 (2)

where $U(U_i=1)$ is the increased system unavailability level when the considered component i is assumed to fail or unavailability of that component equals 1.0. U(base) is the present system unavailability level.

In this research, in order to make the parameters used in the proposed risk matrix easy to assist in examining how the risk level is improved quantitatively, the consequence of a component's failure to the system unavailability is corresponded as $U(U_i=1)$.

Both the consequence of each component to the system and the present unavailability of each component are considered on the risk matrix simultaneously.

The likelihood and the consequence are then plotted on the risk matrix. Maximum values and minimum values of the likelihood and consequence from all components are used to define the upper and lower bound of the ranges of the risk matrix. Each axis of risk matrix is equally divided into three categories, such as low, medium, and high. Thereafter, the risk significance for surveillance test is considered as shown in Fig. 3.

In Fig. 3, the risk significance is categorized into three zones, which are corresponding to surveillance test interval T^1 , T^2 , and T^3 . The T^1 , T^2 , T^3 are selected as the design variables in the optimal process. T^1 represents the shortest test interval, T^2 represents the medium one, and T^3 represents the longest one.

The risk significance for each divided zone is categorized as follows.

- (1) Zone 1: The components that locate in this zone are the highest risk significance components. Therefore, these components should be tested most frequently. The surveillance test interval for the components in this zone is determined as T^1 , which is the shortest one allocated in this paper. This zone is considered as an unacceptable zone for the operation.
- (2) Zone 2: The components that locate in this zone are the medium risk significance components. The surveillance test interval for the components in this zone is determined as T^2 , which is the medium test interval allocated in this paper. This zone is considered as an acceptable zone for the operation.
- (3) Zone 3: The components that locate in this zone are the lowest risk significance components. The surveillance test interval for the components in this zone is determined as T^3 , which is the longest one allocated in this paper. This zone is considered as an acceptable zone for the operation.
- 2.3 Revision of the Risk Matrix. Since only one of risk ranking process is not sufficient to find the most optimal groups for surveillance test intervals, the revision of the risk matrix is then required.

In order to revise the risk ranking, the risk matrix (for the solution of the latest obtained test interval groups) is created

again. After that, the interested components to be revised in the test interval groups are treated according to the following two cases.

- (1) Case I: The components, which are still located in zone I even after the treatment, are considered as the highest risk significant components. An example of the components to be revised as the case I is shown as the component A in Fig. 3. These components will be revised by shortening the test interval.
- (2) Case II: The components, which are still located in zone 3, are considered as components that can be further disregarded in the maintenance activities. An example of the components to be revised as the case II is shown as the component B in Fig. 3. These components will be revised by extending the test interval.

The objective of revising the risk ranking is to improve the risk significance of components until they are converged at the optimal test interval groups based on risk consideration, whose risk significances should fall into the medium risk significance finally. The medium risk significance that is shown in zone 2 is not too conservative and not too risks significance.

3 Formulation of Maintenance Activities

In order to optimize the surveillance test, both system unavailability and maintenance costs are treated as simultaneous objectives in this paper. The formulations of these objective functions are taken from the model developed by Martorell et al. [2]. A summary of the models is shown later.

3.1 Unavailability Function. The system unavailability model in the PRA is usually shown as

$$U(x) \approx \sum_{j} \prod_{k} u_{jk}(T) \tag{3}$$

where $u_{jk}(T)$ is the unavailability at the basic event k of the minimal cut set (MCS) j. T is the surveillance test interval. The unavailability model of $u_{jk}(T)$ in Eq. (3) can be expressed as

$$u_{jk}(T) = u_r(T) + u_t(T) + u_c(T)$$
 (4)

where $u_r(T) = \rho + 1/2 \cdot \lambda \cdot T$ is the average unavailability due to random failures, while ρ is a perdemand failure probability and λ is the standby failure rate. $u_r(T) = t/T$ is the unavailability due to testing, while t is the mean downtime due to testing. $u_c(T) = 1/T(\rho + \lambda \cdot T) \cdot d$ is the unavailability due to corrective maintenance, while d is the mean downtime due to corrective maintenance.

3.2 Cost Function. The maintenance cost model can be defined as

$$C(T) = \sum_{i} c_{i}(T) \tag{5}$$

where i is the index of each component.

The cost model of each component can be expressed as

$$c(T) = c_i(T) + c_c(T) \tag{6}$$

where $c_l(T) = t/T \cdot c_{ht}$ is the yearly cost contribution as a consequence of the number of tests being performed over a year period, while c_{ht} represents the hourly costs for testing. In turn, $c_c(T) = 1/T(\rho + \lambda \cdot T) \cdot d \cdot c_{hc}$ is the yearly cost contribution as a consequence of performing corrective maintenance, and c_{hc} is the hourly costs of corrective maintenance.

4 Simulation Method

The multiobjective optimization is used when there are conflicting objectives in the problem. Many classical methods have been used to solve multiobjective optimization problems; these include the weighted sum method [5] and the e-constraint method [5]. Most of the classical methods start with one random predicted solution. From that point, the algorithm is explored to search for a

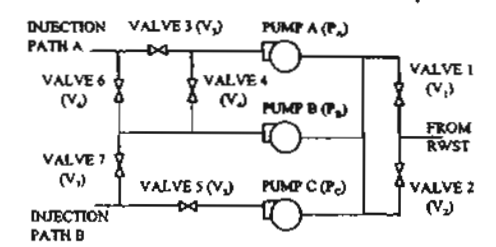


Fig. 4 A standby simplified HPIS

direction to locate a better solution. The process is repeated for a number of times to obtain the best optimum solution. These classical algorithms must be iterated many times to obtain a different solution from the Pareto-optimal solution set. Moreover, some of the classical methods are not efficient in nondifferentiable, discontinuous problems or in nonconvex Pareto-optimal regions. Multi-objective optimization using a genetic algorithm (GA), however, can diminish these problems. Because genetic algorithms work with a population of solutions, it is advantageous to obtain the Pareto-optimal solutions in a single simulation run. GA enables us to give equal emphasis to all nondominated solutions in the population and to simultaneously maintain a diverse set of multiple nondominated solutions.

4.1 Multiobjective Optimization Method Using GA. In this paper, the elitist nondominated sorting genetic algorithm or NSGA-II by Deb [5] has been chosen to solve the multiobjective optimization. The NSGA-II is a multiobjective optimization using genetic algorithm, which has the advantage of a crowding comparison procedure acting as an explicit diversity-preserving mechanism.

4.2 Case Study. A case of a standby-simplified HPIS of a nuclear power plant's PWR modeled by Harunuzzaman and Aldemir [15], which is shown in Fig. 4, is examined in this study.

This system is normally in standby mode. Under accidental conditions, the HPIS can be used to remove heat from the reactor when the steam generators are unavailable. The unavailability of related component and cost data for maintaining the system are summarized from Harunuzzaman and Aldemir [15] and shown in Table 1.

In order to investigate the effectiveness of the proposed methodology, four cases of simulation were investigated. The four investigated cases of initial test interval groups before performing the risk-based inservice testing to the HPIS are shown in Table 2. The symbols used in Table 2 are shown in Fig. 4. T^1 , T^2 , T^3 in Table 2 are the surveillance test intervals, which are already described in Sec. 2.2. The T^1 , T^2 , T^3 are constrained by the following equations:

short test interval
$$(T^1) \leq 8760 \text{ h}$$

medium test interval
$$(T^2 = kl \cdot T^1)$$
 while $1 \le kl \le 10$ (7)

long test interval $(T^3 = k2 \cdot T^2)$ while $1 \le k2 \le 10$

Consequently, the maintenance activities optimization of this system has decision variables set as shown in Eq. (8):

$$T = \{T^{\dagger}, ki, k2\} \tag{8}$$

Table 1 Component unavailability and maintenance cost parameters

Unit	λ (10 ⁻⁶ /h)	ρ (10 ⁻³)	(h)	d (h)	cы (\$/h)	c _{hc} (\$/h)
Valves (V) Pumps (P)	5.83	1.82	0.75	2.6	20	15
	3.89	0.53	4	24	20	15

Table 2 The investigated cases of initial test interval groups before performing the risk-based inservice testing

Case	T ¹	T ²	τ,
1 2	All components V_1, V_2, P_a, P_b, P_c	$v_3, v_4, v_5, v_6,$	
3	v_1	V_1, P_a, P_b, P_e	V_{3}, V_{4}, V_{5}
4	$V_1, V_2, V_3, V_4, V_5, V_6, V_7$	P_o , P_b . P_c	V ₆ , V ₁

4.3 GA Parameters. By using data in Table 1, the objective functions of the unavailability function and cost function can be derived. To formulate the unavailability objective function, a fault tree diagram has been developed to determine the MCSs. Thereafter, NSGA-II is simulated for solving the multiobjective optimization using the parameters shown in Table 3.

5 Results and Discussions

5.1 Discussion of the Proposed Sensitivity Index. The Pareto-optimal solutions (before applying the proposed methodology) for the investigated case I are shown in Fig. 5. However, there are some Pareto-optimal solutions in Fig. 5 that are not appropriate because of their high sensitivities.

For example, at point A in Fig. 5, the optimal unavailability value is 2.43×10^{-5} and the optimal value of costs is \$5591. At point B, the optimal value of unavailability is 2.53×10^{-5} and the optimal cost value is \$4399. This indicates that around these points, a slight variation (only 1.e-6) in the unavailability causes the high variation in maintenance cost optimization value by \$1192. This means unavailability has high sensitivities on cost in this zone

However, at point F, the optimal unavailability value is 1.38×10^{-4} and the optimal cost value is \$971. At point G, the optimal unavailability value is 1.55×10^{-4} and the optimal value of cost is \$905. This indicates that around these points, a slight variation (only \$66) in the maintenance costs causes the variation in unavailability optimization value up to 1.7×10^{-5} . This means cost has high sensitivities on unavailability in this zone.

On the other hand, for points C and D, a variation in the unavailability optimal value of only 1.e-6 causes the small variation in cost optimal value by \$2543-\$2477=\$66. Thus, in this zone,

Table 3 Parameters used in optimization

Parameters	Values		
Encoding mechanism	Real-parameter		
Population size	500		
Generation numbers	20		
Crossover probability ·	0.6		
Mutation probability	0.01		

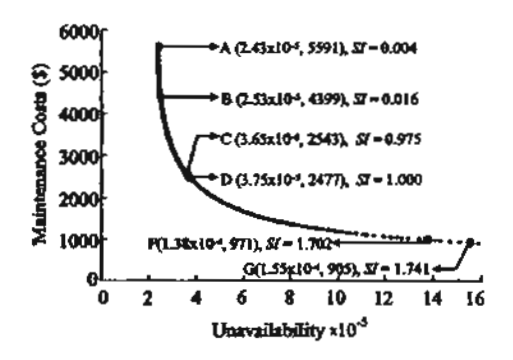


Fig. 5 Pareto-optimal solutions for the investigated case 1

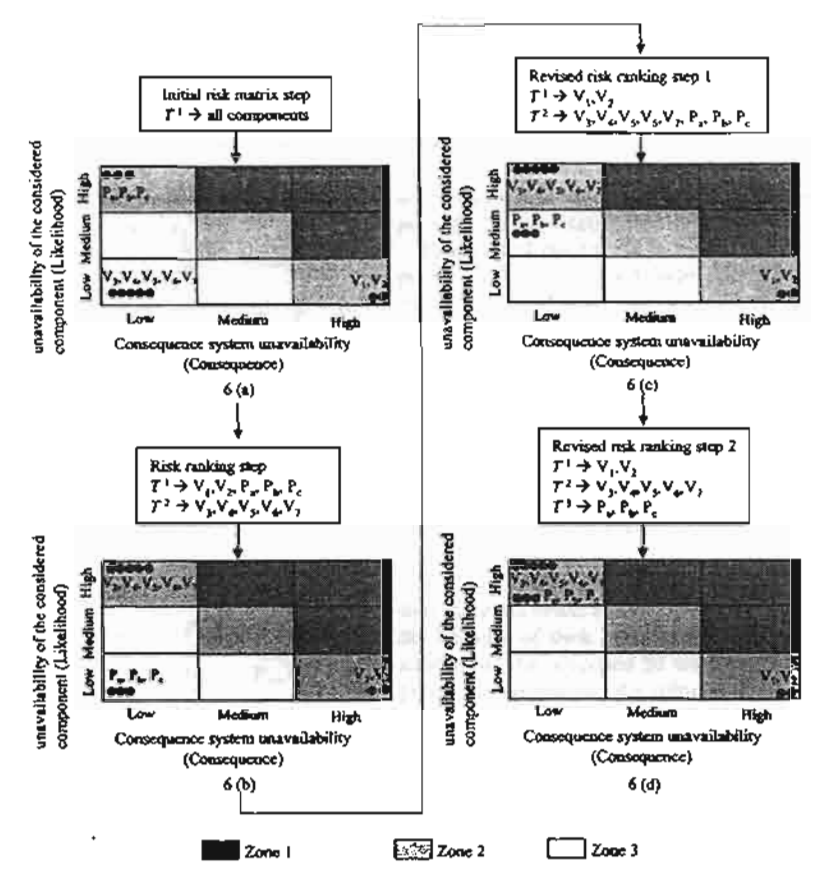


Fig. 6 Risk matrix for investigated case 1

there are low sensitivities for all of objectives. Consequently, in the high sensitivity parts, slight variation of the parameters may cause vast change in the objective function values with lacking of robustness. If the single objective optimization is performed in these high sensitivity zones, the optimization result may not robust enough.

Therefore, in order to obtain the robust solution, the multiobjective optimization should be performed together with the decision-making based on robustness. Thus, the proposed SI is required in the process of the proposed methodology.

The SIs in Fig. 5 show that the values of SIs are far apart from the value of 1.0 in the high sensitivity zones. And SI is equal to 1.0 at point D, which means this point has low sensitivity against variable changes. Therefore, it is shown that the proposed sensitivity index is appropriate to find out the robust solution.

5.2 Application to Risk-Based Inservice Testing. The Pareto-optimal solutions in Fig. 5 can be improved to be more satisfactorily solutions in the viewpoint of risk by applying the proposed methodology. In the processes of the proposed methodology, risk-based inservice testing technique is used to group the system components into optimal different test strategies based on their risk significance. And SI and GA are used in finding the multiobjective optimization solutions of the specified test interval groups.

The results of risk ranking and revising risk ranking of the process in the proposed methodology for investigated case 1 are shown in Fig. 6.

The proposed methodology started with defining the standby system, which is the HPIS shown in Fig. 4. The HPIS has the unavailability parameters and cost parameters of each component as shown in Table 1. After that, the multiobjective optimization is performed for the initial inservice testing groups of components.

Thereafter, the Pareto-optimal solutions are obtained and the

lowest sensitivity solution at SI=1 (described in Sec. 2.1) is selected to create the risk matrix (described in Sec. 2.2).

The result of risk matrix is shown in Fig. 6(a). The result of test interval groups obtained from the risk matrix in Fig. 6(a) is that the components allocated for T^1 are V_1 , V_2 , P_a , P_b , P_c and the components allocated for T^2 are \dot{V}_3 , V_4 , V_5 , V_6 , V_7 .

Thereafter, the multiobjective optimization is performed again for the latest obtained test interval groups and solution at SI=1 is selected to created the risk matrix as the result shown in Fig. 6(b). From this risk matrix, P_a , P_b , P_c , are specified as the case II (described in Sec. 2.3) that should be revised by extending the test interval. Therefore, test interval for P_a , P_b , P_c , is revised from T^1 to T^2 . The result of test interval groups obtained from the revised risk ranking step 1 in Fig. 6(b) is that the components allocated for T^1 are V_1 , V_2 and the components allocated for T^2 are V_3 , V_4 , V_5 , V_6 , V_7 , P_a , P_b , P_c .

The process of multiobjective optimization and revising risk ranking are repeated until the test interval groups are converged like the last step in Fig. 6(d). Figure 6(d) shows that the risk significance of all components falls into the medium risk significance (zone 2). The result is then shown to be the most optimal test interval groups based on risk.

The results for all cases are summarized in Table 4. As shown in Table 4, the converged results (after applying the proposed methodology) are completely same regardless of the initial conditions. This shows the appropriateness of the methodology. The obtained results for the optimal surveillance test interval groups based on risk consideration are shown in Table 5.

In order to confirm the proposed methodology is capable of finding the most optimal surveillance test interval groups based on risk consideration, the Pareto-optimal solutions of initial test interval groups before performing the proposed methodology are

Table 4 Test interval groups for each step in the processes

	n.,	Test interval groups				
Case	Risk ranking step	T'	T ²	T3		
ī	Initial risk	All				
	matrix step	components				
	Risk ranking step	V_1, V_2, P_a	V_3, V_4, V_5, \dots	•••		
	Revised risk	P_b , P_c V_1 , V_2	v_{1}, v_{1}, v_{2}			
	ranking stop l		V_6, V_7, P_4			
	Revised risk	v_1, v_2	v_3, v_i, v_s	P_a , P_b , P_c		
•	ranking step 2		V_6, V_7			
2	Initial risk matrix step	V_1, V_2, P_a, P_a	V_3, V_4, V_5, V_6, V_7			
	Risk ranking	V_1, V_2, V_3	P_a , P_b , P_c	• • •		
	step	V_4, V_5, V_6, V_7				
	Revised risk	$v_1^{v_1}v_2$	V_3 , V_4 , V_5 ,			
	ranking step 1		V_6 , V_1 , P_a ,			
	Revised risk	V_1, V_2	$v_3, v_4, v_5,$	P_a , P_b , P_c		
3	ranking step 2	v_2	V ₆ , V ₇	V_3, V_4, V_5		
3	Initial risk matrix step	v ₂	V_1, P_a, P_b	V_6 , V_7		
	Risk ranking	V_2, V_3, V_4	V_1, P_a, P_b			
	step Revised risk	$V_{5}, V_{6}, V_{7} \\ V_{1}, V_{2}$	$V_3, V_4, V_5,$	P_a . P_b . P_c		
	ranking step 1	11. 12	V ₆ . V ₇	14.14.12		
4	Initial risk	$V_1, V_2, V_3,$	P_a , P_b , P_c			
	matrix step	V_4, V_5, V_6, V_7				
	Risk ranking	V_1, V_2, P_a	$V_3, V_4, V_5,$			
	step	P_b , P_c	V6, V7			
	Revised risk ranking step 1	V_1, V_2	$V_3, V_4, V_5, V_6, V_7, P_a$	• • •		
	ranking step 1		P_b , P_c			
	Revised risk	V_1 , V_2	V_3, V_4, V_5	P_a , P_b , P_c		
	ranking step 2		V_4, V_7			

compared with the Pareto-optimal solutions of the optimal test interval groups obtained by the proposed methodology. The results are shown in Fig. 7.

As shown in the Fig. 7, the objective function values at SI=1 from the Pareto-optimal solutions obtained from four initial cases, which operated with the nonsuitable test interval groups, are not sufficiently appropriate. Therefore, risk management is required

Table 5 The most efficient test interval groups based on risk consideration

Test interval group	Components		
T¹ T² T³	$V_1, V_2 \\ V_3, V_4, V_5, V_6, V_7 \\ P_a, P_b, P_c$		

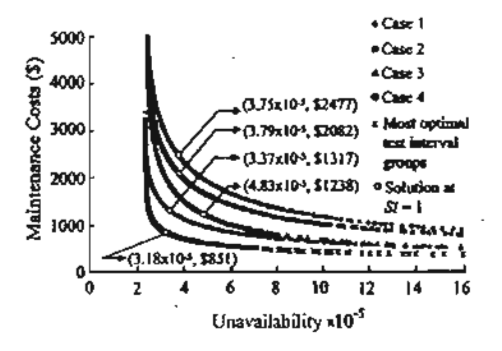


Fig. 7 The comparison of the Pareto-optimal solutions before and after performing the proposed methodology

together with the optimization and the proposed methodology is required. After comparing all of the Pareto-optimal solutions in Fig. 7, the Pareto-optimal solutions obtained after performing the proposed methodology provides the most satisfactory result. Therefore it is confirmed from the results from Fig. 7 that the proposed methodology is capable of determining the most optimal surveillance test interval groups based on risk consideration that provide the most satisfactory result of the Pareto-optimal solutions

From all of the earlier discussions, it is confirmed that the proposed methodology and index provide the effective scheme to achieve the robust solution with the most optimal surveillance test interval groups based on risk consideration.

6 Conclusions

A new methodology for applying the multiobjective optimization to risk-based inservice testing and the decision-making for the Pareto-optimal solution based on robustness were proposed. The proposed methodology and index have been applied to a nuclear power plant's HPIS and the results of this paper can be summarized as follows.

(1) The obtained multiobjective optimal solutions were shown that there are some Pareto-optimal solutions that are not appropriate because of their high sensitivities. The multiobjective optimization and the proposed SI were confirmed that they were appropriate in determining the robust solution.

(2) The proposed methodology was confirmed that it is capable of determining the optimal surveillance test intervals based on risk management. This obtained surveillance test intervals provided the most satisfactory optimal result based on risk consideration.

Conclusively, the proposed methodology is capable of determining the most optimal surveillance test interval based on risk and robust consideration that provided the most satisfactory surveillance test with robustness

Acknowledgment

The first author would like to thank for the support from the Thailand Research Fund (TRF) for the Senior Scholar Professor Pramote Dechaumphai.

Nomenclature

C(T)	=	maintenance	costs	οţ	system	during	period
		T					

$$c_c(T)$$
 = yearly cost contribution as a consequence of performing corrective maintenance

$$c_{\rm bc}$$
 = hourly costs of corrective maintenance

$$c_{\rm ht}$$
 = hourly costs for testing

$$c_l(T)$$
 = maintenance costs of component during period T

d = mean downtime due to corrective maintenance

Risk

achievement

worth (RAW) $= U(U_i=1)/U(base)$.

SI = sensitivity index

T =surveillance test interval

t = mean downtime due to testing
 U(base) = present system unavailability level

 $U(U_i = 1)$ = system unavailability with component i assumed failed

U(T) = average system unavailability during period

 $u_c(T)$ = average unavailability due to corrective maintenance during period T

 $u_{jk}(T)$ = average unavailability at the basic event k of the MCS j during period T

- $u_c(T)$ = average unavailability due to random failure during period T
- $u_i(T)$ = average unavailability due to testing during period T
 - $\rho = \text{per-demand failure probability}$
 - λ = standby failure rate

References

- [1] USNRC, 1998. "Regulatory Guide 1,177-An Approach for Plant-Specific. Risk-Informed Decision Making," Technical Specifications.
- [2] Martorell, S., Carlos, S., Sanchez, A., and Serradell, V., 2000, "Constrained Optimization of Test Intervals Using Steady-State Genetic Algorithm." Reli-
- ability Eng. Sys. Safety. 67(3), pp. 215-232.
 [3] Munoz, A., Martorell, S., and Serradell, V., 1997, "Genetic Algorithms in Optimizing Surveillance and Maintenance of Components," Reliability Eng. Sys. Safety, 57(2), pp. 107-120.
 [4] Vaurio, J. K., 1995. "Optimization of Test and Maintenance-Intervals Based on
- Risk and Cost," Reliability Eng. Sys. Safety, 49(1), pp. 23-36.
- [5] Deb, K., 2001, Multi-objective optimization using evolutionary algorithms, Wiley, New York.
- [6] American Petroleum Institute (API), 2000, "Risk-Based Inspection Base Resource Document." API 581, API publications.

 [7] An ASME Research Report, 1991. "Risk-Based Inspection—Development of

- Guidelines: Volume 1, General Document," CTRD-Vol-20-1, The American Society of Mechanical Engineer (ASME).
- [8] Duthie, J. C., Robertson, M. L., Clayton, A. M., and Łidbury, D. P. G., 1998, "Risk-Based Approaches to Ageing and Maintenance Management," Nucl Eng Des., 184(1), pp. 27-38.
- [9] Khan, F. I., and Haddara, M. M., 2003, "Risk-Based Maintenance (RBM): A Quantitative Approach for Maintenance/Inspection Scheduling and Planning." J. Loss Prev. Process Ind., 16(6), pp. 561-573.
- [10] Nilsson, F., 2003, "Risk-Based Approach to Plant Life Management," Nucl. Eng. Dos., 221(1-3), pp. 293-300.
 [11] Stewart, M. G., 2001, "Reliability-Based Assessment of Ageing Bridges Using
- Risk Ranking and Life Cycle Cost Decision Analyses," Reliability Eng. Sys. Safety, 74(3), pp 263-273.
- [12] An ASME Research Report, 1996, "Risk Based Inservice Testing, Development of Guidelines: Light Water Reactor (Lwr) Nuclear Power Plant Componeats," ASME International
- [13] Balkey, K. R., Art, R. J., and Bosnak, R. J., 1998, "ASME Risk Based Inservice Inspection and Testing: An Outlook to the Future," Risk Anal, 18(4), pp. 407-421.
- [14] Van der Borst, M., and Schoonakker, H., 2001. "An Overview of PSA Importance Measures," Reliability Eng. Sys. Safety, 72(3), pp. 241-245.
- [15] Harunuzzaman, M., and Aldemir. T., 1995, "Optimization of Standby Safety System Maintenance Schedules in Nuclear Power Plants," Nucl. Technol., 113, pp. 354-367.